From star formation to regional distribution: Influences on the embedded cluster mass function

Dissertation
zur
Erlangung des Doktorgrades (Dr. rer. nat.)
der
Mathematisch-Naturwissenschaftlichen Fakultät
der
Rheinischen Friedrich-Wilhelms-Universität Bonn

von
Patrick Lieberz
aus
Köln

Bonn, Februar 2021

Angefertigt mit Genehmigung der Mathematisch-Naturwissenschaftlichen Fakultät der Rheinischen Friedrich-Wilhelms-Universität Bonn

1. Gutachter:	Prof. Dr. Pavel Kroupa
2. Gutachter:	Prof. Dr. Karl Menten
Tag der Promotion:	21.06.2021
Erscheinungsjahr:	2021

Abstract

In this work we study the embedded cluster mass function (ECMF), meaning the mass distribution function of embedded clusters. Embedded clusters are fully or partially enclosed in interstellar gas, dust and molecular clouds and represent the earliest stage in the life-time of a formed star cluster. They may be the forerunners to the open clusters and are therefore valuable probes for cluster formation.

It has been observed that while the ECMF locally has the form of a power-law, the galaxy-wide ECMF has a Schechter-like turn down. This work looks into possible explanations for the difference between the local ECMF and the galaxy-wide ECMF. The main assumption in this work is that the local star formation rate creates an upper mass limit on the ECMF. As the star formation rate varies over the galaxy the upper mass limit would also vary. This would naturally cause turn down similar to a Schechter turn down.

In this work we apply different models for the radial distribution of the star formation rate in a galaxy and how it effects the ECMF. Like a simple Kennicutt-Schmidt power-law relation between the gas surface density and star formation surface density while assuming a thin radially symmetric exponential gas disk. We also make a theoretical derivation of a Kennicutt-Schmidt-like relation from the free-fall time of the gas in a galaxy and thus getting a more detailed star formation rate profile of the galaxy. Finally we also look into the disruptive force created by the gradient of angular velocity caused by a galaxy's flat rotation curve: the shear effect. This effect can further limit the areas of a galaxy in which star formation is possible and could also cause indirectly a size and mass limit on embedded star clusters. In the last we chapter we look whether the ECMF proposed in the second chapter can be applied to the Andromeda galaxy.

Contents

CHAPTER 1

Introduction

1.1 A brief look back into the past

The night sky has fascinated mankind since time immemorial. Ancient cultures saw in stellar formations either the workings of gods or gods themselves.

The earliest known civilization who observed astronomical objects in detail were the Babylonians around 1800 B.C. who noticed the periodicity of several astronomical events and were able to mathematically predict them. One of the oldest remaining works from this time would be the "Enuma Anu Enlil" (Koch-Westenholz, 1995), which mathematically describes the cycles of the moon, methods to calculate lunar and solar eclipses, and visibilities of Venus. While the intention of these models was to make predictions about fortunes based on the belief that what happens in the skies is a reflection of what happens on earth, the math and astronomical predictions made are still quite accurate given the technological limitations of the time.

Over the next thousand years Babylonian astronomers would improve their models to the extent that they were able to describe the motions of Jupiter in such detail that would not be rediscovered for the next two millennia (Ossendrijver, 2016). One of the key reasons why the Babylonians were able to make so accurate astronomical predictions in contrast to e.g. their Greek contemporaries was that dogmatic philosophical ideas were having less influence on their interpretation of observations. While Greek astronomers were convinced of uniform circular motions being a requirement for planetary orbits the Babylonians lacked this bias in their models (Pingree 1992; Koch-Westenholz 1995). This even allowed the Babylonians to make the discovery that the sun was not moving uniformly along the ecliptic, although they apparently were unable to understand why this was the case. But it is assumed that this discovery influenced other classical astronomers like Hipparchus and Ptolemy (Leverington, 2003).

After the hellenisation of the Babylonian area the geocentric model, claiming the sun and the planets to be rotating around earth, became the dominant model until Copernicus published his "De Revolutionibus Orbium Coelestium" in 1543 (Westman, 2011). Although Copernicus' theories were in the beginning controversial and nearly universally doubted the continued work of others like Kepler helped them to regain more credibility. With Kepler's three laws (which overcame the ancient Greek bias of orbits having perfect circles) it was possible to improve the heliocentric model to be more accurate than a geocentric one. Kepler's three laws of planetary motion are:

1. The orbit of a planet is an ellipse with the Sun at one of the two foci. (Kepler, 1609)

2. A line segment joining a planet and the Sun sweeps out equal areas during equal intervals of time. (Kepler 1621; Kepler 1609)

3. The square of a planet's orbital period is proportional to the cube of the length of the semi-major axis of its orbit. (Kepler, 1619)

Another problem for the geocentric model was discovered by Galileo Galilei in 1610. He discovered four moons of Jupiter. As the geocentric model of the time stipulated that all celestial objects are in an orbit around earth this was a clear contradiction. Further he discovered craters on the moon, sunspots and the phases of Venus. As the celestial objects were supposed to be perfect they should not have craters or sunspots. Also the phases of Venus were in contradiction to the notion that earth was in the center of the solar system (Lawson 2004; Finnocchiaro 1989). Although Galileo later under pressure of the Roman Inquisition withdrew his findings they remained in the world and helped establishing the heliocentric model.

In 1687 Isaac Newton published "Philosophiæ Naturalis Principia Mathematica" in which he described what is today known as "Newton's law of universal gravitation" and as Newtonian dynamics. His gravitational law has the form (Newton, 1687):

$$F = G\frac{m_1 m_2}{r^2} \tag{1.1}$$

Using these discoveries Newton was able to derive Kepler's laws from first principles thus creating a theoretical foundation for modern astronomy and physics. Newton's discoveries remain relevant even today. Even though Einstein's theory of general relativity has been superseding Newton's law of universal gravitation its applicability as a good approximation leads to it remaining used well into modern astrophysics. In fact general relativity only becomes relevant when looking at objects in a strong gravitational field, e.g. a black hole.

Over the next centuries observational capabilities and methods to estimate distances improved allowing for a more detailed view of the universe outside the solar system. This led to questions about the nature of the "spiral nebulae" (today known to be spiral galaxies) such as Andromeda. Opinions differed whether these "spiral nebulae" were part of our galaxy (making our galaxy to be equivalent to the universe) or if they were galaxies on their own (Trimble, 1995). Curiously, from our modern perspective, the proponents of the idea of the existence of several galaxies believed that the sun was in the center of our galaxy, while the proponents of the idea that the "spiral nebulae" were part of our galaxy believed our sun to be much closer to the position it is determined to be nowadays (Trimble 1995; Curtis 1917). The main arguments of the single-galaxy idea camp were that if Andromeda would be its own galaxy the distance would be of the order 10^8 pc. A distance unimaginable at the time. Also Adriaan van Maanen claimed to have seen the rotation of the Pinwheel galaxy - which would be impossible, if it was outside of our galaxy. The main arguments of the several galaxies camp were that more novae were found in Andromeda than in the Milky Way and that the structure of Andromeda closely resembles what we know about the structure of our galaxy (Curtis, 1917). This debate was finally resolved by Hubble by observing cepheids and determining distances using them, therefore finding that our galaxy is only one of many in the universe (e.g. Hubble 1926). This in turn necessitated research into the dynamics of galaxies.

1.2 Dark Matter and MoND

1.2.1 Historical overview

In 1933 Fritz Zwicky applied the virial theorem to the Coma Cluster to get an estimate on the mass of the cluster. He realized that the mass he got from the virial theorem was different than the mass estimate he got from the brightness of the cluster and its galaxies. From this observation Zwicky assumed that there had to be some unseen (dark) matter within the cluster and that this non-luminous mass is what held the galaxy cluster gravitationally together (Zwicky 1933; Zwicky 1937).

Shortly after that other discrepancies between the determined mass using classical theories and mass determined from luminosities were discovered. So was the rotation curve of Andromeda deemed to be abnormal (the suggested reason was light absorption Babcock 1939) and NGC 3115 was found to have a sort of invisible halo (Oort, 1940).

In 1970 Vera Rubin and Kent Ford observed the rotation curve of the Andromeda galaxy in greater detail, which again confirmed that the determined rotation curve did not fit the observed mass profile when using Newtonian dynamics (Rubin and Ford, 1970). The determined rotation curve and mass profile needed to cause this profile can be seen in Fig. 1.1. By 1980 these observations of an apparent contradiction between the observed mass distribution and the determined rotation curve were confirmed for many more galaxies (e.g. Rubin, Ford and Thonnard 1980). This led to the general acceptance of dark matter as an yet undetermined particle responsible for the invisible extra mass.

At first there was the idea that an already known particle within the limits of the standard model of particle physics could be responsible for the observed effects: the neutrino. But it was soon calculated that the upper bound for the neutrino density is too low to cause the observed effects (Bertone, Hooper and Silk, 2005). Therefore the search for the dark matter particle went to non-standard model particles like the neutralino. As a consequence the theory of an unknown cold dark matter particle emerged in the 1980s (Peebles 1982; Bond, Szalay and Turner 1982; Blumenthal, Pagels and Primack 1982; Blumenthal, Faber et al. 1984).

Following the discovery of the cosmic microwave background anisotropy by the Cosmic Background Explorer in 1992 (Smoot et al. 1992; Bennett et al. 1996) the credibility of cold dark matter models became strengthened. And after the observations indicating an accelerating universe were made in 1998 (Riess et al., 1998) the ΛCDM cosmology became the leading theory.

However already in the 1980s an alternative theory was created. Given the observational constraints detailed above there are currently only two known possible explanations:

- There is an huge amount of hidden mass we cannot detect
- Newton's laws do not work on the scales of galaxies or higher

ΛCDM cosmology (and other cold dark matter theories) assume the first option to be true. But if one argues that there is no cold dark matter then Newton's laws have to be modified on the scale of galaxies. The most known example is modified Newtonian dynamics (MOND) developed by Mordehai Milgrom (Milgrom 1983d; Milgrom 1983a; Milgrom 1983b).

1.2.2 ΛCDM Cosmology

The Lambda cold dark matter (ΛCDM) model is a Big Bang cosmological model with implications down to the current behaviour of galaxies. In short it postulates that the universe contains three major

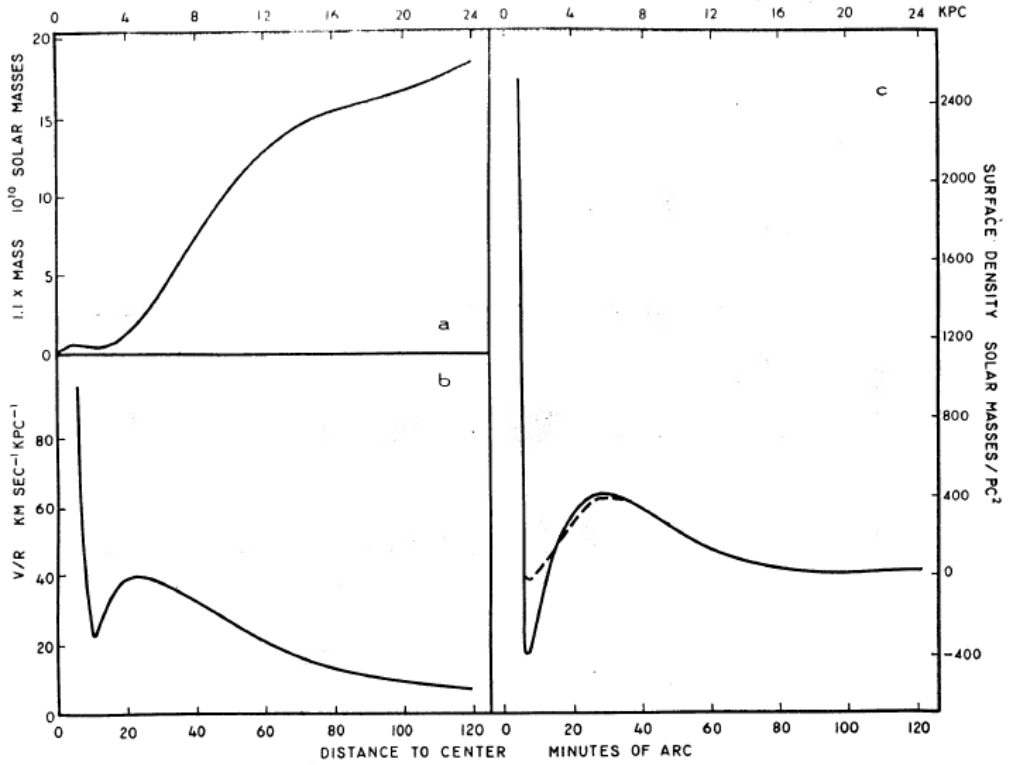

FIG. 10.—(*a*) Total mass of M31 out to $R = 24$ kpc determined from rotation curve (Fig. 9), as a function of distance from the center, and multiplied by 1.1 to compensate for flat disk approximation. (*b*) Angular velocity, V/R, for M31, calculated from rotation curve, as a function of distance from center. (*c*) Surface density for M31, determined from rotation curve, as a function of distance from center. Solid curve and dashed curve are calculated from corresponding curves in Fig. 9.

Figure 1.1: fig. 10 from Rubin and Ford (1970) with original caption

components. In order of abundance: a cosmological constant (Λ) often argued to be dark energy, cold dark matter and baryonic matter (see also Fig 1.2). Like most modern cosmological models it assumes the cosmological principle to be true: that our position within the universe is neither unusual or special and therefore most observations made from earth would be the same if made from another point in the universe. From this follows the claim that the universe looks the same in all directions (isotropy) and from every location (homogeneity). Further it assumes Einstein's general relativity to be the correct theory of gravity for large and cosmological scales.

The main component of the universe, according to the ΛCDM model, is the cosmological constant Λ seen as responsible for the accelerating expansion of the universe. The cosmological constant is assumed to have a negative pressure which, according to general relativity, would cause an accelerating expansion. Current estimates assumes the cosmological constant contributes around 67% of the total energy density of the universe (Abbott et al. 2019; Planck Collaboration et al. 2020).

The ΛCDM postulates the existence of cold dark matter and assumes it is responsible various observed anomalies, e.g. the flattening of rotation curves of galaxies and gravitational lensing of

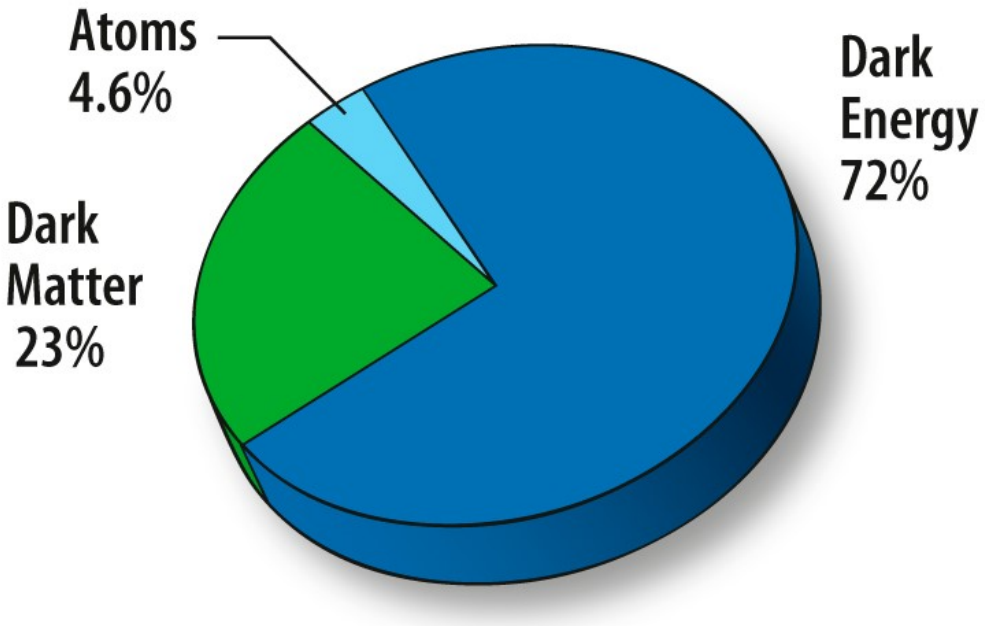

Figure 1.2: The current composition of the universe according to the ΛCDM model.
Source: NASA and WMAP Science Team (2013)

galaxy clusters. The ΛCDM model proposes the following characteristics for the unknown cold dark matter:

- CDM-particles are non-baryonic
- CDM is cold meaning its velocity is significantly lower than the speed of light
- CDM-particles only interact gravitationally and weakly
- CDM-particles are stable

According to current estimates dark matter contributes around 26.5% and baryonic matter around 5% of the total energy density of the universe (Planck Collaboration et al., 2020).

Applying the ΛCDM model to the rotation curves of spiral galaxies

A relatively simple way to calculate the rotation curve $V(R)$, at galactocentric distance R, of a galaxy is by calculating separate rotation velocities for the distinct components of the galaxy (Sofue, 2013). Note that this is a simplification as in reality these components cannot be strictly separated. If one assumes the ΛCDM model and a standard spiral galaxy, one has three main components: the spheroidal bulge in the center (which causes the rotational velocity $V_\mathrm{b}(R)$), the thin disk (which produces the rotational velocity $V_\mathrm{d}(R)$) and the dark matter halo (which causes the rotational velocity $V_\mathrm{h}(R)$). The total velocity $V(R)$ is then given by the square root of the sum of the square of the individual rotational velocities:

$$V(R) = \sqrt{V_\mathrm{b}(R)^2 + V_\mathrm{d}(R)^2 + V_\mathrm{h}(R)^2}\,. \tag{1.2}$$

If the rotation curve close to the center of the galaxy is of interest it might be necessary to add as another component the rotation curve caused by an eventual central black hole.

Regarding the bulge: the luminosity profile of the bulge component of galaxies has been found to follow a de Vaucouleurs law (de Vaucouleurs 1953; de Vaucouleurs 1958; Sofue 2013). From this one can determine the surface mass density profile of the bulge ($\Sigma_b(R)$):

$$\Sigma_b(R) = \Sigma_{be} \exp\left[-\kappa\left(\left(\frac{R}{R_b}\right)^{1/4} - 1\right)\right], \tag{1.3}$$

with $\kappa = 7.6695$ being a constant, R_b being the half-mass radius (meaning half the projected mass is inside a cylinder of radius R_b) and Σ_{be} being the surface mass density at radius R_b. By definition Σ_{be} is $\Sigma_b(0)/\kappa$. The total bulge mass within galactocentric radius R ($M_b(R)$) can therefore be calculated by:

$$M_b(R) = 2\pi \int_0^R r\Sigma_b(r)\, dr\,. \tag{1.4}$$

As the mass distribution is assumed to be spherical the resulting rotational velocity $V_b(R)$ is:

$$V_b(R) = \sqrt{\frac{GM_b(R)}{R}}\,. \tag{1.5}$$

The galactic disk can be assumed to be an exponential disk (Freeman 1970; Sofue 2013) resulting in a surface mass density profile $\Sigma_d(R)$ of

$$\Sigma_d(R) = \Sigma_{dc} \exp\left(-R/R_d\right), \tag{1.6}$$

with Σ_{dc} being the surface mass density in the center of the disk and R_d being the scale radius of the disk. Note that Eq. (1.6) describes a perfect symmetric exponential disk without any perturbations or distortions. If one wants to include such disturbances as an additional mass terms Δ then Eq. (1.6) becomes

$$\Sigma_d(R) = \Sigma_{dc} \exp\left(-R/R_d\right) + \Delta\,, \tag{1.7}$$

but continuing this thesis will assume perfect exponential disks. The rotational velocity $V_d(R)$ resulting from Eq. (1.6) is (Freeman 1970; Binney and Tremaine 2008; Sofue 2013)

$$V_d(R) = \sqrt{4\pi\Sigma_{dc}R_d y^2\left[I_0(y)K_0(y) - I_1(y)K_1(y)\right]}\,, \tag{1.8}$$

with $y = R/(2R_d)$ and I_i and K_i being the modified Bessel functions.

Regarding the rotation curve caused by the dark matter halo is is important to note that there are several different models describing the density distribution of the halo, which therefore vary slightly in their proposed rotational velocity caused by the dark matter halo. One of the most simple models would be an isothermal spherical distribution of the dark matter halo (Kent 1986; Begeman, Broeils and Sanders 1991; Sofue 2013) causing the density profile $\rho_{iso}(R)$ to be

$$\rho_{iso}(R) = \frac{\rho_{iso}^0}{1 + (R/h)^2}\,, \tag{1.9}$$

where $\rho^0_{\rm iso}$ is central mass density of the dark matter halo and h its scale radius. Neither of these parameters are directly observable but they are linked to the rotation curve at an infinite distance (or in more practical terms the observable velocity when the rotation curve becomes flat) V_∞

$$V_\infty = \sqrt{4\pi G \rho^0_{\rm iso} h^2}\,, \tag{1.10}$$

leaving this model with one remaining free parameter. From this follows the rotation curve caused by the dark matter halo to be

$$V_{\rm h}(R) = V_\infty \sqrt{1 - \left(\frac{h}{R}\right) \tan^{-1}\left(\frac{R}{h}\right)}\,. \tag{1.11}$$

As mentioned the above model is on eof the most simple ones and several others fitting more closely to the observed rotation curves have been found. Two examples are the NFW model by Navarro, Frenk and White (1996) and the Burkert model by Burkert (1995). Both models assume a slightly different density profile. The NFW model assumes a density profile $\rho_{\rm NFW}(R)$ of

$$\rho_{\rm NFW}(R) = \frac{\rho^0_{\rm NFW}}{(R/h)\left[1 + (R/h)\right]^2}\,, \tag{1.12}$$

and the Burkert model assumes a density profile $\rho_{\rm bur}(R)$ of

$$\rho_{\rm bur}(R) = \frac{\rho^0_{\rm bur}}{\left[1 + (R/h)\right]\left[1 + (R/h)^2\right]}\,. \tag{1.13}$$

As both models assume sphericity the resulting mass of the dark matter halo ($M_{\rm h}(R)$) within galactocentric distance R is

$$M_{\rm h}(R) = 4\pi \int_0^R \rho_{\rm NFW\,/\,bur}(r) r^2\, dr\,, \tag{1.14}$$

and therefore the rotation curve follows as

$$V_{\rm h}(R) = \sqrt{\frac{G M_{\rm h}(R)}{R}}\,. \tag{1.15}$$

Using these methods several accurate descriptions of rotation curves were made, e.g. Corbelli et al. (2014).

1.2.3 Modified Newtonian Dynamics

Please note that this section is the same as section 3.1.1.

Milgromian Dynamics (MOND, Milgrom, 1983c) is as an alternative to a dark matter dominated universe deduced from the flattening of observed rotation curves, which are in contrast to classical Newtonian models without dark matter. MOND is a space-time invariance symmetry of the equations of motion (Milgrom 1983c; see also Wu and Kroupa 2015) and may be an effect of the physical quantum vacuum (Milgrom 1999; Smolin 2017).

MOND as derived from a classical Lagrangian (Bekenstein and Milgrom, 1984) introduces the natural constant $a_0 = 1.2 \times 10^{-10}\,\mathrm{m/s^2}$ and states that if the Newtonian gravitational acceleration $g_\mathrm{N} \gg a_0$, the Newtonian gravitational description should be used but if $g_\mathrm{N} \ll a_0$, the gravitational acceleration g becomes in spherical symmetry

$$g = \frac{\sqrt{GMa_0}}{R}\,. \tag{1.16}$$

In other words, if the distance to an object is much larger than its MOND radius R_M, which follows from Eq. (1.16) for $g = a_0$:

$$R_\mathrm{M} = \sqrt{\frac{GM}{a_0}}\,, \tag{1.17}$$

then the gravitational acceleration will be given by Eq. 1.16.

Milgrom (1983c) developed an algebraic approximation for the gravitational acceleration g:

$$g = g_\mathrm{N}\nu\left(\frac{g_\mathrm{N}}{a_0}\right)\,, \tag{1.18}$$

with $\nu(x)$ being the so-called interpolation function (shown to be derivable from the quantum vacuum, see Milgrom 1999) fulfilling the following conditions: $(x \gg 1 \mid \nu(x) = 1)$ and $\left(x \ll 1 \mid \nu(x) = \sqrt{1/x}\right)$. So, for example, in the case of a single point mass ($g_\mathrm{N} = GM/R^2$) Eq. (1.18) would become

$$g = \frac{GM}{R^2}\nu\left(\frac{GM}{a_0R^2}\right)\,. \tag{1.19}$$

There are three well-defined extreme cases of MOND. Firstly, if $g_\mathrm{N} \gg a_0$, we have the Newtonian case, where ν becomes 1 and the gravitational acceleration g_N becomes according to Eq. 1.19

$$g(g_\mathrm{N} \gg a_0) = g_\mathrm{N} = \frac{GM}{R^2}\,, \tag{1.20}$$

which is the classical Newtonian description. Secondly, an isolated point mass with $g_\mathrm{N} \ll a_0$ constitutes the isolated deep-MOND limit, where $\nu(x) = \sqrt{1/x}$ and the gravitational acceleration (g_idM) becomes, according to Eq. 1.19,

$$g_\mathrm{idM} = \sqrt{a_0 g_\mathrm{N}} = \frac{\sqrt{GMa_0}}{R}\,. \tag{1.21}$$

Finally, if the point mass is not isolated and the gravitational acceleration of an external field ($g_\mathrm{ext,N}$) is much larger than the internal gravitational field ($g_\mathrm{int,N}$) but still much smaller than a_0, so $g_\mathrm{int,N} \ll g_\mathrm{ext,N} \ll a_0$, then the quasi-Newtonian regime results. The quasi-Newtonian regime needs a different algebraic interpolation function (Banik and Zhao, 2018b):

$$g = g_\mathrm{N}\nu\left(\frac{g_\mathrm{N}}{a_0}\right)\left(1 + \frac{K}{3}\right)\,, \tag{1.22}$$

with

$$K = \left.\frac{d\log\nu(x)}{d\log x}\right|_{x=g_N/a_0} . \tag{1.23}$$

In the extreme case of the Quasi-Newtonian regime, $\nu = \sqrt{a_0/g_{\mathrm{ext,N}}}$ and $K = -\frac{1}{2}$, accordingly $\left(1+\frac{K}{3}\right) = \frac{5}{6}$ and the gravitational acceleration (g_{QN}) therefore becomes:

$$g_{\mathrm{QN}} = \frac{5}{6}\sqrt{\frac{a_0}{g_{\mathrm{ext,N}}}}\,g_{\mathrm{int,N}} = \frac{5}{6}\sqrt{\frac{a_0}{g_{\mathrm{ext,N}}}}\,\frac{GM}{R^2} \tag{1.24}$$

To summarize: Eq. 1.18 is valid for isolated objects while Eq. 1.22 should be used if the external gravitational field is much stronger than the internal one.

Note that if either $g_{\mathrm{ext,N}}$ or $g_{\mathrm{int,N}}$ or the combined Newtonian acceleration $g_{\mathrm{N}} = \sqrt{g^2_{\mathrm{int,N}} + g^2_{\mathrm{ext,N}}}$ is much larger than a_0, then the system is in the Newtonian regime (for a summary, see Fig. 1.3).

Using MoND to calculate the rotation curves of spiral galaxies

Using MoND calculating the rotation curve of galaxies at great galactocentric distances is easily done. If the distance is large enough one can assume the galaxy to be a point-mass and can use Eq. (1.19). A slight modification leads to:

$$g_{\mathrm{idM}}R = V^2 = \sqrt{GMa_0}\,, \tag{1.25}$$

which directly gives us the rotational velocity of

$$V = \left(GMa_0\right)^{1/4} . \tag{1.26}$$

This is just the relation known as Tully-Fisher relation (Tully and Fisher, 1977), which is an empirical relationship between the luminosity (and thus the baryonic mass) of a galaxy and its asymptotic rotation velocity. This empirical relationship is therefore derivable using MoND.

If one wants to calculate a more detailed rotation curve this is also quit simple. One can use an approach like in section 1.2.2, sans the contributions of the dark matter halo to the rotation curves. One then has the rotational velocity according to Newton $V_N(R)$. Further one can calculate the Newtonian acceleration $a_N(R)$

$$a_N(R) = \frac{V_N(R)^2}{R} . \tag{1.27}$$

Using this one can then calculate the acceleration according to MoND:

$$a(R) = a_N(R)\nu\left(\frac{a_N(R)}{a_0}\right) , \tag{1.28}$$

and finally use this to calculate the rotational velocity according to MoND:

$$V(R) = \sqrt{a(R)R}\,. \tag{1.29}$$

This is a solution assuming ideal circumstances and ignores the possibility of e.g. the external field of other galaxies influencing the rotational velocity.

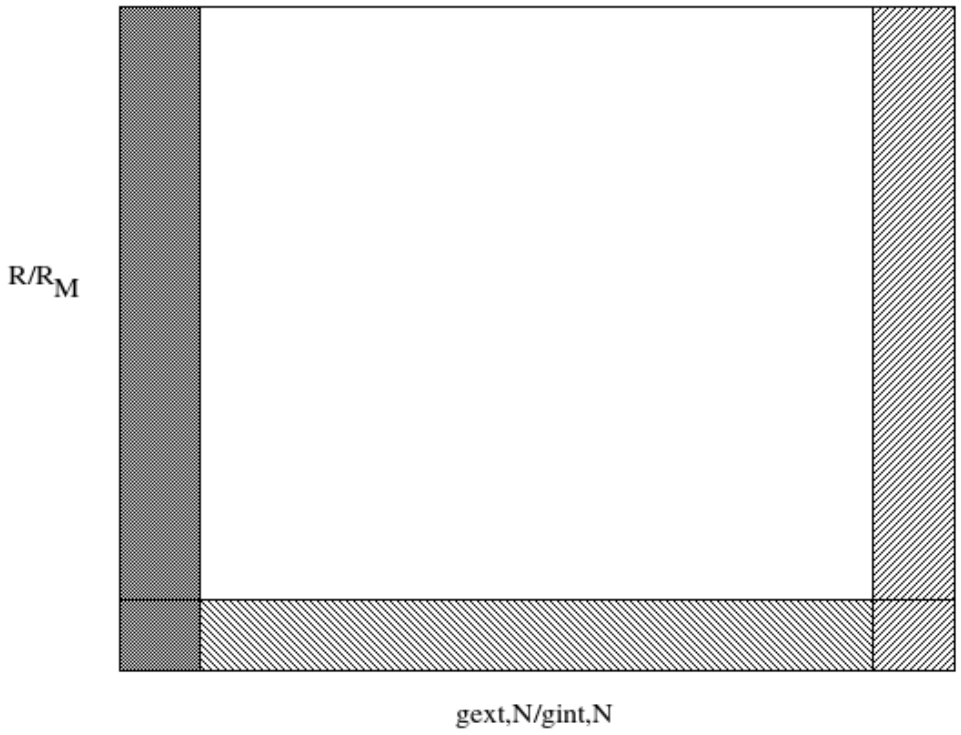

Figure 1.3: A schematic, where the x-axis represents the relative strength of the external gravitational acceleration $g_{\mathrm{ext,N}}$ compared to the initial internal gravitational acceleration $g_{\mathrm{int,N}}$ and the y-axis shows the initial distance in units of MOND radii R_{M}. The dark grey area shows the deep-MOND regime in which the interpolation function of Eq. 1.19 is valid for calculating the gravitational acceleration. The hatched part on the bottom of the schematic is completely in the Newtonian regime and therefore the gravitational acceleration can be calculated using Eq. 1.20. Finally, the hatched area on the right side is external-field dominated and can therefore be calculated using the interpolation function from Eq. 1.22. There is no analytic solution for the upper middle (white) part of the schematic, for which numerical methods are needed.

1.3 The mass functions of stars and clusters

At its core the initial mass function (IMF, $\xi(m)$) is an empirical function describing the initial mass distribution of a population of stars born from the same event (Kroupa, Weidner, Pflamm-Altenburg et al., 2013b). In this case "event" describes a gravitationally driven process of transforming gaseous matter into stars over a time scale of about 1 Myr and a spatial scale of about 1 pc or, in other words, the star formation process within an embedded cluster.

Over time several descriptions of the IMF have emerged. The oldest and most simple was determined by Salpeter (1955) and took the form of power-law:

$$\xi(m) = km^{-2.35}\,, \tag{1.30}$$

with m being the stellar mass and k being a constant. Newer observations showed that a single power-law was insufficient to accurately describe the low-mass end of the IMF. Kroupa (2001) found a broken power-law to be better fit and describing both the low-mass and high-mass end of the IMF (also known as the canonical IMF):

$$\xi(m) = k \begin{cases} m^{-1.3\pm0.3} & ,0.07M_\odot < m \leq 0.5M_\odot, \\ 0.5m^{-2.3\pm0.3} & ,0.5M_\odot < m \leq 150M_\odot. \end{cases} \tag{1.31}$$

An alternative to the canonical IMF was described by Chabrier (2003) in the the form of the log-normal canonical IMF:

$$\xi(m) = k \begin{cases} \frac{1}{m} \exp\left[-\frac{(\log_{10} m/M_\odot - \log_{10} m_c/M_\odot)^2}{2\sigma_{lm}^2}\right] & ,0.07M_\odot < m \leq 1M_\odot, \\ Am^{-2.3\pm0.3} & ,1M_\odot < m \leq 150M_\odot, \end{cases} \tag{1.32}$$

with $m_c = 0.079^{-0.016}_{+0.021}\ M_\odot$, $\sigma_{lm} = 0.69^{-0.01}_{+0.05}$ and $A = 0.2791$ according to Chabrier (2003). A comparison between the canonical IMF and the log-normal canonical IMF can be seen in Fig. 1.4, which is fig. 24 from Kroupa, Weidner, Pflamm-Altenburg et al. (2013b).

In order to quantitatively apply the above IMF-descriptions one needs additional information about the constant k and the upper mass limit of the equations. The upper mass limit can be expressed as the heaviest observed star within an embedded cluster $m_{\rm max}$. One obvious upper limit for $m_{\rm max}$ would be the general upper mass limit for stars $m_{\rm max*}$. The exact value of $m_{\rm max*}$ has been grounds for discussions but in general a value of around 150 $M_\odot$ was found to be fitting (Kroupa, Weidner, Pflamm-Altenburg et al., 2013b). Another observation is that $m_{\rm max}$ seems also to correlate to the mass of the embedded cluster $M_{\rm ecl}$ (see e.g. Weidner, Kroupa and Bonnell 2010 and Kirk and Myers 2011). A graphical representation of the correlation between $m_{\rm max}$ and $M_{\rm ecl}$ can be seen in Fig. 1.5 (fig. 5 from Kroupa, Weidner, Pflamm-Altenburg et al. 2013b).

Therefore a quantitative description of the IMF needs to include the underlying $M_{\rm ecl}$, or more general a description of the mass function of embedded star clusters, the embedded cluster mass function (ECMF, $\xi_{\rm ecl}$). Similar to the IMF, the ECMF is often described as having the form of a power-law (C. J. Lada and E. A. Lada, 2003b)

$$\xi_{\rm ecl}(M_{\rm ecl}) = KM_{\rm ecl}^{-\beta}\,, \tag{1.33}$$

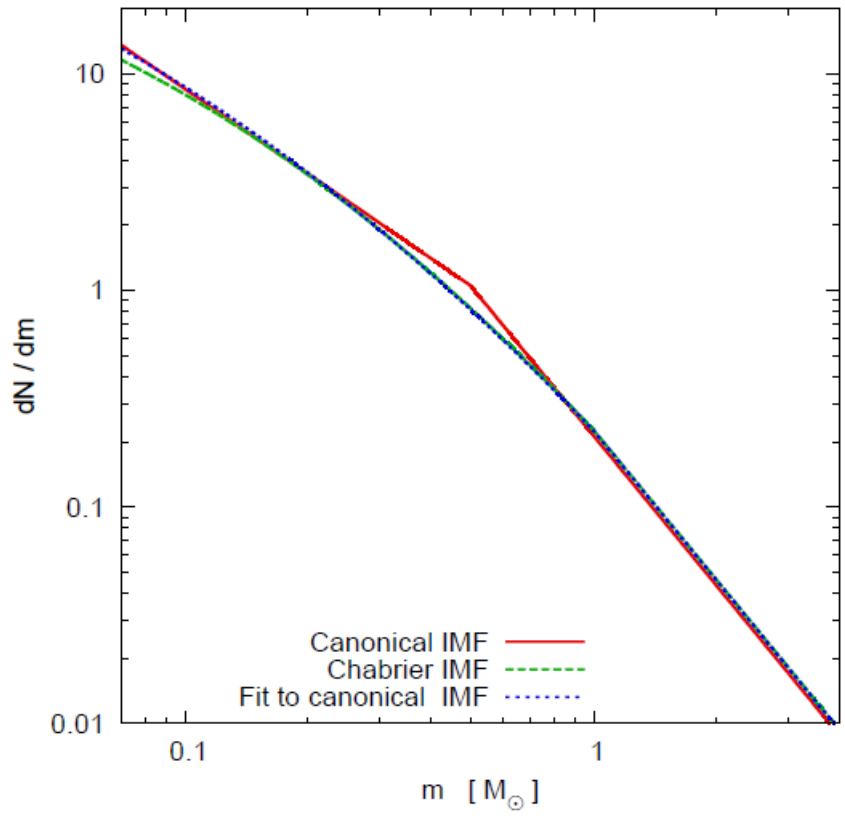

Figure 1.4: fig. 24 from Kroupa, Weidner, Pflamm-Altenburg et al. (2013b). It is shown that the different portrayed IMF descriptions are indistinguishable from each other over the whole mass interval.

with K being a constant and β the power-law index. Observationally β has been found to be between 1.5 and 2.5 (Weidner, Kroupa and Larsen, 2004a).

Again similar to the IMF, to describe the ECMF quantitatively one needs to constrain its upper mass limit. Observationally it has been found that the local maximum cluster mass $M_{\rm ecl,max}$ depends on the local star formation rate SFR (see e.g. Weidner, Kroupa and Larsen 2004a and Weidner and Kroupa 2005). As the SFR of galaxy varies over its surface area, the observed $M_{\rm ecl,max}$ would also vary over the galaxy. This would result in the observed effect that while the ECMF locally has the form of a power-law, the galaxy-wide ECMF has a Schechter-like turn down (Gieles et al., 2006a). This gets discussed in more detail and with a mathematical description of the galaxy-wide ECMF in chapter 2.

1.4 The star formation rate in a galaxy

As described in Sec. 1.3 the exact form of the embedded cluster mass function depends on the underlying star formation rate, or to be more accurate the star formation surface density ($\Sigma_{\rm SFR}$). There are several ways to model the star formation rate of galaxy. One of the earliest models was created by citetSchmidt, who examined the Milky Way and found a relation between the star formation surface

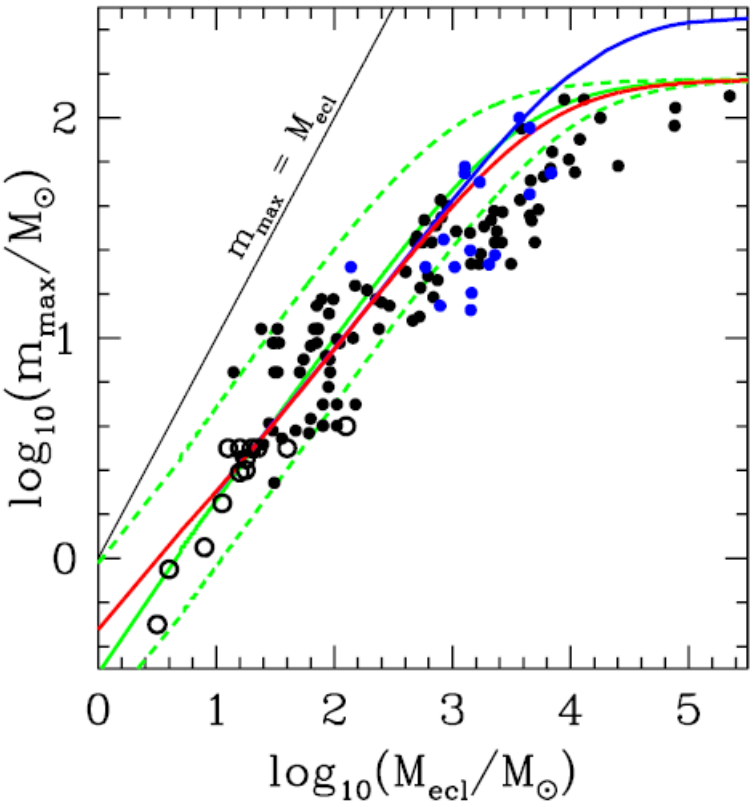

Figure 1.5: fig. 5 from Kroupa, Weidner, Pflamm-Altenburg et al. (2013b) showing the $m_{\rm max}$-$M_{\rm ecl}$ relation. The solid dots are observed clusters from Weidner, Kroupa and Bonnell (2010), while the open circles are observations from Kirk and Myers (2011). The blue and red line show a calculated $m_{\rm max}$-$M_{\rm ecl}$ relation using eq. 12 from Kroupa, Weidner, Pflamm-Altenburg et al. (2013b). The red lines assumes $m_{\rm max*} = 150\,M_\odot$ and the blue line $m_{\rm max*} = 300\,M_\odot$. The green lines show the result of randomly sampling $m_{\rm max}$ from a population of stars, with the solid green line being the median and the dashed green lines showing are the boundaries of 2/3 of all sampled data points.

density and the gas surface density $\Sigma_{\rm gas}$) in the form of a power-law (then known as the Schmidt-law)

$$\Sigma_{\rm SFR} \propto \Sigma_{\rm gas}^{n}\,, \tag{1.34}$$

with $n \approx 2$. Years later Kennicutt (1989) determined $n \approx 1.4$ from Hα observations of 7 galaxies, which resulted in the relation to be known as the Kennicutt-Schmidt law. Since then, a value of $n \approx 1.5$ has become accepted and also supported by observations (see e.g. Heyer et al. 2004; A. Leroy et al. 2005; Kennicutt et al. 2007), forming the basis for both theoretical and simulation work (see e.g. Schaye and Dalla Vecchia 2008).

On the other hand, ultraviolet observations (Boissier et al., 2007) find a value of $n = 0.99$. Ultraviolet observations are less sensitive to the presence of young, very massive stars and are therefore more likely to derive a value of n close to the true one. Furthermore Pflamm-Altenburg and Kroupa (2008a) support $n = 1$ through the radially changing initial mass function of stars expected in the integrated galactic initial mass function (IGIMF) theory (Kroupa and Weidner 2003; Kroupa, Weidner, Pflamm-Altenburg et al. 2013a). This form of the Kennicutt-Schmidt law, together with the assumption of a thin exponential gas disk, was assumed for determining $\Sigma_{\rm SFR}$ in chapter 2 and chapter 4.

In chapter 3 the Kennicutt-Schmidt gets derived theoretically and it is shown while overall a power-law is a good approximation for the relation between star formation and gas surface density, a more detailed description was found as well.

Another big influence on the relation on star formation is whether star formation is possible in the observed region of the galaxy. One possible quantity which can be used to determine the possibility of star formation is the shear effect Hunter, Elmegreen and Baker (1998), A. Leroy et al. (2005) and Dib et al. (2012). Because the rotation curve of a galaxy is approximately constant rather than increasing linearly with galactocentric distance R, the angular velocity of orbiting gas decreases with increasing R. The gradient of angular velocity gives rise to a disruptive force, the shear effect. If an object in the galaxy (e.g. a molecular cloud) grows so large that the shear effect becomes stronger than the self-gravity of the object, then the shear effect would destroy or reduce the size of the object. The influence of the shear effect on the upper mass limit of an embedded cluster in a given region of the galaxy is discussed in chapter 5.

CHAPTER 2

On the Origin of the Schechter-Like Mass Function of Young Clusters in Disk Galaxies

This chapter is based on the publication Lieberz and Kroupa (2017a) with the same title "On the Origin of the Schechter-Like Mass Function of Young Clusters in Disk Galaxies". Only minor changes concerning formatting were made in order to present it as a chapter in the thesis.

Abstract The mass function of freshly formed star clusters is empirically often described as a power law. However the cluster mass function of populations of young clusters over the scale of a galaxy has been found to be described by a Schechter-function. Here we adress this apparent discrepancy. We assume that in an annulus of an isolated self-regulated radially-exponential axially-symmetric disk galaxy, the local mass function of very young (embedded) clusters is a power law with an upper mass limit which depends on the local star formation rate density. Radial integration of this mass function yields a galaxy-wide embedded cluster mass function. This integrated embedded cluster mass function has a Schechter-type form, which results from the addition of many low mass clusters forming at all galactocentric distances and rarer massive clusters only forming close to the center of the galaxy. In this chapter we present for the first time an analytical approach to the integrated embedded cluster mass function making the assumption of the upper mass limit decreasing exponentially with the galactocentric distance. We show that a Schechter-like function obtained this way is in accordance with observational data.

2.1 Introduction

The freshly-formed stellar mass of a galaxy resides in its embedded star clusters (C. J. Lada and E. A. Lada 2003b; Megeath et al. 2016a; Meingast et al. 2016b), which can synonymously be referred to as (about 1 pc extended, 1 Myr duration) space-time correlated star-formation events. i.e. essentially in molecular cloud clumps. The investigation of embedded clusters helps us to understand the buildup of the stellar populations in galaxies.

Embedded clusters are fully or partially enclosed in interstellar gas, dust and molecular clouds and represent the earliest stage in the life-time of a formed star cluster. They may be the forerunners to the open clusters and are therefore valuable probes for cluster formation (C. J. Lada and E. A. Lada, 2003b).

Observations indicate that the masses of the embedded star clusters in galaxies follow a particular distribution function, the embedded cluster mass function (ECMF). Locally it is typically found to be a power-law, while galaxy-wide observation reveal a Schechter-like turn-down (Gieles et al., 2006a). This has also been observed for old, massive globular clusters (see e.g. Jordán et al. 2007; Burkert and Smith 2000; Parmentier and Gilmore 2007). Massive clusters do not experience much dynamical evolution and are therefore still a reasonable indicator for the initial cluster mass function (Baumgardt and Makino, 2003).

The focus of this chapter is on embedded clusters in the disks of isolated late-type galaxies. Ideally the disk can be seen as a purely self-regulated axis-symmetric system, such that it is possible to investigate the ECMF only radially over the area of the disk galaxy to explain the difference between the local and integrated distribution.

In this chapter we present for the first time analytical approaches to the galaxy wide ECMF and also rewrite the dependency on the galactocentric distance into a mass dependency so that we arrive at a new relation between the number and the mass of star clusters. Hereby we follow the ansatz that the galaxy-wide ECMF is the sum of all local ECMFs.

We constrain these models with observational data and show that the models account for the data quite well.

2.2 The local embedded cluster mass function

The local ECMF (LECMF or $\xi_{\rm lecl}$) describes the surface number density of star clusters in the stellar mass interval $\left[M_{\rm ecl},\ M_{\rm ecl}+{\rm d}M_{\rm ecl}\right]$ in an infinitesimally small surface area (dA) at a distance r from the center of the star-forming disk galaxy

$$\xi_{\rm lecl}(M_{\rm ecl};r)\,{\rm d}M_{\rm ecl}\,{\rm d}A = {\rm d}N_{\rm ecl}\,, \tag{2.1}$$

where d$N_{\rm ecl}$ is the number of embedded clusters in d$M_{\rm ecl}$ and dA.

In general the LECMF has the form of a power law, as derived from observations (C. J. Lada and E. A. Lada, 2003b)

$$\xi_{\rm lecl}(M_{\rm ecl};r) = K(r)M_{\rm ecl}^{-\beta}, \tag{2.2}$$

where $M_{\rm ecl}$ is the stellar mass of the embedded cluster at birth and $K(r)$ the normalization constant and β the power law index. By observation β was found to be between $\beta = 1.5$ and $\beta = 2.5$ (Weidner, Kroupa and Larsen 2004a and references therein). $K(r)$ has to be estimated using normalization conditions.

The normalization condition is that the entire freshly formed stellar mass of a galactic region has to be in embedded clusters. So integrating the mass over all clusters (from the lower mass limit $M_{\rm ecl,min}$ to the locally upper mass limit $M_{\rm U,loc}(r)$) obtains the freshly formed stellar mass. In the case of an infinitesimally small surface area dA this obtains the embedded cluster mass surface density. This embedded cluster mass surface density is defined as the star formation rate density $\Sigma_{\rm SFR}(r)$ multiplied with the time-scale (δt), the time over which a population of embedded clusters forms. $\Sigma_{\rm SFR}(r)$ is defined as

$$\Sigma_{\rm SFR}(r) = \frac{{\rm dSFR}}{{\rm d}A}\,, \tag{2.3}$$

with SFR being the star formation rate in the whole galaxy.

The total embedded cluster mass density is obtained by multiplying $\Sigma_{\rm SFR}(r)$ with δt (Schulz, Pflamm-Altenburg and Kroupa 2015; Weidner, Kroupa and Larsen 2004a):

$$\Sigma_{\rm SFR}(r)\,\delta t = \int_{M_{\rm ecl,min}}^{M_{\rm U,loc}(r)} M'_{\rm ecl}\xi_{\rm lecl}(M'_{\rm ecl};r){\rm d}M'_{\rm ecl}\,. \tag{2.4}$$

$M_{\rm ecl,min}$ is assumed to be about 5 $M_\odot$, corresponding to the smallest groups of embedded stars observed (Kroupa and Bouvier 2003, Kirk and Myers 2012), and is here assumed to be a constant. δt is roughly 10 Myr, as deduced by Egusa, Sofue and Nakanishi (2004). This is the time it takes for the interstellar medium to transform into a new population of stars and is essentially the lifetime of molecular clouds (Fukui et al. 1999; Yamaguchi et al. 2001; Tamburro et al. 2008). It is essentially the lifetime over which the embedded cluster mass function is fully populated (see the discussion in Kroupa, Weidner, Pflamm-Altenburg et al. 2013b and Schulz, Pflamm-Altenburg and Kroupa 2015).

It is noteworthy that to calculate the LECMF Eq. (2.4) is sufficient once $M_{\rm U,loc}(r)$ is known. The values for $K(r)$ are uniquely defined for different β. For $\beta \neq 2$,

$$K(r) = \frac{\Sigma_{\rm SFR}(r)\,\delta t(2-\beta)}{M_{\rm U,loc}^{2-\beta}(r) - M_{\rm ecl,min}^{2-\beta}}\,. \tag{2.5}$$

For the special case of $\beta = 2$,

$$K(r) = \frac{\Sigma_{\rm SFR}(r)\,\delta t}{\ln\left(M_{\rm U,loc}(r)/M_{\rm ecl,min}\right)}\,. \tag{2.6}$$

A visual verification that a LECMF calculated by this method is in agreement with a LECMF that was obtained by randomly drawing star clusters according to Eq. (2.2) is shown in Fig. 2.1.

The only uncertainty left is the exact form of $M_{\rm U,loc}(r)$. At the moment we can only state that the local upper mass limit has to be smaller than the total upper mass limit of the galaxy $M_{\rm U}$: $M_{\rm U,loc}(r) \leq M_{\rm U}$. Therefore additional research into this subject is necessary (see Sec. 2.3.1).

The LECMF with an observable non-infinitesimal surface area ΔA is discussed in Appendix A.1.

2.3 The Galaxy-Wide Embedded Cluster Mass Function

In this section the scope of our analysis is to describe the form of the ECMF after integrating over the axis-symmetric galactic disk surface area. The previous formulae allow the normalisation of the LECMF at a fixed distance to the center of a galaxy.

The galaxy wide or integrated ECMF (IECMF or $\xi_{\rm iecl}$, not to be confused with the LECMF $\xi_{\rm lecl}$ above) is defined as the number of star clusters in the stellar mass interval $M_{\rm ecl}$ to $M_{\rm ecl} + {\rm d}M_{\rm ecl}$

$$\xi_{\rm iecl}(M_{\rm ecl})\,{\rm d}M_{\rm ecl} = {\rm d}N_{\rm ecl}\,, \tag{2.7}$$

or

$$\begin{aligned}\xi_{\rm iecl}(M_{\rm ecl}) &= \int_0^{2\pi}\int_0^{R'(M_{\rm ecl})} \xi_{\rm lecl}(M_{\rm ecl};r)\,r\,{\rm d}r{\rm d}\phi \\ &= \int_0^{2\pi}\int_0^{R'(M_{\rm ecl})} K(r)M_{\rm ecl}^{-\beta} r\,{\rm d}r{\rm d}\phi\,.\end{aligned} \tag{2.8}$$

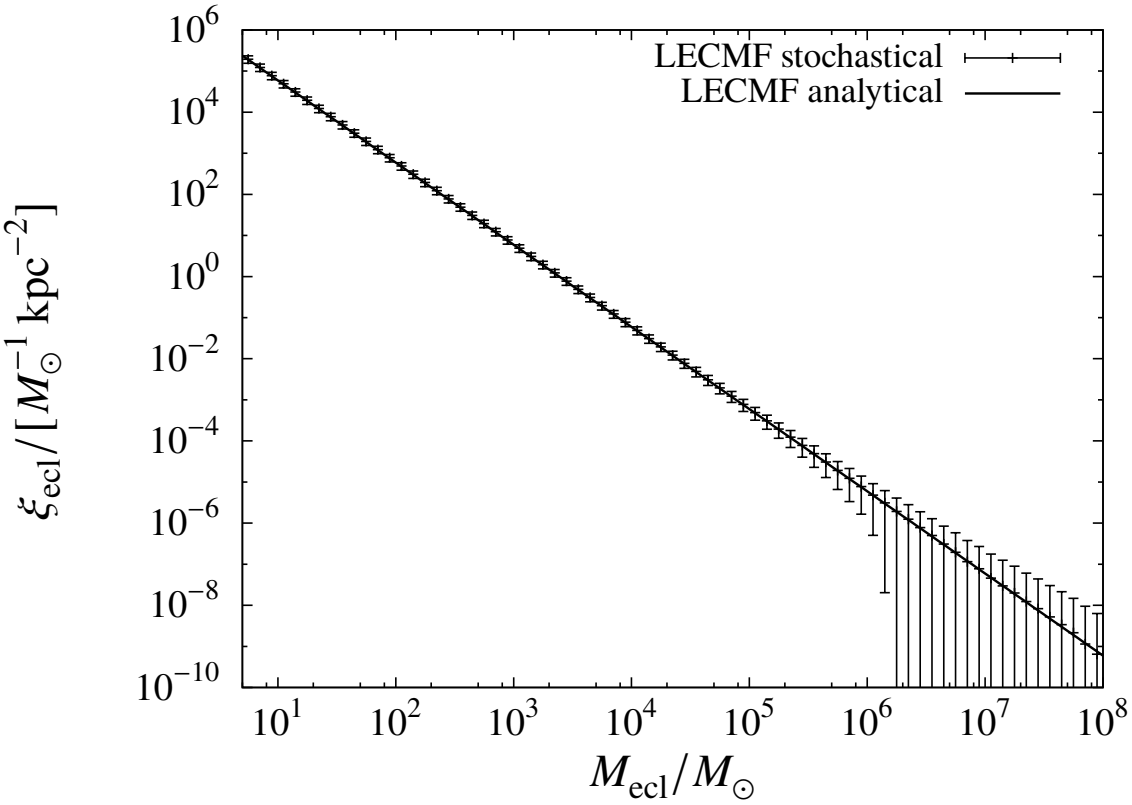

Figure 2.1: An exemplary LECMF. Shown here is a LECMF from the distribution function given by Eq. (2.2) for a galactic region with $10^8\ M_\odot$ of stellar mass. Further we assumed a $M_{\rm ecl,min}$ of 5 $M_\odot$ and a $M_{\rm U,loc}(r)$ of $10^8\ M_\odot$. The solid line shows the LECMF calculated analytically, whereas the points are the binned results of stochastic sampling.

with $R'(M_{\rm ecl})$ being the maximal galactocentric distance at which an embedded cluster of mass $M_{\rm ecl}$ can form, assuming the maximum cluster mass decreases monotonically with increasing radial distance.

Is the IECMF still similar to a power-law function of the cluster mass? And if yes, does the power-law parameter β differ from the local one? To answer these questions one first has to look at the available information.

The galaxy wide star formation rate (SFR)

$$\mathrm{SFR} = \int_0^{2\pi} \int_0^{R_{\rm gal}} \Sigma_{\rm SFR}\, r\, \mathrm{d}r\mathrm{d}\phi\,, \tag{2.9}$$

with $R_{\rm gal}$ being the radius of the star forming area of the the galaxy. In order to obtain $\xi_{\rm iecl}$ one can insert Eq. (2.4) into Eq. (2.9). The resulting equation (see also Kroupa, Weidner, Pflamm-Altenburg

et al. 2013b) is:

$$\begin{aligned} \mathrm{SFR}\,\delta t &= \int_0^{2\pi}\int_0^{R_{\rm gal}}\int_{M_{\rm ecl,min}}^{M_{\rm U,loc}(r)} M_{\rm ecl}\xi_{\rm lecl}(M_{\rm ecl};r)\mathrm{d}M_{\rm ecl}r\mathrm{d}r\mathrm{d}\phi \\ &= \int_0^{2\pi}\int_0^{R_{\rm gal}}\int_{M_{\rm ecl,min}}^{M_{\rm U,loc}(r)} K(r)M_{\rm ecl}^{1-\beta}r\,\mathrm{d}M_{\rm ecl}\mathrm{d}r\mathrm{d}\phi\,. \end{aligned} \tag{2.10}$$

Eq. (2.10) is first an integration over the mass of the clusters and then over the area. It is possible to exchange the mass intgral with the integral over the galactocentric distance by noting that in a given annulus the theoretical most massive cluster $M_{\rm U,loc}(r)$ depends on r, that is, we can invert this function to obtain the galactocentric distance $R'(M_{\rm ecl})$ at which the annulus contains a particular theoretical most massive cluster. In other words to exchange the positions of the r- and $M_{\rm ecl}$-integration. Assuming that the mass of the theoretical most massive cluster possible, $M_{\rm U}(r)$, decreases with the galactocentric distance r then the integration needs only to extend over the distances 0 to $R'(M_{\rm ecl}) \leq R_{\rm gal}$. Therewith at the low mass end the IECMF is an integral over 0 to $R_{\rm gal}$, while at the high mass end large radii do not contribute:

$$\mathrm{SFR}\,\delta t = \int_{M_{\rm ecl,min}}^{M_{\rm U}}\int_0^{2\pi}\int_0^{R'(M_{\rm ecl})} K(r)M_{\rm ecl}^{1-\beta}r\,\mathrm{d}r\mathrm{d}\phi\mathrm{d}M_{\rm ecl}\,. \tag{2.11}$$

Both $K(r)$ and $M_{\rm U,loc}(r)$ are not known for a specific r. $K(r)$ depends on $\Sigma_{\rm SFR}$, see Eq. (2.4).

A direct relation between $\Sigma_{\rm SFR}$ and the position within the galaxy, assumed to be valid for a galaxy in self-regulated equilibrium, is taken from Pflamm-Altenburg and Kroupa (2008b):

$$\begin{aligned} \Sigma_{\rm SFR}(x,y) &= \frac{\mathrm{SFR}\;e^{R_{\rm gal}/r_d}}{2\pi r_d^2\left(e^{R_{\rm gal}/r_d}-\frac{R_{\rm gal}}{r_d}-1\right)}e^{-r/r_d} \\ &\approx \frac{\mathrm{SFR}}{2\pi r_d^2}e^{-r/r_d}\,. \end{aligned} \tag{2.12}$$

In this case r_d is the disc scale length. The equation is normalised in such a way that an integral over the whole area results in the total SFR. Therefore both sides of Eq. (2.12) can be multiplied with δt so that it is equal to Eq. (2.4) (in the following we will write SFR δt as $M_{\rm tot}$, the total stellar mass formed galaxy wide in time δt):

$$\int_{M_{\rm ecl,min}}^{M_{\rm U,loc}(r)} M'_{\rm ecl}\xi_{\rm lecl}(M'_{\rm ecl})\mathrm{d}M'_{\rm ecl} = \frac{M_{\rm tot}}{2\pi r_d^2}e^{-r/r_d}\,. \tag{2.13}$$

This gives a relation between $K(r)$ and $M_{\rm U,loc}(r)$. For $\beta \neq 2$:

$$K(r) = \frac{(2-\beta)\,M_{\rm tot}}{2\pi r_d^2\left(M_{\rm U,loc}^{2-\beta}(r) - M_{\rm ecl,min}^{2-\beta}\right)}e^{-r/r_d}\,. \tag{2.14}$$

For $\beta = 2$:

$$K(r) = \frac{M_{\rm tot}}{2\pi r_d^2\ln\left(M_{\rm U,loc}(r)/M_{\rm ecl,min}\right)}e^{-r/r_d}\,. \tag{2.15}$$

To get an unambiguous expression for $K(r)$ and $M_{\rm U,loc}(r)$ more constraints are needed. For this purpose we are going to use a model (henceforth called the exponential model) based on an ansatz

from Pflamm-Altenburg and Kroupa (2008b). Other possible models, found to be not working as well as this one, are dicussed in the Appendix A.3.

2.3.1 Exponential Model

Pflamm-Altenburg and Kroupa (2008b) propose the ansatz that the radial dependence of $M_{\rm ecl,max,loc}(r)$ should have the same form, as the radial dependence of the gas surface density $\Sigma_{\rm gas}(r)$:

$$\Sigma_{\rm gas}(r) = \Sigma_{\rm gas,0}\, e^{-\frac{r}{r_d}}\,, \tag{2.16}$$

with $\Sigma_{\rm gas,0}$ being the gas surface density at the center of the galactic disk. Thus

$$M_{\rm ecl,max,loc}(r) = M_{\rm ecl,max}\, e^{-\frac{r}{r_d}}\,. \tag{2.17}$$

With this ansatz they were able to show that the Hα radial cutoff in disk galaxies is naturally explained, given that star formation extends well beyond this cutoff radius.

As our model uses $M_{\rm U,loc}$ instead of $M_{\rm ecl,max}$, we modify Eq. (2.17) to

$$M_{\rm U,loc}(r) = M_{\rm U} e^{-\frac{r}{r_d}}\,. \tag{2.18}$$

Inserting Eq. (2.18) into Eq. (2.13) with $\beta \neq 2$ results in a definite $K(r)$:

$$K(r) = \frac{(2-\beta)\, M_{\rm tot}}{2\pi r_d^2 \left[\left(M_{\rm U} e^{-\frac{r}{r_d}}\right)^{2-\beta} - M_{\rm ecl,min}^{2-\beta}\right]} e^{-r/r_d}\,, \tag{2.19}$$

and for $\beta = 2$ in

$$K(r) = \frac{M_{\rm tot}}{2\pi r_d^2 \ln\left[\left(M_{\rm U} e^{-\frac{r}{r_d}}\right)/M_{\rm ecl,min}\right]} e^{-r/r_d}\,. \tag{2.20}$$

For each r in the axis-symmetric disk galaxy there is a theoretical maximal cluster mass $M_{\rm U,loc}(r)$. Regarding the entire galaxy, each $M_{\rm U,loc}(r)$ is a theoretical possible cluster mass $M_{\rm ecl}$. And in this relation r is the maximal galactocentric distance $R'(M_{\rm ecl})$, at which a cluster of mass $M_{\rm ecl}$ can still be found. This is true for every $M_{\rm ecl}$, $R'(M_{\rm ecl})$ being the reverse function of $M_{\rm U,loc}(r)$. $R'(M_{\rm ecl})$ is needed for Eq. (2.11),

$$R'(M_{\rm ecl}) = -r_d \ln\left(\frac{M_{\rm ecl}}{M_{\rm U}}\right)\,. \tag{2.21}$$

Now $\xi_{\rm iecl}(M_{\rm ecl})$ can be calculated:

$$\xi_{\rm iecl}(M_{\rm ecl}) = \int_0^{2\pi}\int_0^{R'(M_{\rm ecl})} K(r) M_{\rm ecl}^{-\beta}\, r\, {\rm d}r{\rm d}\phi\,. \tag{2.22}$$

This integration can only be solved numerically (because of the r-dependence in $K(r)$). The remaining free parameters (β and $M_{\rm U}$) can be fixed using empirical data. Weidner, Kroupa and Larsen (2004a) derived a fitting function for the mass of the most massive very young cluster in a galaxy ($M_{\rm vyc,max}$)

depending on the SFR of the host galaxy:

$$M_{\rm vyc,max} = k_{\rm ML} \cdot {\rm SFR}^{0.75(\pm0.03)} \cdot 10^{6.77(\pm0.02)}, \tag{2.23}$$

with $k_{\rm ML}$ being the mass-to-light ratio, which can be assumed to be 0.0144 for young (< 6 Myr) clusters. $M_{\rm vyc,max}$ is a good approximation for the mass of the most massive embedded star cluster of a galaxy, $M_{\rm ecl,max}$.

To determine $M_{\rm ecl,max}$ we use two conditions: first there is only one most massive cluster. Second the mass of the most massive cluster is $M_{\rm ecl,max}$.

To implement the first condition we choose a mass interval between the upper mass limit $M_{\rm U}$ and $M_{\rm ecl,t}$, with $M_{\rm ecl,t}$ chosen in such a way that there is only one cluster between these limits:

$$1 = \int_{M_{\rm ecl,t}}^{M_{\rm U}} \xi_{\rm iecl}(M'_{\rm ecl}){\rm d}M'_{\rm ecl}\,. \tag{2.24}$$

The second condition implies that the mass between these limits is $M_{\rm ecl,max}$:

$$M_{\rm ecl,max} = \int_{M_{\rm ecl,t}}^{M_{\rm U}} M'_{\rm ecl}\xi_{\rm iecl}(M'_{\rm ecl}){\rm d}M'_{\rm ecl}\,. \tag{2.25}$$

As $M_{\rm ecl,max}$ depends on SFR it therewith follows that also $M_{\rm U}$ depends on SFR. Note that these conditions differ from those employed on previous occasions, as explained in Appendix A.2.

Using these we can find for every β a SFR-$M_{\rm ecl,max}$-curve that aligns with Eq. (2.23). In order to narrow β down, a fitting $M_{\rm U}$ is needed. $M_{\rm U}$ is supposed to be larger than any observed cluster mass but not so large that there would be unrealistic gaps between the mass of the most massive clusters and $M_{\rm U}$. With that we find for $\beta = 2.3 \pm 0.1$ and $\delta t = 10$ Myr a SFR-$M_{\rm ecl,max}$-curve that aligns with Eq. (2.23) and resulting $M_{\rm U}$ that fulfils the above criteria (see also Fig. 2.2).

2.4 Comparison to Empirical Data

We already used empirical data in Sec. 2.3.1 to align the SFR-$M_{\rm ecl,max}$-curve of the exponential model with the empirical fit by Weidner, Kroupa and Larsen (2004a) (Eq. 2.23) and in doing so constrained the free parameters of the model. In the following we want to determine whether the model, using said constraints, is also in reasonable agreement with other observations.

Empirical data has been indicating that the galaxy-wide ECMF should be a Schechter-function (Gieles et al., 2006a), i.e.

$$\xi_{\rm iecl,\,Schechter}(M_{\rm ecl}) = K' e^{-M_{\rm ecl}/M_{\rm c}} M_{\rm ecl}^{-\beta'}\,. \tag{2.26}$$

[1] In order to calculate $M_{\rm vyc,max}$ from the observed absolute magnitude ($M_{\rm V}$) the following formula has been used (Abdullah private communication):

$$M_{\rm V} = 4.79 - 2.5\log_{10}\frac{M_{\rm ecl,max}}{k_{\rm ML}}\,,$$

with $k_{\rm ML}$ being the mass to light ratio.

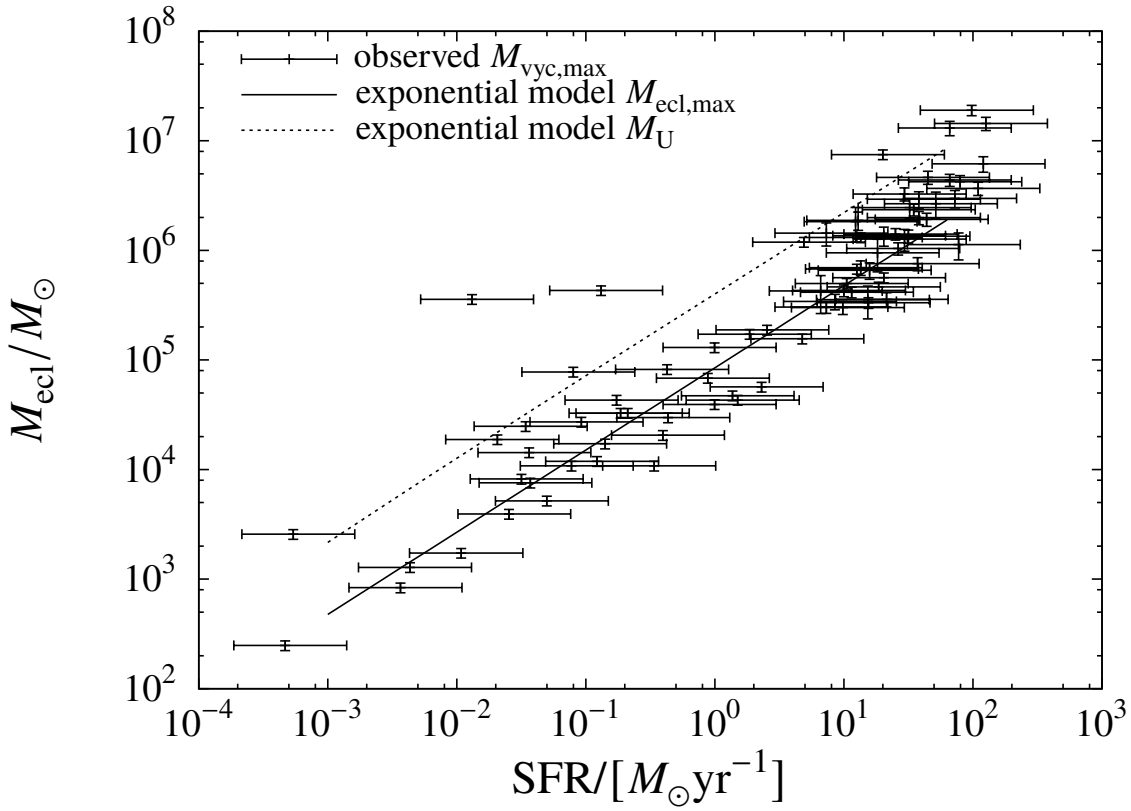

Figure 2.2: The observational data was taken from Weidner, Kroupa and Larsen (2004a) for $M_{\rm vyc,max} < 2{\cdot}10^5\,M_\odot$ and Randriamanakoto et al. (2013)[1] for $M_{\rm vyc,max} > 2\cdot 10^5\,M_\odot$ and shows the observed galaxy-wide most massive very young clusters $M_{\rm vyc,max}$ (which are a good approximation for $M_{\rm ecl,max}$) in dependence of SFR. Also plotted here is $M_{\rm ecl,max}$ and $M_{\rm U}$, as calculated using the model from Sec. 2.3.1 for $\beta = 2.3$ against the galaxy-wide SFR. All observed clusters should be below the $M_{\rm U}$-line, which is mostly the case given the uncertainties.

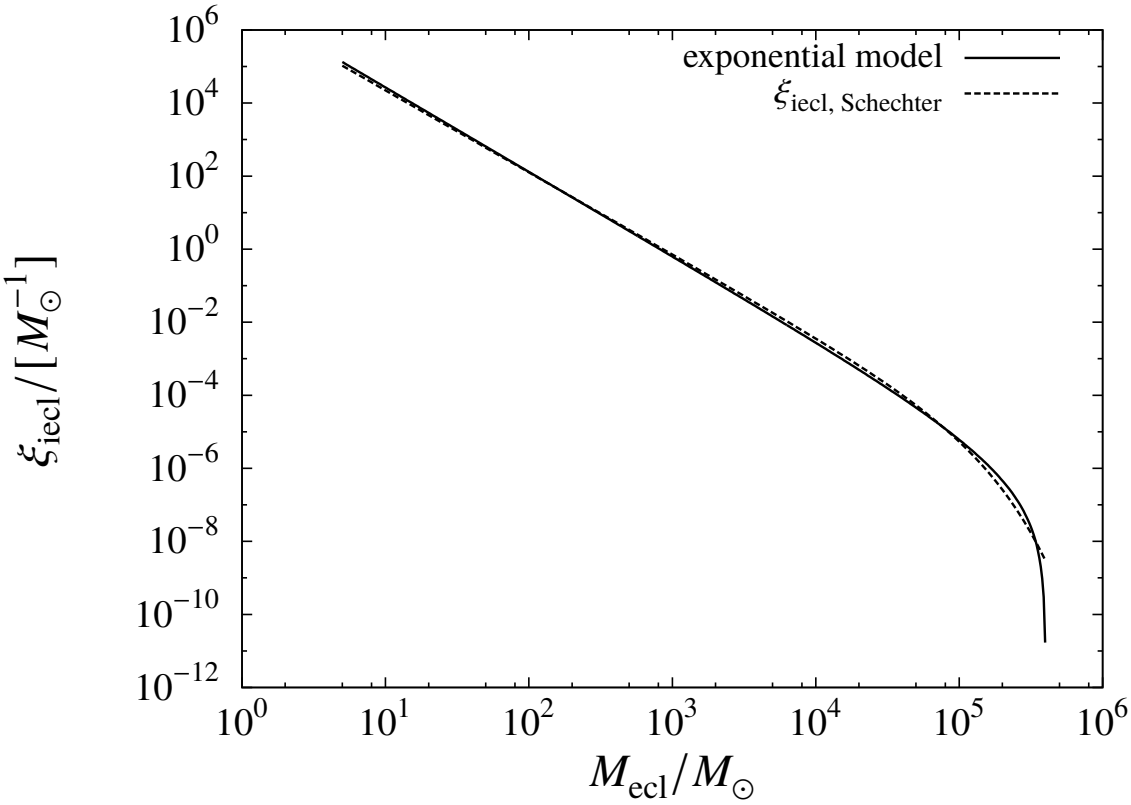

Figure 2.3: A comparison between the ECMF acquired from the exponential model (the solid line) and the ECMF from the Schechter form (Eq. 2.26, the dashed line) for SFR = 1 $M_\odot$/yr and a δt = 10 Myr. For the exponential model $\beta = 2.3$, while for the $\xi_{\mathrm{iecl,\ Schechter}}$ model $\beta = 2.24$.

In this case M_{c} is the turn-down mass,at which the ECMF turns down. Our formalism results in a similar form for the ECMF as the Schechter form. This is shown in Fig. 2.3.

Up until now no theoretical formulation existed which allowed M_{c} to be predicted from properties of the galaxy. Wth our formulation we can derive the turn-down mass in dependence of the exponential density profile of the galaxy.

Fitting the Schechter-function to the exponential model allows us to determine a relation between M_{c} and the SFR:

$$M_{\mathrm{c}} = (85000 \pm 5000)\ \mathrm{SFR}^{(0.73\pm0.02)}\ . \tag{2.27}$$

Comparing this to Eq. (2.23) shows that these two equations are the same within the uncertainties. Therefore $M_{\mathrm{c}} = M_{\mathrm{ecl,max}}$ is at least a good approximation.

While β has roughly the same effect in the Schechter formalism as it has for the LECMF (Eq. (2.2)), meaning that β describes the slope of the curve if viewed logarithmically, this is not true for the theoretically calculated IECMFs.

This means that for a specific β the slope of the LECMF (which is just β in the logarithmic case) is not equal to the slope of the IECMF. Thus the slope changes when viewing areas of different sizes ($\pi R^2(M_{\mathrm{ecl}})$) in the same galaxy. This could be one of the reasons why it was not possible to get a

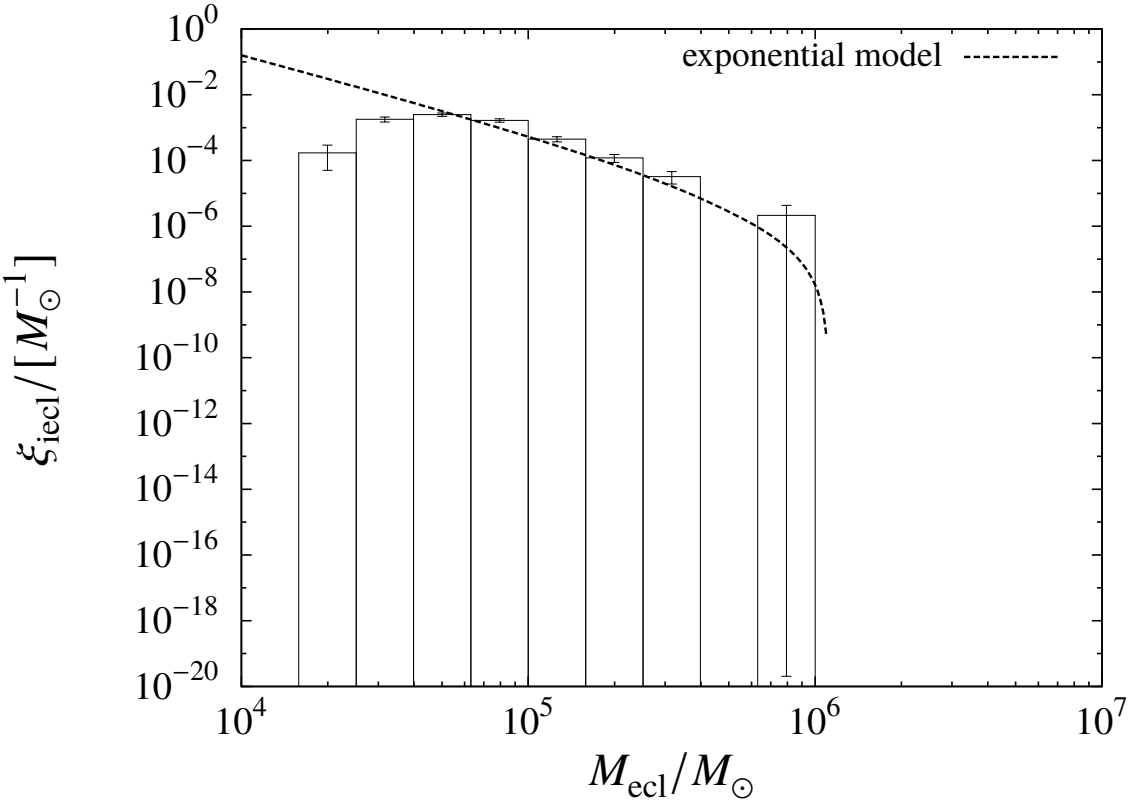

Figure 2.4: Combined binned young cluster mass function for two galaxies (NGC 5236 and NGC 6946, data taken from Larsen 1999 and Larsen private communication). Also shown is the exponential model. For the single galaxies see Figs. 2.5 and 2.6.

unique value for β.

Next we compare the exponential model to actual empirical data. For this we confront the model with galaxy-wide observations of NGC 5236 and NGC 6946 (data taken from Larsen 1999 and Larsen private communication). The empirical data consists of a list of cluster masses, which were binned. To compare these data to the models we need the SFRs of the galaxies. Dopita et al. (2010) calculated a SFR of 2.76 $M_\odot$/yr for NGC 5236, whereas Hong et al. (2013) determined SFRs of 1.52 and 0.18 $M_\odot$/yr, depending on the method used. For NGC 6946 Heesen et al. (2014) measured, depending on the method, a SFR of 4.635 ± 0.232 and 3.497 ± 0.175 $M_\odot$/yr. For our models we are therefore assuming SFR = 1.5 $M_\odot$/yr for NGC 5236 and SFR = 4 $M_\odot$/yr for NGC 6946. A comparison of the data to the combined $\xi_{\rm iecl}$ calculated using the exponential model is shown in Fig. 2.4. The only difference between the IECMF models that has been applied here are the differing galaxy-wide SFRs. As $\xi_{\rm lecl} \propto K \propto \delta t$ a change in δt does not change the overall behaviour of the function. All other parameters are identical to the fit from Fig. 2.2. The exponential model fits reasonably well to the data. We can also compare the model to the individual galaxies (Figs. 2.5 and 2.6) but this has the disadvantage of having higher uncertainties. Nonetheless the model fits quite well, given the uncertainties.

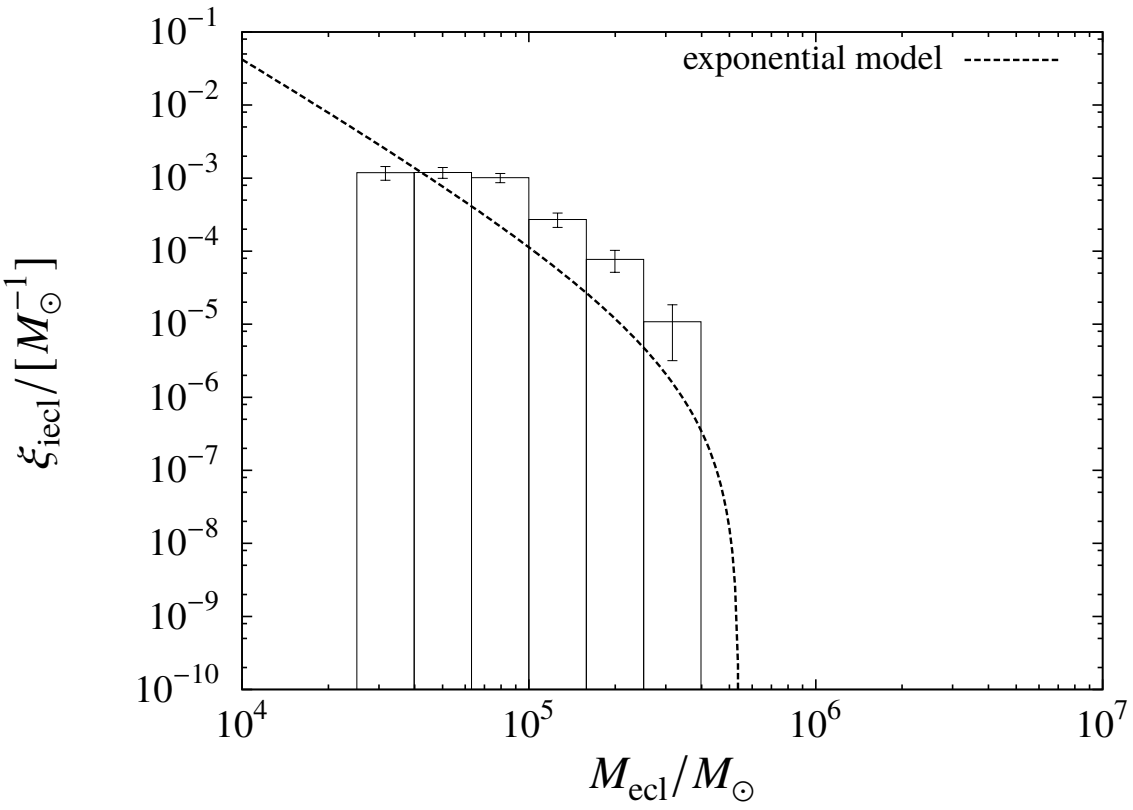

Figure 2.5: Binned young cluster mass function for NGC 5236 (data taken from Larsen 1999 and Larsen private communication). Also shown is the exponential model for SFR = 1.5 $M_\odot$/yr. See text for further details.

The r-dependency of $M_{\rm U,loc}(r)$ is also a crucial part to the usability of the exponential model. We compare the theoretical $M_{\rm U,loc}$-r dependence with the observed very young star clusters in M33 (data taken from Pflamm-Altenburg, González-Lópezlira and Kroupa 2013b) in Fig. 2.7. Fig. 2.7 shows the r-dependence of $M_{\rm U,loc}$ for the model compared to observed very young star clusters. As $M_{\rm U,loc}$ is the upper mass limit for star clusters at a given galactocentric distance we would expect that no observed cluster is heavier than it. But several observed ones are. Also using the observed SFR (0.16 $M_\odot$/yr, Skibba et al. 2011) in the empirical fit by Weidner (Eq. 2.23) results in a $M_{\rm vyc,max}$ much smaller than several observed clusters. But taking into account that individual cluster masses have large uncertainties it becomes apparent that the exponential model fits quite well to the observed decreasing upper masses.

2.5 Conclusion

In this chapter we calculated for the first time the galaxy-wide integrated embedded cluster mass function for galaxies, which we assumed to be axis-symmetric exponential disks, and showed that it has the form of a Schechter-like function, although locally the ECMF is a pure power-law.

To do that we first described an analytical solution of the LECMF. It was assumed there that the

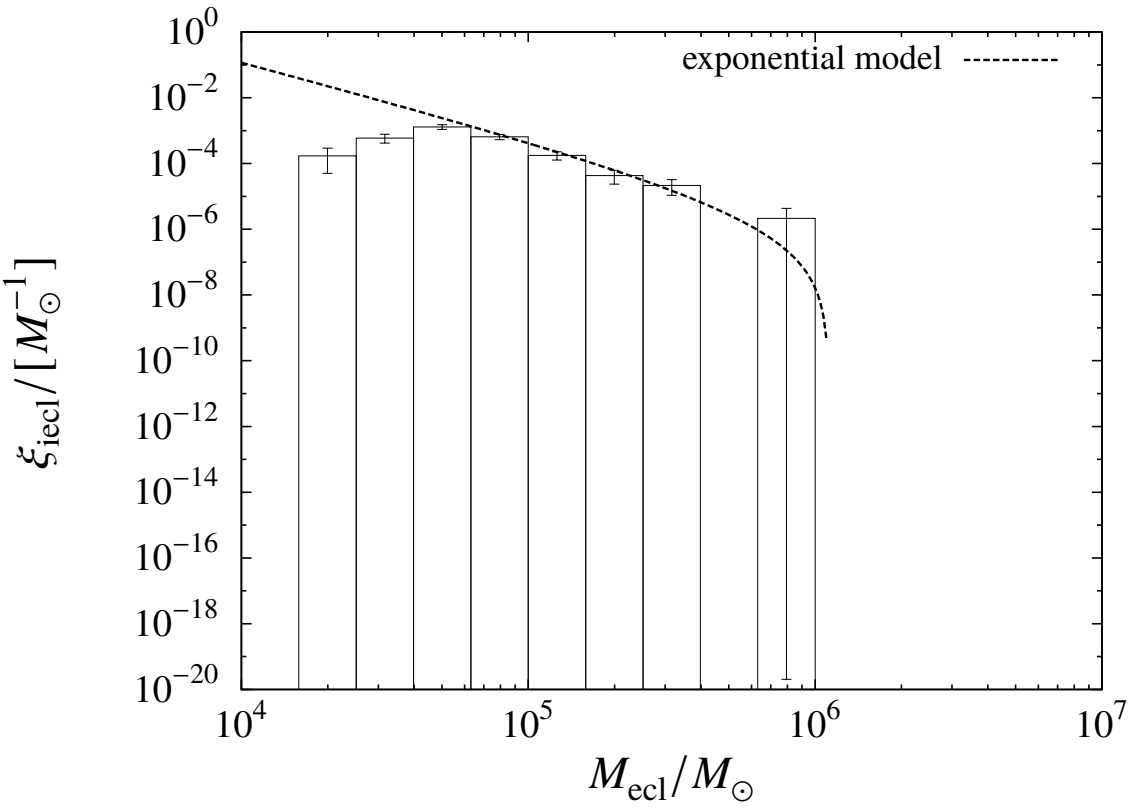

Figure 2.6: Binned young cluster mass function for NGC 6946 (data taken from Larsen 1999 and Larsen private communication). Also shown is the exponential model for SFR = 4 $M_\odot$/yr. See text for further details.

theoretical local upper cluster mass limit, $M_{\rm U,loc}(r)$, depends on the galactocentric distance r.

Integrating the LECMF over the area of the star forming disk yields the galaxy-wide or integrated embedded cluster mass function (IECMF or $\xi_{\rm iecl}$). For this purpose a model describing the r-dependence of $M_{\rm U,loc}(r)$ was needed. The exponential model, introduced by Pflamm-Altenburg and Kroupa (2008b), is found to be in agreement with observational data.

Even though the LECMF is a power law, the IECMF resembles a Schechter-like function, the reason being that the upper mass limit of the local power law is defined by $M_{\rm U,loc}(r)$, which decreases with an increasing galactocentric distance.

Additionally given a locally estimated power-law index β for an ensemble of embedded clusters in a region in a galaxy, we have shown here that other regions elsewhere are expected to have different logarithmic ECMF, depending on the size and position of the region in the galaxy, and that the size of the region implies a Schechter-type turn-down of the embedded cluster mass function. Even more importantly, the logarithmic slope of the observed ECMF depends on the size of the observed region and is not equal to β. This could be one of the reasons for the spread of observationally determined β. The galaxy-wide ECMF, the integrated ECMF, IECMF, thus becomes a Schechter-type form.

All of this opens further possibilities for new research. As has been stated, the exponential model depends on the theoretical upper limit for the mass of clusters in a galaxy of a specific stellar mass. At

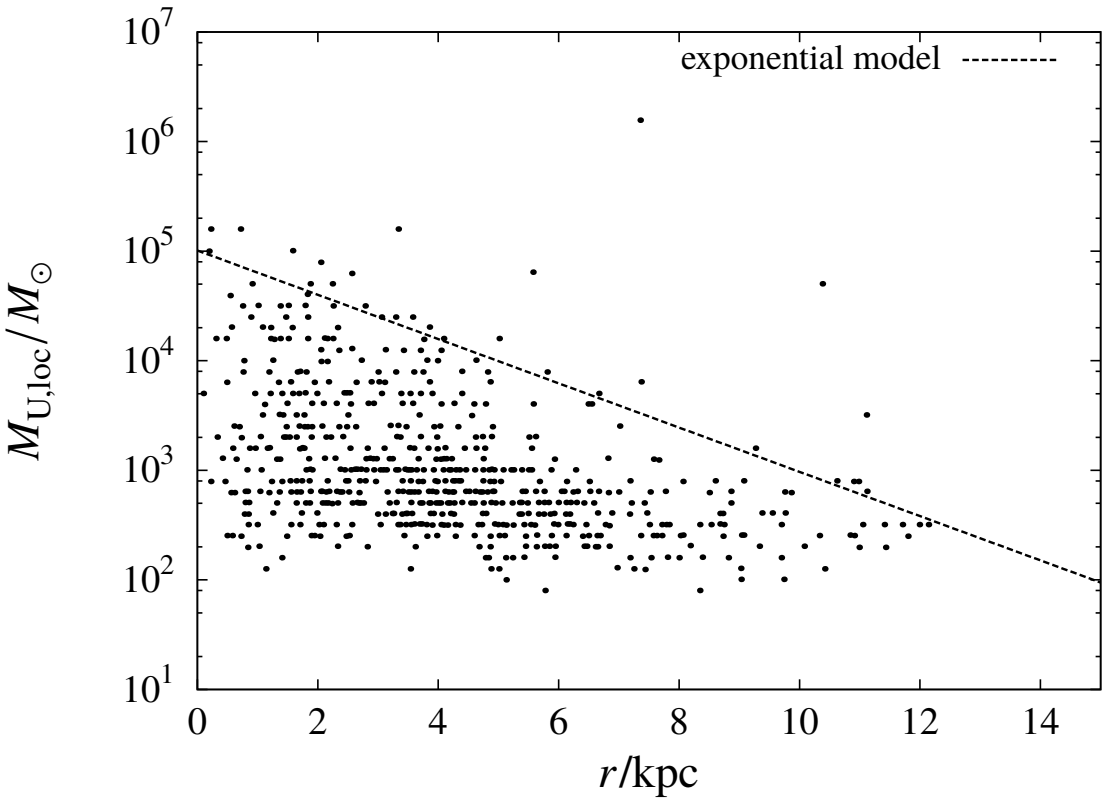

Figure 2.7: Comparison of the dependence on the galactocentric distance of $M_{\mathrm{U,loc}}$ for the exponential model with observed very young clusters in M33 (Pflamm-Altenburg, González-Lópezlira and Kroupa, 2013b). M33 has a SFR of about 0.16 $M_\odot$/yr (Skibba et al., 2011). Therefore the model uses SFR = 0.16 $M_\odot$/yr, δt = 10 Myr and β = 2.31. These values have been chosen so that the model fits the experimental data from the SFR-$M_{\mathrm{ecl,max}}$ relation (Fig. 2.2).

the moment we can only give a lower limit to these values, which could underestimate them. Further research in the context of star and cluster formation should be able to give improved insights on the theoretical upper mass limits.

Another step, which has to be done, would be to combine the stellar initial mass function (IMF) and the ECMF into the integrated galactic initial mass function (IGIMF) (Weidner, Kroupa, Pflamm-Altenburg et al. 2013, Recchi and Kroupa 2015), which is the galaxy-wide stellar initial mass function.

Acknowledgements

We thank the referee for helpful comments and Søren S. Larsen for providing us with valuable data regarding the galaxies NGC 5236 and NGC 6946. We are also grateful to Jan Pflamm-Altenburg for providing data on M33 and for useful discussions.

CHAPTER 3

The Kennicutt-Schmidt law and the main sequence of galaxies in Newtonian and Milgromian Dynamics

This chapter is based on an upcoming publication with the same title "The Kennicutt-Schmidt law and the main sequence of galaxies in Newtonian and Milgromian Dynamics". Only minor changes concerning formatting were made in order to present it as a chapter in the thesis.

Abstract The Kennicutt-Schmidt law is an empirical relation between the star formation rate surface density ($\Sigma_{\rm SFR}$) and the gas surface density ($\Sigma_{\rm gas}$) in disk galaxies. According to this law, the relation has the form of a power law $\Sigma_{\rm SFR} \propto \Sigma_{\rm gas}^{n}$. Assuming that star formation results from the gravitational collapse of the interstellar medium, $\Sigma_{\rm SFR}$ can be determined by dividing $\Sigma_{\rm gas}$ by the local free-fall time $t_{\rm ff}$. The formulation of $t_{\rm ff}$ yields the relation between $\Sigma_{\rm SFR}$ and $\Sigma_{\rm gas}$, assuming that a fraction ($\varepsilon_{\rm SFE}$) of gas is converted into stars every $t_{\rm ff}$. This is done here for the first time using Milgromian Dynamics (MOND). Using linear stability analysis of a uniformly rotating thin disk, it is possible to determine the size of a collapsing perturbation within a galactic disk. Therefore, it is possible to evaluate the size and mass of clouds (and free-fall time $t_{\rm ff}$) in dependence of $\Sigma_{\rm gas}$. This allows us to identify the relation between $\Sigma_{\rm SFR}$ and $\Sigma_{\rm gas}$.

We analytically derive the relation $\Sigma_{\rm SFR} \propto \Sigma_{\rm gas}^{n}$ both in Newtonian and Milgromian dynamics, finding that $n = 1$. The differences between the two cases are only a change to the constant pre-factor, resulting in increased $\Sigma_{\rm SFR}$ of up to 25% using MOND. A near exact representation of the present-day main sequence of galaxies is obtained if $\epsilon_{\rm SFE}$ = constant $\approx$ 1.3% We also show that empirically found correction terms to the Kennicutt-Schmidt law are included in the here presented relation. Furthermore, we determine that if star formation is possible, the temperature only affects $\Sigma_{\rm SFR}$ by up to a factor of $\sqrt{2}$.

3.1 Introduction

The relation between the star formation rate surface density ($\Sigma_{\rm SFR}$) and the gas surface density ($\Sigma_{\rm gas}$) was first proposed by Schmidt (1959), who examined the Milky Way and found this relation (then

known as the Schmidt-law) to be a power-law of the form

$$\Sigma_{\rm SFR} \propto \Sigma_{\rm gas}^{n}\,, \tag{3.1}$$

with $n \approx 2$. Kennicutt (1989) determined $n \approx 1.4$ from Hα observations of 7 galaxies. This relation became known as the Kennicutt-Schmidt law. Further, Kennicutt (1989) found that star formation appears to cease where the Toomre stability criterion for a gas disk (Toomre, 1964) indicates star formation to be impossible.

Since then, a value of $n \approx 1.5$ has become accepted and also supported by observations (see e.g. Heyer et al. 2004; A. Leroy et al. 2005; Kennicutt et al. 2007), forming the basis for both theoretical and simulation work (see e.g. Schaye and Dalla Vecchia 2008).

On the other hand, ultraviolet observations (Boissier et al., 2007) find a value of $n = 0.99$. Ultraviolet observations are less sensitive to the presence of young, very massive stars and are therefore more likely to derive a value of n close to the true one. Furthermore Pflamm-Altenburg and Kroupa (2008a) support $n = 1$ through the radially changing initial mass function of stars expected in the integrated galactic initial mass function (IGIMF) theory (Kroupa and Weidner 2003; Kroupa, Weidner, Pflamm-Altenburg et al. 2013a). In view of the discrepancy between $n = 1.5$ and $n = 1$, we readdress this problem within the basics of star formation in a galactic disk.

The aim of this chapter is to derive the Kennicutt-Schmidt law from a basic description using the free-fall time as an approximation for the time the gas needs to collapse into stars. This principal idea has already been explored by e.g. Krumholz and McKee (2005). In contrast to their work, our approach is completely two-dimensional – we do not mix a two-dimensional surface density and a three dimensional free-fall time. This is achieved by assuming that the collapsing area of the disk can be calculated using a thin disk stability analysis. Furthermore, our chapter will for the first time derive the Kennicutt-Schmidt law using Milgromian Dynamics.

3.1.1 Milgromian Dynamics

Milgromian Dynamics (MOND, Milgrom, 1983c) is as an alternative to a dark matter dominated universe deduced from the flattening of observed rotation curves, which are in contrast to classical Newtonian models without dark matter. MOND is a space-time invariance symmetry of the equations of motion (Milgrom 1983c; see also Wu and Kroupa 2015) and may be an effect of the physical quantum vacuum (Milgrom 1999; Smolin 2017).

MOND as derived from a classical Lagrangian (Bekenstein and Milgrom, 1984) introduces the natural constant $a_0 = 1.2 \times 10^{-10}\,{\rm m/s^2}$ and states that if the Newtonian gravitational acceleration $g_{\rm N} \gg a_0$, the Newtonian gravitational description should be used but if $g_{\rm N} \ll a_0$, the gravitational acceleration g becomes in spherical symmetry

$$g = \frac{\sqrt{GMa_0}}{R}\,. \tag{3.2}$$

In other words, if the distance to an object is much larger than its MOND radius $R_{\rm M}$, which follows from Eq. (3.2) for $g = a_0$:

$$R_{\rm M} = \sqrt{\frac{GM}{a_0}}\,, \tag{3.3}$$

then the gravitational acceleration will be given by Eq. 3.2.

Milgrom (1983c) developed an algebraic approximation for the gravitational acceleration g:

$$g = g_{\rm N}\nu\left(\frac{g_{\rm N}}{a_0}\right), \tag{3.4}$$

with $\nu(x)$ being the so-called interpolation function (shown to be derivable from the quantum vacuum, see Milgrom 1999) fulfilling the following conditions: $(x \gg 1 \mid \nu(x) = 1)$ and $\left(x \ll 1 \mid \nu(x) = \sqrt{1/x}\right)$. So, for example, in the case of a single point mass ($g_{\rm N} = GM/R^2$) Eq. (3.4) would become

$$g = \frac{GM}{R^2}\nu\left(\frac{GM}{a_0R^2}\right). \tag{3.5}$$

There are three well-defined extreme cases of MOND. Firstly, if $g_{\rm N} \gg a_0$, we have the Newtonian case, where ν becomes 1 and the gravitational acceleration $g_{\rm N}$ becomes according to Eq. 3.5

$$g(g_{\rm N} \gg a_0) = g_{\rm N} = \frac{GM}{R^2}, \tag{3.6}$$

which is the classical Newtonian description. Secondly, an isolated point mass with $g_{\rm N} \ll a_0$ constitutes the isolated deep-MOND limit, where $\nu(x) = \sqrt{1/x}$ and the gravitational acceleration ($g_{\rm idM}$) becomes, according to Eq. 3.5,

$$g_{\rm idM} = \sqrt{a_0 g_{\rm N}} = \frac{\sqrt{GMa_0}}{R}. \tag{3.7}$$

Finally, if the point mass is not isolated and the gravitational acceleration of an external field ($g_{\rm ext,N}$) is much larger than the internal gravitational field ($g_{\rm int,N}$) but still much smaller than a_0, so $g_{\rm int,N} \ll g_{\rm ext,N} \ll a_0$, then the quasi-Newtonian regime results. The quasi-Newtonian regime needs a different algebraic interpolation function (Banik and Zhao, 2018b):

$$g = g_{\rm N}\nu\left(\frac{g_{\rm N}}{a_0}\right)\left(1 + \frac{K}{3}\right), \tag{3.8}$$

with

$$K = \left.\frac{d\log\nu(x)}{d\log x}\right|_{x=g_N/a_0}. \tag{3.9}$$

In the extreme case of the Quasi-Newtonian regime, $\nu = \sqrt{a_0/g_{\rm ext,N}}$ and $K = -\frac{1}{2}$, accordingly $\left(1 + \frac{K}{3}\right) = \frac{5}{6}$ and the gravitational acceleration ($g_{\rm QN}$) therefore becomes:

$$g_{\rm QN} = \frac{5}{6}\sqrt{\frac{a_0}{g_{\rm ext,N}}}g_{\rm int,N} = \frac{5}{6}\sqrt{\frac{a_0}{g_{\rm ext,N}}}\frac{GM}{R^2} \tag{3.10}$$

To summarize: Eq. 3.4 is valid for isolated objects while Eq. 3.8 should be used if the external gravitational field is much stronger than the internal one.

Note that if either $g_{\rm ext,N}$ or $g_{\rm int,N}$ or the combined Newtonian acceleration $g_{\rm N} = \sqrt{g_{\rm int,N}^2 + g_{\rm ext,N}^2}$ is

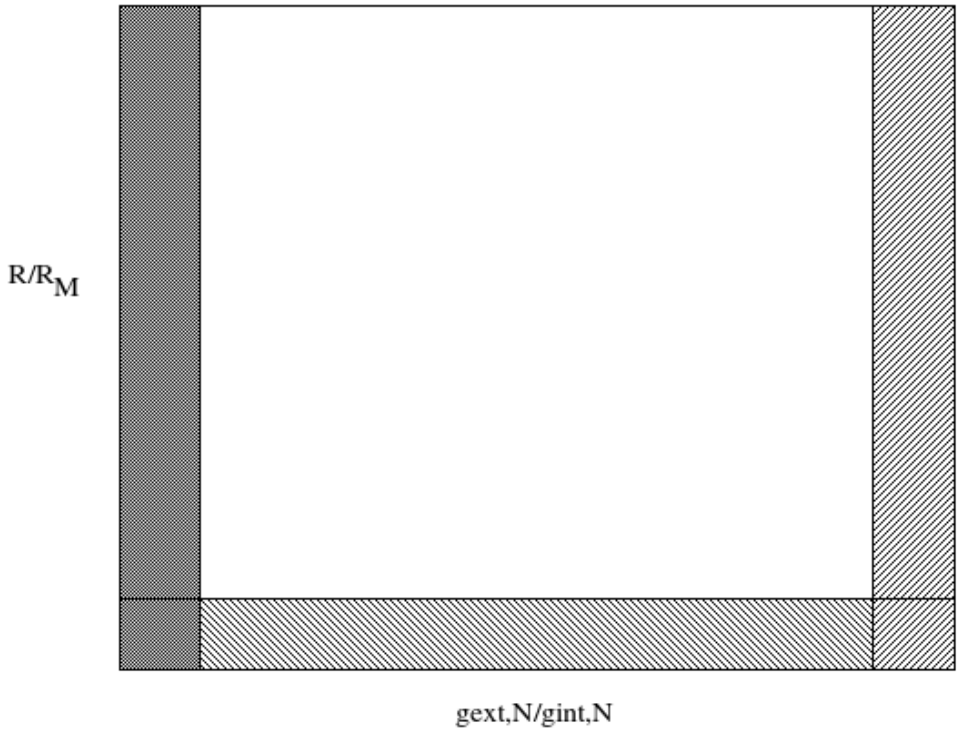

Figure 3.1: A schematic, where the x-axis represents the relative strength of the external gravitational acceleration $g_{\rm ext,N}$ compared to the initial internal gravitational acceleration $g_{\rm int,N}$ and the y-axis shows the initial distance in units of MOND radii $R_{\rm M}$. The dark grey area shows the deep-MOND regime in which the interpolation function of Eq. 3.5 is valid for calculating the gravitational acceleration. The hatched part on the bottom of the schematic is completely in the Newtonian regime and therefore the gravitational acceleration can be calculated using Eq. 3.6. Finally, the hatched area on the right side is external-field dominated and can therefore be calculated using the interpolation function from Eq. 3.8. There is no analytic solution for the upper middle (white) part of the schematic, for which numerical methods are needed.

much larger than a_0, then the system is in the Newtonian regime (for a summary, see Fig. 3.1).

3.2 Method

3.2.1 Calculating the star formation rate surface density using Newtonian Dynamics

Assuming that star formation results from the collapse of the interstellar medium via giant molecular clouds (GMCs), the star formation rate surface density ($\Sigma_{\rm SFR}$) can be expressed as

$$\Sigma_{\rm SFR} = \frac{\Sigma_{\rm gas}}{t_{\rm ff}} \varepsilon_{\rm SFE} \,, \tag{3.11}$$

where $\Sigma_{\rm gas}$ is the gas surface density, $t_{\rm ff,N}$ is the free-fall time (the time needed for gravitational collapse) assuming Newtonian Dynamics and $\varepsilon_{\rm SFE}$ is the star formation efficiency (the fraction of the cloud transformed into stars). It is well established (see e.g Zuckerman and Evans 1974; Beuther et al. 2014) that $\varepsilon_{\rm SFE}$ can be assumed to be a few percent for a GMC.

The Newtonian free-fall time $t_{\rm ff,N}$ of a spherical cloud is (see e.g. Binney and Tremaine 2008)

$$t_{\rm ff,N} = \frac{\pi}{2}\frac{R_{\rm cloud}^{3/2}}{\sqrt{2GM_{\rm cloud}}}\,, \tag{3.12}$$

with $R_{\rm cloud}$ being the radius and $M_{\rm cloud}$ the mass of the cloud. Since $\Sigma_{\rm gas}$ is known, $M_{\rm cloud}$ can be expressed as

$$M_{\rm cloud} = \Sigma_{\rm gas}\pi R_{\rm cloud}^2\,. \tag{3.13}$$

Therefore,

$$t_{\rm ff,N} = \frac{\sqrt{\pi}}{2}\sqrt{\frac{R_{\rm cloud}}{2G\Sigma_{\rm gas}}}\,. \tag{3.14}$$

Inserting this into Eq. 3.11, the Newtonian star formation surface density $\Sigma_{\rm SFR,N}$ follows:

$$\Sigma_{\rm SFR,N} = \frac{2}{\sqrt{\pi}}\Sigma_{\rm gas}^{3/2}\sqrt{\frac{2G}{R_{\rm cloud}}}\varepsilon_{\rm SFE}\,. \tag{3.15}$$

The only remaining unknown is the radius of the cloud $R_{\rm cloud}$. We determine $R_{\rm cloud}$ using a stability criterion.

Linear stability analysis of a uniformly rotating thin gas disk yields the following dispersion relation (Binney and Tremaine 2008; Escala and Larson 2008)

$$\omega^2 = \kappa^2 - 2\pi G\Sigma_{\rm gas}|k| + C_s^2k^2\,, \tag{3.16}$$

Here, κ is the epicyclic frequency, C_s the sound speed and k the wave number defined as $k = \frac{2\pi}{\lambda}$, with λ being the wavelength of the perturbation. As long as $\omega^2 > 0$, the region under study is stable against collapse. We thus set $\omega^2 = 0$ (the limit for stability/instability). By approximating $R_{\rm cloud}$ to be half of λ, we get that

$$R_{\rm cloud} = \frac{\lambda}{2} = \frac{\pi^2G\Sigma_{\rm gas}}{\kappa^2} + \sqrt{\frac{\pi^4G^2\Sigma_{\rm gas}^2}{\kappa^4} - \frac{\pi^2C_s^2}{\kappa^2}}\,. \tag{3.17}$$

Inserting $R_{\rm cloud}$ into Eq. 3.15, the Newtonian $\Sigma_{\rm SFR,N}$ becomes

$$\Sigma_{\rm SFR,N} = \varepsilon_{\rm SFE}\frac{2}{\pi^{3/2}}\kappa\Sigma_{\rm gas}\sqrt{\frac{2}{1+\sqrt{1-\frac{\kappa^2C_s^2}{\pi^2G^2\Sigma_{\rm gas}^2}}}}\,. \tag{3.18}$$

3.2.2 Calculating the star formation rate surface density using MOND

Given that MOND is a non-Newtonian classical theory of gravitation, the free-fall time must also be modified. As pointed out above, the algebraic approximation of the MOND force law needs to be

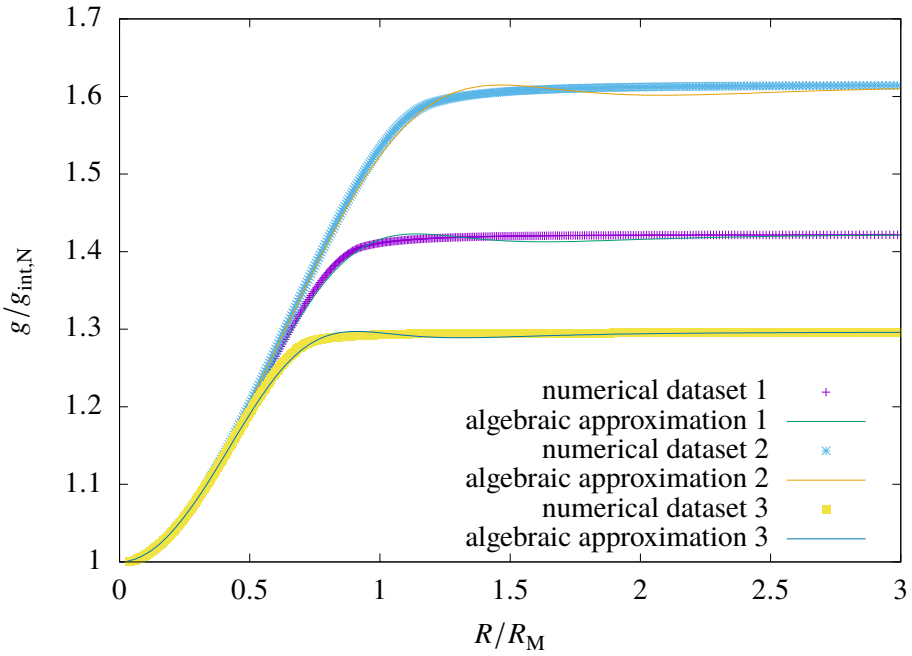

Figure 3.2: The numerical datasets from Banik and Zhao (2018b) compared to the algebraic approximation (see Eq. 3.19). The y-axis is the gravitational acceleration calculated using MOND relative to the Newtonian gravitational acceleration. The x-axis is the separation in MOND-radii. The numerical dataset and algebraic approximation 1 refer to an external field roughly as a strong as the Solar System is experiencing from the Milky Way. Dataset and approximation 2 (3) are for an external field 0.7 (1.4) times stronger than in dataset 1.

corrected in the case of a dominating external gravitational field by a factor of $(1+\frac{K}{3})$. So the first step in calculating a general Milgromian free-fall time is to derive a general algebraic description for the MOND force law. For this, we use the data from Banik and Zhao (2018b).

A general correction factor of $\left(1+\tanh\left(0.825\frac{g_{\rm ext,N}}{g_{\rm int,N}}\right)^{3.7}\frac{K}{3}\right)$ manages to reproduce the numerical results from Banik and Zhao (2018b) sufficiently well (see Fig. 3.2). It becomes $(1+\frac{K}{3})$ if the external field is much stronger than the internal field and yields a correction factor of 1 in the Newtonian regime or if the external field is much weaker than the internal field. It is therefore able to reproduce every part in the schematic of Fig 3.1. Thus, the general algebraic approximation of the MOND force law takes the form:

$$g = g_{\rm int,N}\nu\left(\frac{g_{\rm N}}{a_0}\right)\left(1+\tanh\left(0.825\frac{g_{\rm ext,N}}{g_{\rm int,N}}\right)^{3.7}\frac{K}{3}\right). \tag{3.19}$$

It is not possible to write down a closed algebraic description of the general free-fall time ($t_{\rm ff}$) in MOND valid for any state between the Newtonian regime, isolated MOND regime and quasi-Newtonian

regime. But an approximate algebraic description is possible (see Appendix B.1 for the derivation):

$$t_{\mathrm{ff}} = \frac{\pi}{2} \frac{R^{3/2}}{\sqrt{2GM\nu\left(g_{\mathrm{N}}/a_0\right)\left(1+\tanh\left(0.825\frac{g_{\mathrm{ext,N}}}{g_{\mathrm{int,N}}}\right)^{3.7}\frac{K}{3}\right)}} N\,, \tag{3.20}$$

with N being a numerical correction that becomes $\frac{2}{\sqrt{\pi}}$ in the isolated deep MOND case and 1 otherwise:

$$N = 1 + \frac{\left(1-\frac{1}{\nu\left(g_{\mathrm{N}}/a_0\right)}\right)\left(\frac{2}{\sqrt{\pi}}-1\right)}{\frac{g_{\mathrm{ext,N}}}{g_{\mathrm{int,N}}}+1}\,. \tag{3.21}$$

Note that in the Newtonian regime ($g_{\mathrm{N}} \gg a_0 \mid \nu\left(g_{\mathrm{N}}/a_0\right) \to 1 \wedge \tanh\left(0.825\frac{g_{\mathrm{ext,N}}}{g_{\mathrm{int,N}}}\right)^{3.7} K \to 0$), t_{ff} becomes equal to $t_{\mathrm{ff,N}}$ and therefore to Eq. (3.12). In the isolated deep-MOND regime ($g_{\mathrm{N,ext}} \ll g_{\mathrm{N,int}} \ll a_0 \mid \nu\left(g_{\mathrm{N}}/a_0\right) \to \sqrt{\frac{a_0}{g_{\mathrm{N}}}} \wedge \tanh\left(0.825\frac{g_{\mathrm{ext,N}}}{g_{\mathrm{int,N}}}\right)^{3.7} K \to 0$), t_{ff} simplifies to

$$t_{\mathrm{ff,idM}} = \sqrt{\frac{\pi}{2}} \frac{R_{\mathrm{cloud}}}{\sqrt[4]{GM_{\mathrm{cloud}}a_0}} = \sqrt[4]{\frac{\pi}{G\Sigma_{\mathrm{gas}}a_0}}\sqrt{\frac{R_{\mathrm{cloud}}}{2}}\,, \tag{3.22}$$

which is the same as Eq. (24) from Banik and Zhao (2018a), as expected. In the Quasi-Newtonian regime ($g_{\mathrm{N,int}} \ll g_{\mathrm{N,ext}} \ll a_0 \mid \nu\left(g_{\mathrm{N}}/a_0\right) \to \sqrt{\frac{a_0}{g_{\mathrm{N,ext}}}} \wedge \tanh\left(0.825\frac{g_{\mathrm{ext,N}}}{g_{\mathrm{int,N}}}\right)^{3.7} K \to -1/2$), t_{ff} simplifies to

$$t_{\mathrm{ff,QN}} = \sqrt{\frac{3}{5}}\frac{\pi}{2}\frac{R_{\mathrm{cloud}}^{3/2}}{\sqrt[4]{\frac{a_0}{g_{\mathrm{N,ext}}}}\sqrt{GM_{\mathrm{cloud}}}} = \frac{1}{2}\sqrt{\frac{3\pi}{5}}\sqrt{\frac{R_{\mathrm{cloud}}}{\sqrt{\frac{a_0}{g_{\mathrm{N,ext}}}}G\Sigma_{\mathrm{gas}}}} = \frac{1}{2}\sqrt{\frac{3\pi}{5}}\sqrt{\frac{R_{\mathrm{cloud}}V}{\sqrt{a_0R_{\mathrm{gal}}}G\Sigma_{\mathrm{gas}}}}\,, \tag{3.23}$$

assuming $g_{\mathrm{N,ext}} = V^2/R_{\mathrm{gal}}$ as the Newtonian external field in the last part of the equation. V is the rotational velocity (according to Newtonian models) of the disk and R_{gal} the distance to the galactic centre.

For the intermediate states, there is a divergence with the numerically determined results of only up to 3% (see Fig. 3.3).

In MOND, the stability of the thin gas disk changes to (Banik, Milgrom and Zhao, 2018)

$$\omega^2 = \kappa^2 - 2\pi G\nu\left(g_{\mathrm{N,disk}}/a_0\right)\left(1+\frac{K}{2}\right)\Sigma_{\mathrm{gas}}|k| + C_s^2k^2\,, \tag{3.24}$$

with $g_{\mathrm{N,disk}}$ being the disk's Newtonian gravitational acceleration just above the disk (see e.g. Brada and Milgrom 1995; Banik, Milgrom and Zhao 2018):

$$g_{\mathrm{N,disk}} = \sqrt{g_{\mathrm{N,r}}^2 + g_{\mathrm{N,z}}^2} = \sqrt{\left(V^2/R_{\mathrm{gal}}\right)^2 + \left(2\pi G\Sigma_{\mathrm{gas}}\right)^2}\,, \tag{3.25}$$

while $g_{\mathrm{N,r}}$ is the radial gravitational acceleration and $g_{\mathrm{N,z}}$ the vertical one orthogonal to the galactic

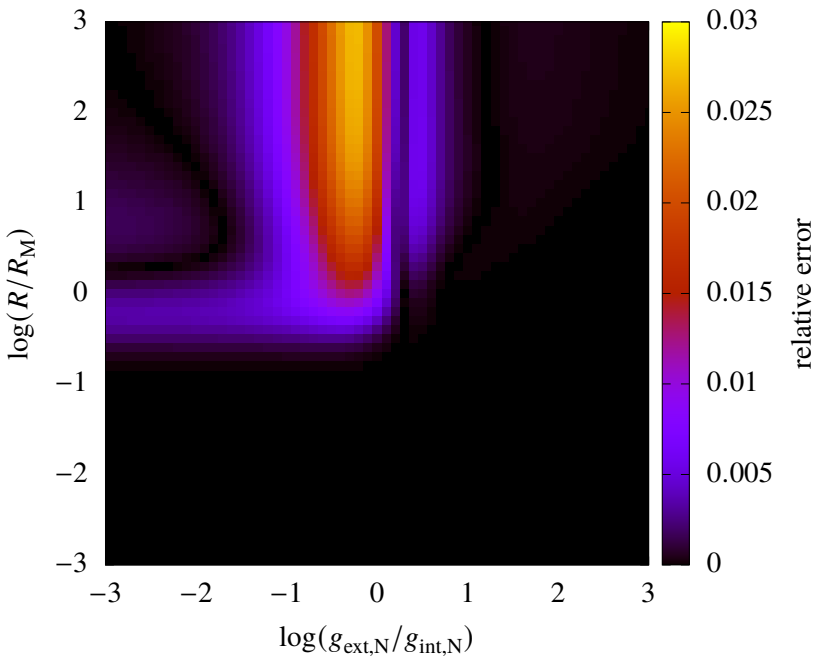

Figure 3.3: The relative error of the approximation (Eq. 3.20) for the free-fall time. The y-axis is the starting distance in MOND-radii and the x-axis is the initial ratio of the external and internal gravitational fields. As can be seen, the maximal error of the approximation is only about 3%.

disk.Note that in Eq. (3.24), K is without the $\tanh\left(0.825\frac{g_{\rm ext,N}}{g_{\rm int,N}}\right)^{3.7}$ pre-factor. As the initial perturbation to the disk is always external field dominated (see Banik, Milgrom and Zhao 2018), the pre-factor is not needed.

The equations above result in a radial extent to the collapsing region of

$$R_{\rm cloud} = \frac{\pi^2 G\nu\left(g_{\rm N,disk}/a_0\right)\left(1+\frac{K}{2}\right)\Sigma_{\rm gas}}{\kappa^2} + \sqrt{\frac{\pi^4 G^2 \nu\left(g_{\rm N,disk}/a_0\right)^2\left(1+\frac{K}{2}\right)^2\Sigma_{\rm gas}^2}{\kappa^4} - \frac{\pi^2 C_s^2}{\kappa^2}}\,. \quad (3.26)$$

In general, the MOND star formation surface density $\Sigma_{\rm SFR,M}$ therefore becomes

$$\Sigma_{\rm SFR,M} = \varepsilon_{\rm SFE}\frac{2}{N\pi^{3/2}}\kappa\Sigma_{\rm gas}\sqrt{\frac{2\nu\left(g_{\rm N}/a_0\right)\left(1+\tanh\left(0.825\frac{g_{\rm ext,N}}{g_{\rm int,N}}\right)^{3.7}\frac{K}{3}\right)}{\nu\left(g_{\rm N,disk}/a_0\right)\left(1+\frac{K}{2}\right)+\sqrt{\nu\left(g_{\rm N,disk}/a_0\right)^2\left(1+\frac{K}{2}\right)^2-\frac{\kappa^2C_s^2}{\pi^2G^2\Sigma_{\rm gas}^2}}}}\,. \quad (3.27)$$

In the Newtonian limit, this is the same as Eq. 3.18. In the isolated-deep MOND limit (which

incidentally also requires $g_{\rm N,r} \ll g_{\rm N,z}$ to avoid external field domination), one gets:

$$\Sigma_{\rm SFR,idM} = \varepsilon_{\rm SFE}\frac{2}{\pi}\frac{\sqrt[4]{2}}{\sqrt{3}}\kappa\Sigma_{\rm gas}\sqrt{\frac{2}{1+\sqrt{1-\frac{32\kappa^2C_s^2}{9\pi G\Sigma_{\rm gas}}}}}\,. \tag{3.28}$$

In the external-field dominated case (which incidentally also requires $g_{\rm N,r} \gg g_{\rm N,z}$), one obtains

$$\Sigma_{\rm SFR,QN} = \varepsilon_{\rm SFE}\frac{2\sqrt{10}}{3\pi^{3/2}}\kappa\Sigma_{\rm gas}\sqrt{\frac{2}{1+\sqrt{1-\frac{16V^2\kappa^2C_s^2}{9a_0R_{\rm gal}\pi^2G^2\Sigma_{\rm gas}^2}}}}\,. \tag{3.29}$$

3.3 Results

There are now two extreme solutions to Eq. 3.27. First, if $C_s = 0$, then Eq. (3.27) simplifies to[1]

$$\Sigma_{\rm SFR,M} = \varepsilon_{\rm SFE}\frac{2}{N\pi^{3/2}}\kappa\Sigma_{\rm gas}\sqrt{\frac{\nu\left(g_{\rm N}/a_0\right)\left(1+\tanh\left(0.825\frac{g_{\rm ext,N}}{g_{\rm int,N}}\right)^{3.7}\frac{K}{3}\right)}{\nu\left(g_{\rm N,disk}/a_0\right)\left(1+\frac{K}{2}\right)}}\,, \tag{3.30}$$

which in the different cases becomes:

$$\Sigma_{\rm SFR,N} = \varepsilon_{\rm SFE}\frac{2}{\pi^{3/2}}\kappa\Sigma_{\rm gas}\ \text{(Newtonian)}, \tag{3.31}$$

$$\Sigma_{\rm SFR,idM} = \varepsilon_{\rm SFE}\frac{2}{\pi}\frac{\sqrt[4]{2}}{\sqrt{3}}\kappa\Sigma_{\rm gas}\ \text{(isolated deep-MOND)}, \tag{3.32}$$

$$\Sigma_{\rm SFR,QN} = \varepsilon_{\rm SFE}\frac{2\sqrt{10}}{3\pi^{3/2}}\kappa\Sigma_{\rm gas}\ \text{(external-field dominated)}. \tag{3.33}$$

The other extreme case is obtained if $C_s = \frac{\pi G\nu\left(g_{\rm N,disk}/a_0\right)\left(1+\frac{K}{2}\right)\Sigma_{\rm gas}}{\kappa}$.

$$\Sigma_{\rm SFR,M} = \varepsilon_{\rm SFE}\frac{2\sqrt{2}}{N\pi^{3/2}}\kappa\Sigma_{\rm gas}\sqrt{\frac{\nu\left(g_{\rm N}/a_0\right)\left(1+\tanh\left(0.825\frac{g_{\rm ext,N}}{g_{\rm int,N}}\right)^{3.7}\frac{K}{3}\right)}{\nu\left(g_{\rm N,disk}/a_0\right)\left(1+\frac{K}{2}\right)}}\,, \tag{3.34}$$

[1] as $C_s^2 \propto T$, with T being the temperature, this would require a temperature of 0 K, making this extreme solution unphysical. Nonetheless it shows one of the extreme solutions of Eq. (3.18).

which becomes

$$\Sigma_{\rm SFR,N} = \varepsilon_{\rm SFE}\frac{2\sqrt{2}}{\pi^{3/2}}\kappa\Sigma_{\rm gas}\ \text{(Newtonian)}, \tag{3.35}$$

$$\Sigma_{\rm SFR,idM} = \varepsilon_{\rm SFE}\frac{2}{\pi}\frac{2^{3/2}}{\sqrt{3}}\kappa\Sigma_{\rm gas}\ \text{(isolated deep-MOND)}, \tag{3.36}$$

$$\Sigma_{\rm SFR,QN} = \varepsilon_{\rm SFE}\frac{2\sqrt{20}}{3\pi^{3/2}}\kappa\Sigma_{\rm gas}\ \text{(external field-dominated)}. \tag{3.37}$$

If $C_s > \frac{\pi G\nu\left(g_{\rm N,disk}/a_0\right)\left(1+\frac{K}{2}\right)\Sigma_{\rm gas}}{\kappa}$, then Eq. (3.27) becomes imaginary and therefore $\Sigma_{\rm SFR,M}$ drops to 0. This happens at high temperatures as $C_s^2 \propto T$. In the following, except if otherwise stated, we assume that star formation is possible. Therefore $\Sigma_{\rm SFR}$ must lie between these two extreme solutions to Eq. (3.27), which only differ by a factor of $\sqrt{2}$:

$$\Sigma_{\rm SFR,M}\left(C_s=0\right) = \frac{\Sigma_{\rm SFR,M}\left(C_s = \pi G\nu\left(g_{\rm N,disk}/a_0\right)\left(1+\frac{K}{2}\right)\Sigma_{\rm gas}/\kappa\right)}{\sqrt{2}}, \tag{3.38}$$

and

$$\Sigma_{\rm SFR,M}\left(C_s=0\right) \leq \Sigma_{\rm SFR,M} \leq \sqrt{2}\,\Sigma_{\rm SFR,M}\left(C_s=0\right)\ . \tag{3.39}$$

Eq. (3.27) can therefore be simplified to

$$\Sigma_{\rm SFR,M} = \varepsilon_{\rm SFE}\frac{2}{N\pi^{3/2}}\kappa\Sigma_{\rm gas}W\sqrt{\frac{\nu\left(g_{\rm N}/a_0\right)\left(1+\tanh\left(0.825\frac{g_{\rm ext,N}}{g_{\rm int,N}}\right)^{3.7}\frac{K}{3}\right)}{\nu\left(g_{\rm N,disk}/a_0\right)\left(1+\frac{K}{2}\right)}}, \tag{3.40}$$

with

$$W = \sqrt{\frac{2}{1+\sqrt{1-\frac{C_s^2\kappa^2}{\pi^2G^2\nu\left(g_{\rm N,disk}/a_0\right)\left(1+\frac{K}{2}\right)\Sigma_{\rm gas}^2}}}} = \left[1,\sqrt{2}\right]\ . \tag{3.41}$$

3.4 Discussion

As shown in Eq. (3.39), the two extremes only differ by a factor of $\sqrt{2}$ (factor W from Eq. (3.40)). Furthermore W is the only part of Eq. (3.40) depending on the sound speed C_s, which is the only part of the equation depending on the temperature. Therefore, as long as star formation is possible (Equation 3.27 has real solutions), the temperature only influences the star formation by up to a factor of $\sqrt{2}$.

As is evident from the extreme solution (see Eqs. 3.31-3.33 and Eqs. 3.35-3.37), the general dependence of $\Sigma_{\rm SFR}$ on $\Sigma_{\rm gas}$ does not change when going from the Newtonian to the MONDian regime or the external field dominated regime. Only the numerical pre-factors vary slightly. Eqs. 3.30 and 3.34 show why – the MONDian factor ν contributes to both the free-fall time and the disk stability, leading to it cancelling out. As $2g_{\rm int,N} = g_{\rm N,z}$ and $g_{\rm ext,N} = g_{\rm N,r}$, only constant numerical contributions of order unity remain from the division of the ν parameters. The general numerical deviation between

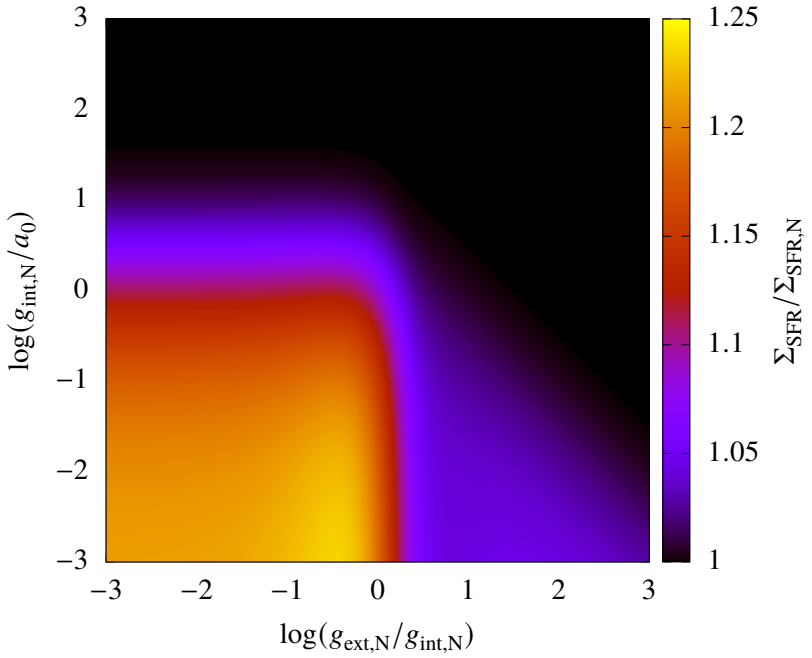

Figure 3.4: The relative deviation of $\Sigma_{\rm SFR,M}$ from $\Sigma_{\rm SFR,N}$, as calculated in Eqs. 3.27 and 3.18. The y-axis is the initial gravitational acceleration from the internal field in units of a_0, while the x-axis is the initial ratio of the external and internal gravitational fields. As can be seen, the maximal deviation arises in the deep-MOND limit and is about 25%.

the Newtonian and Milgromian formulations is up to 25%, as can be seen in Fig. 3.4.

Of further interest, Prantzos and Aubert (1995) found a radial dependence to the Kennicutt-Schmidt law (testing both for $N = 1$ and $N = 2$) of $1/R_{\rm gal}$ (Eq. 6 from Prantzos and Aubert 1995; variable names changed to be in agreement with the ones used in this chapter)

$$\Sigma_{\rm SFR} = 0.3\Sigma_{\rm gas}(R_{\rm gal}/R_\odot)^{-1}\ {\rm M}_\odot\ {\rm pc}^{-2}\ {\rm Gyr}^{-1}\,. \tag{3.42}$$

In their dynamical model, Boissier et al. (2007) described an additional dependence on the galactic rotation curve of $V(R_{\rm gal})/R_{\rm gal}$ (eq. 6 from Boissier et al. 2007; variable names changed to be in agreement with the ones used in this chapter)

$$\Sigma_{\rm SFR} = \alpha\Sigma_{\rm gas}^n \frac{V(R_{\rm gal})}{R_{\rm gal}}\,, \tag{3.43}$$

where $V(R_{\rm gal})$ is the rotation speed and α is a constant. Thus, the additional factor of Boissier et al. (2007) is equal to the one found by Prantzos and Aubert (1995) when the rotation curve becomes flat.

According to Eq. 3.39, we can write

$$\Sigma_{\rm SFR} \propto \kappa\Sigma_{\rm gas}\,, \tag{3.44}$$

and as the epicyclic frequency κ is (see e.g. A. K. Leroy et al. 2008)

$$\kappa = \sqrt{2}\frac{V(R_{\rm gal})}{R_{\rm gal}}\sqrt{1+\frac{d\log V(R_{\rm gal})}{d\log R_{\rm gal}}}\,, \tag{3.45}$$

we get that $\kappa \propto V(R_{\rm gal})/R_{\rm gal} \propto 1/R_{\rm gal}$ for a flat rotation curve. So our relation between $\Sigma_{\rm SFR}$ and $\Sigma_{\rm gas}$ is in agreement with the empirically found additional factors to the Kennicutt-Schmidt law.

3.4.1 Comparison with data

Lelli, McGaugh and Schombert (2016) published the '*Spitzer* Photometry and Accurate Rotation Curves' (SPARC) galaxy sample: 175 galaxies with surface photometry at 3.6 μm and extended HI-rotation curves. SPARC contains disk galaxies with a broad range of luminosities, surface brightness, rotation velocities and Hubble types. It therefore forms a representative sample of the nearby universe. Two main results from the SPARC data are used in the following section. Firstly, Lelli, McGaugh and Schombert (2016) found scaling relations between several characteristics of a disk galaxy, e.g a relation between the stellar and HI-mass. Secondly, analyzing the SPARC data, Lelli, McGaugh, Schombert and Pawlowski (2017) discovered the 'radial acceleration relation' (RAR) of galaxies, which gives the possibility to determine the rotation curves of galaxies from only their observed baryonic matter. The RAR relates the observed acceleration to the Newtonian acceleration of the baryons alone, so we use it to calculate rotation curves $V(R_{\rm gal})$.

Assuming the scaling relations from SPARC (Lelli, McGaugh and Schombert, 2016) and the RAR (Lelli, McGaugh, Schombert and Pawlowski, 2017), one can use the here developed star formation law to make further predictions. For simplicity, the following assumptions and approximations are made:

- The mass-to-light ratio of the stellar population is 0.5 $M_\odot/L_\odot$
- The total gas mass is 1.33 times the HI-mass ($M_{\rm HI}$)
- Both the stellar and the gas disk are single exponential disks with scale length R_d taken from the SPARC scaling relations.
- The scatter of the SPARC scaling relations is ignored (for the present).

With these simplifications we obtain (eq. 4 from Lelli, McGaugh and Schombert 2016)

$$\log_{10}(M_{\rm HI}) = 0.54\log_{10}(M_S) + 3.74\,, \tag{3.46}$$

with M_S being the stellar mass. Combining eqs. 3 and 6 from Lelli, McGaugh and Schombert (2016) yields the second scaling relation we use:

$$\log_{10}(R_d) = 0.62\log_{10}(M_{\rm HI}) - 5.40\,. \tag{3.47}$$

To calculate $V(R_{\rm gal})$, we first determine the Newtonian rotation curves of the stellar disk ($V_{\rm disk,stellar}(R_{\rm gal})$) and the gas disk ($V_{\rm disk,gas}(R_{\rm gal})$). We combine them in quadrature to get the total Newtonian rotation curve $V_{\rm N}(R_{\rm gal})$

$$V_{\rm N}(R_{\rm gal}) = \sqrt{V^2_{\rm disk,stellar}(R_{\rm gal}) + V^2_{\rm disk,gas}(R_{\rm gal})}\,. \tag{3.48}$$

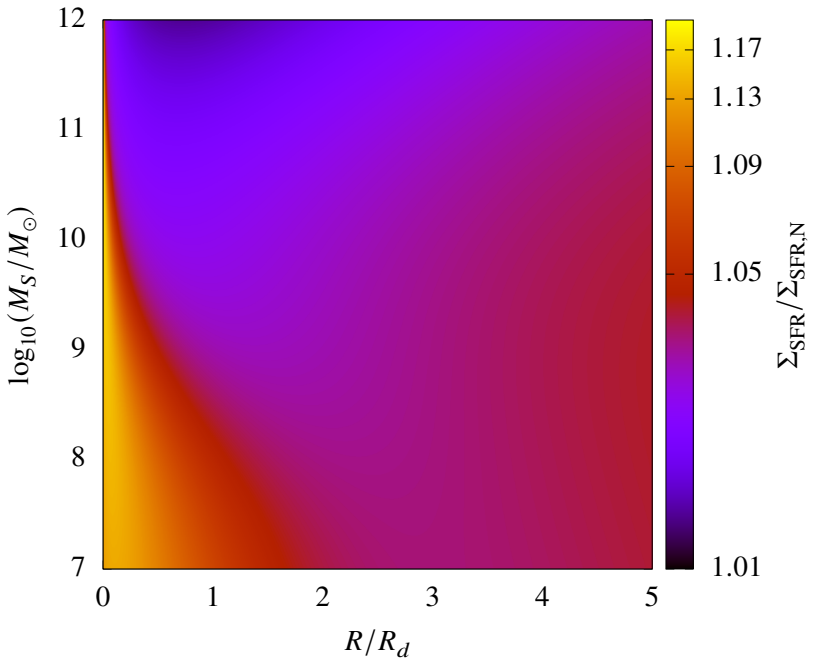

Figure 3.5: The relative deviation of $\Sigma_{SFR,M}$ from $\Sigma_{SFR,N}$, as calculated by Eqs. 3.27 and 3.18 assuming that the SPARC scaling relations (Lelli, McGaugh and Schombert, 2016) hold true and neglecting scatter. The y-axis shows the stellar mass M_S of the galaxy in Solar masses while the x-axis shows galactocentric distance in units of the scale length R_d. As can be seen, the centre of every galaxy is in the deep-MONDian regime. Further, low-mass galaxies go directly from the deep-MOND limit to the Quasi-Newtonian limit, whereas high-mass galaxies go first into the Newtonian limit. Therefore, MOND gives low-mass galaxies a bigger boost to their star formation rate than high-mass galaxies.

We then use the RAR to convert this into $V(R_{gal})$. With the above two scaling relations and $V(R_{gal})$ determined via the RAR, we can calculate Σ_{SFR} in both Newtonian and MONDian disk galaxies.[2] In particular, it is possible to show how much star formation is boosted in different regions in different galaxies by comparing MONDian to Newtonian dynamics (Fig. 3.5). See Appendix B.2 for a discussion of this including scatter.

We use Fig. 3.6 to show an example calculation of $\Sigma_{SFR,M}$ and $\Sigma_{SFR,N}$ in comparison to Σ_{gas} for two galaxies with $M_S = 10^8\ M_\odot$ and $M_S = 10^{12}\ M_\odot$.

The only remaining free parameter is the star formation efficiency ε_{SFE}, typically assumed to be a few percent (Zuckerman and Evans, 1974; Beuther et al., 2014)). Assuming a constant ε_{SFE}, it is therefore possible to radially integrate the here developed star formation law (Eq. 3.27) to get the total star formation rate (SFR). There have also been several studies exploring the relation between the stellar mass (M_S) of a galaxy and its corresponding SFR, the so-called main sequence of galaxies (e.g. Speagle et al., 2014). It is therefore possible to compare the results of the here developed theory to the observed main sequence of galaxies. A comparison with the here calculated main sequence and the one from Speagle et al. (2014) can be seen in Fig. 3.7.

Bigiel et al. (2008) compared many observations between Σ_{SFR} in comparison to Σ_{gas}. As can be

[2] The Newtonian disks are not self-gravitating, unlike the MONDian galaxies.

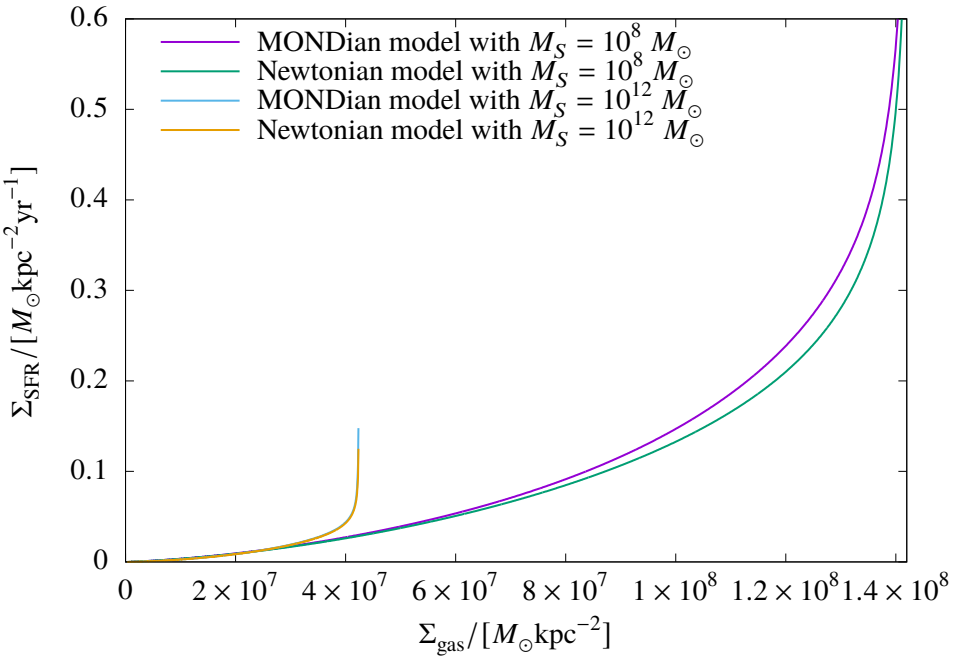

Figure 3.6: $\Sigma_{\rm SFR}$ for the Newtonian and MONDian models in comparison to $\Sigma_{\rm gas}$ for two galaxies with $M_S = 10^8\ M_\odot$ and $M_S = 10^{12}\ M_\odot$. The green curve is the Newtonian $\Sigma_{\rm SFR,N}$ for a galaxy with $M_S = 10^8\ M_\odot$, using the SPARC scaling relations (Lelli, McGaugh and Schombert, 2016) including the RAR (Lelli, McGaugh, Schombert and Pawlowski, 2017) and ignoring scatter. The purple line is the MONDian $\Sigma_{\rm SFR,M}$. The yellow line is the Newtonian model for $M_S = 10^{12}\ M_\odot$ while the blue line is the same for the MONDian model. The graph also shows that the difference between the models is much more noticeable in the low-mass galaxy. Note that although the low-mass galaxy has locally a higher $\Sigma_{\rm SFR}$ than the more massive galaxy, the total SFR is still much lower, as can be seen in Fig. 3.7.

seen in Fig. 3.8, the theory presented in this chapter follows the observations nicely.

3.5 Conclusion

It is possible to determine the MONDian Kennicutt-Schmidt law using well-established physical properties. The so found relation is

$$\Sigma_{\rm SFR,M} = \varepsilon_{\rm SFE}\frac{2}{N\pi^{3/2}}\kappa\Sigma_{\rm gas}\sqrt{\frac{2\nu\left(g_{\rm N}/a_0\right)\left(1+\tanh\left(0.825\frac{g_{\rm ext,N}}{g_{\rm int,N}}\right)^{3.7}\frac{K}{3}\right)}{\nu\left(g_{\rm N,disk}/a_0\right)\left(1+\frac{K}{2}\right)+\sqrt{\nu\left(g_{\rm N,disk}/a_0\right)^2\left(1+\frac{K}{2}\right)^2-\frac{\kappa^2C_s^2}{\pi^2G^2\Sigma_{\rm gas}^2}}}}\,. \tag{3.49}$$

Furthermore the following was established

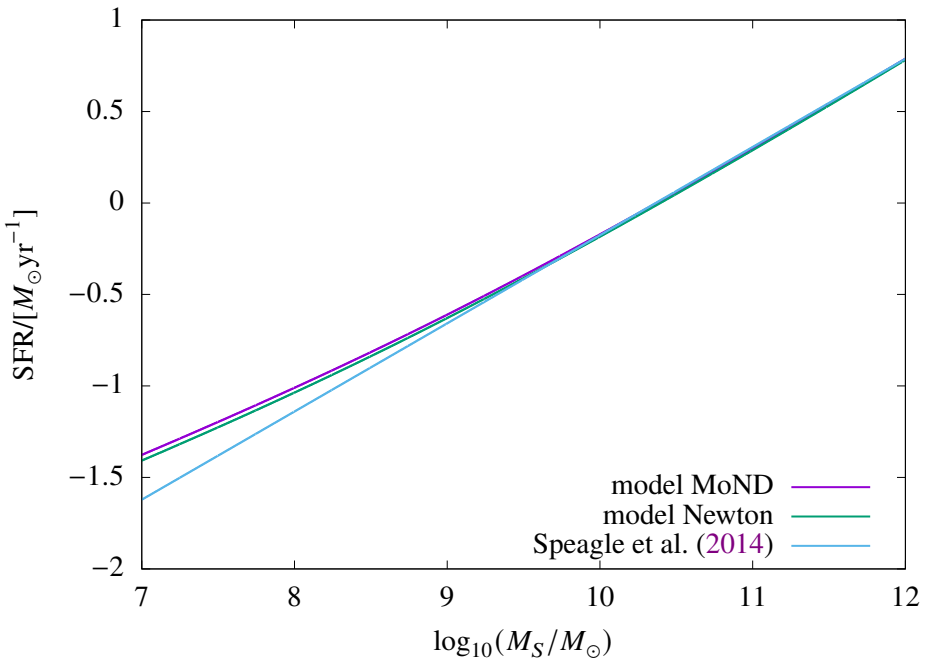

Figure 3.7: The star formation rate (SFR) in comparison to the stellar mass of a galaxy. The blue line is a fit to observations by Speagle et al. (2014) using an age of the universe of 13.77 Gyr. The green curve is a numerical integration over the whole galaxy of Eq. 3.18 using the SPARC scaling relations (Lelli, McGaugh and Schombert, 2016) including the RAR (Lelli, McGaugh, Schombert and Pawlowski, 2017) and ignoring scatter. Therefore, the green line represents the total SFR, if Newtonian dynamics is correct. The purple line is the same for MOND (Eq. 3.27). For both the Newtonian and MONDian cases, a constant star formation efficiency ($\varepsilon_{\rm SFE}$) of 1.33% has been used, as it best fits the observed main sequence. As can be seen, the derived relations are very similar and for the most part closely follow the observed one. Only for the low-mass regime do they begin to diverge. Also, the difference between the Newtonian and MONDian cases is quite small and becomes even less in the high-mass range.

- The above equation can be simplified to

$$\Sigma_{\rm SFR,M} = \varepsilon_{\rm SFE}\frac{2}{N\pi^{3/2}}\kappa\Sigma_{\rm gas}W\sqrt{\frac{\nu\left(g_{\rm N}/a_0\right)\left(1+\tanh\left(0.825\frac{g_{\rm ext,N}}{g_{\rm int,N}}\right)^{3.7}\frac{K}{3}\right)}{\nu\left(g_{\rm N,disk}/a_0\right)\left(1+\frac{K}{2}\right)}}, \tag{3.50}$$

  with $W = \left[1, \sqrt{2}\right]$.

- If star formation is possible, then the influence of the gas temperature is only up to a factor of $\sqrt{2}$.

- The general dependence on the variables $\Sigma_{\rm gas}$ and κ does not differ between the Newtonian and MONDian approach. MOND can boost the local $\Sigma_{\rm SFR}$ in a galaxy by at most 25%.

- The empirically determined correction factors to the general Kennicutt-Schmidt law found by Prantzos and Aubert (1995) and Boissier et al. (2007) are explained here through the epicyclic

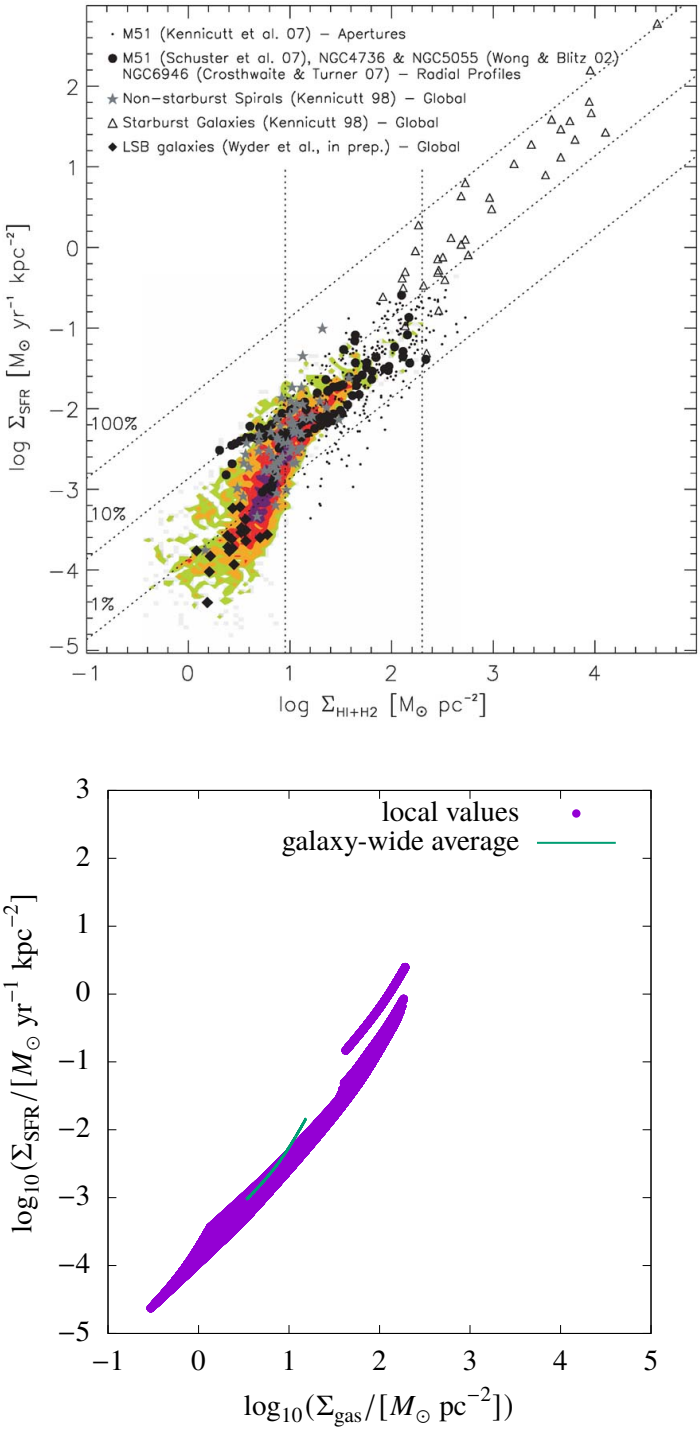

Figure 3.8: Shown is Σ_{SFR} in comparison to Σ_{gas}. The upper plot is fig. 15 from Bigiel et al. (2008) and contains observational data from Bigiel et al. (2008) (the coloured dots) and further data as mentioned in the legend. The lower plot shows the results of this chapter's theory for a variety of galaxies following the SPARC scaling relations. The dots represent local values, while the green curve is an average over the whole respective galaxy.

frequency κ.

- The observed main sequence of galaxies is consistent with the here derived star formation law $\Sigma_{\mathrm{SFR}} \propto \Sigma_{\mathrm{gas}}$ for $\varepsilon_{\mathrm{SFE}} = 1.33\%$.
- Additionally, we found an algebraic approximation for the free-fall time in MOND (Eq. 3.20).

CHAPTER 4

Applying the integrated embedded cluster mass function to the Andromeda-Galaxy

This chapter is a demonstration of the applicability of the IECMF discussed in chapter 2.

Abstract A mathematical description of the galaxy-wide mass function of freshly formed star clusters was derived in Lieberz and Kroupa (2017a), assuming an axis-symmetric exponential gas disk. It is important to test this model for disk galaxies not following these assumptions perfectly, like the Andromeda galaxy (M31). For M31 the standard model by Lieberz and Kroupa (2017a) would expect more and heavier star clusters in the centre region of M31. This is not supported by observations. The necessary changes to the model to reflect this are discussed. Application of our model to Andromeda implies that this galaxy has a suppressed star formation rate density in its inner 10 kpc region. In general the model is found to be in accordance to observational data by Johnson et al. (2016), even though M31 has a star-forming ring, which is contradictory to an exponential disk.

4.1 Introduction

The freshly-formed stellar mass of a galaxy resides in its embedded star clusters (C. J. Lada and E. A. Lada 2003b; Megeath et al. 2016a), which can synonymously be referred to as (about 1 pc extended, 1 Myr duration) space-time correlated star-formation events, i.e. essentially in molecular cloud clumps. The investigation of embedded clusters helps us to understand the build up of the stellar populations in galaxies. Embedded clusters are still fully or partially enshrouded in gas and dust, and represent the earliest stage in the life-time of a formed star cluster. They may be the forerunners to the open clusters and are therefore valuable probes for cluster formation (C. J. Lada and E. A. Lada, 2003b).

Observations indicate that the masses of the embedded star clusters in galaxies follow a particular distribution function, the embedded cluster mass function (ECMF). Lieberz and Kroupa (2017a), hereafter LK17, derive a mathematical formulation for the galaxy-wide or integrated embedded cluster mass function (IECMF). The IECMF has a Schechter-type form and results from adding all power-law ECMFs, formed at each location in a galaxy, over the the whole galaxy.

The focus of this chapter is to determine whether the “exponential model” from LK17 fits the observed data from the Andromeda galaxy (M31) (data taken from Johnson et al. 2016). M31 is a

very interesting case-study, because firstly there are many observed star clusters and secondly the gas disk of M31 is not exactly an axis-symmetric, exponential gas disk. The assumption made by LK17 was that the radial distribution of the upper mass limit of embedded clusters follows the radial distribution of the gas density, which was taken to be exponential. Here we test if this assumption leads to consistency with data in M31, which cannot be described by an exponential disk.

4.2 Method

Johnson et al. (2016) contains a catalogue of observed star clusters in the Andromeda galaxy (M31), including the region in which the star cluster was observed, and the mass and age estimates of the star clusters. The masses of these star clusters are the mass they had while still in the embedded phase. Under the assumption that the catalogue has a sufficient completeness we compare it to the "exponential model" described in LK17. The "exponential model" assumes a purely self-regulated axis-symmetric system with an exponential gas disk and a local embedded cluster mass function (LECMF) in the form of a power law. The power laws have different maximum cluster masses depending on the star formation rate density, which depends on the position within the galaxy. The maximum cluster masses result from the constraint that the locally available star-forming gas is distributed over a fully-sampled ECMF. An integration over the entire galaxy thus leads to a Schechter-like turn down of the galaxy-wide ECMF. The condition of an exponential gas disk is not completely given for M31, as M31 has a denser star-forming ring. Nonetheless it is interesting to check whether the "exponential model" is still valid for M31.

For that purpose the binned data of Johnson et al. (2016) are compared here to the integrated embedded cluster mass function (IECMF or $\xi_{\rm iecl}$), calculated with the "exponential model".

4.3 Analysis

The calculation of the IECMF requires an integration over the surface area of the galactic disk. Hereby it is important to note that the catalogue by Johnson et al. (2016) does not go over the entirety of M31. Only a third of the galaxy has been observed (Johnson et al., 2016). Therefore the angular integral used by the "exponential model" does not go from 0 to 2π but rather from from 0 to $\frac{2}{3}\pi$.

Further, the inner and outer parts of the galaxy have been cut off (Johnson et al., 2016). As a consequence the radial integral is not going idealized from 0 kpc to Infinity, but rather roughly[1] from 3 kpc to 18 kpc.

Also some parts of this were not included in the analysis by Johnson et al. (2016), only the regions 1, 2 and 3 in fig. 1 of Johnson et al. (2016). To give a rough idea how the regions were simplified and used for computational purposes (and which parts were cut-off and not used in the analysis) a direct view of the regions is given in Fig. 4.1.

The "exponential model" gives an IECMF for a galaxy only dependent on the star formation rate (SFR) and the disk scale length (r_d) of the galaxy. For M31 we assume SFR = 0.35 $M_\odot$/yr (Rahmani, Lianou and Barmby, 2016) and r_d = 5.3 kpc (Courteau et al., 2011).

[1] The parts that were cut off are not circular regions, therefore the limits for the radial integration are rough estimates based on Johnson et al. (2016)

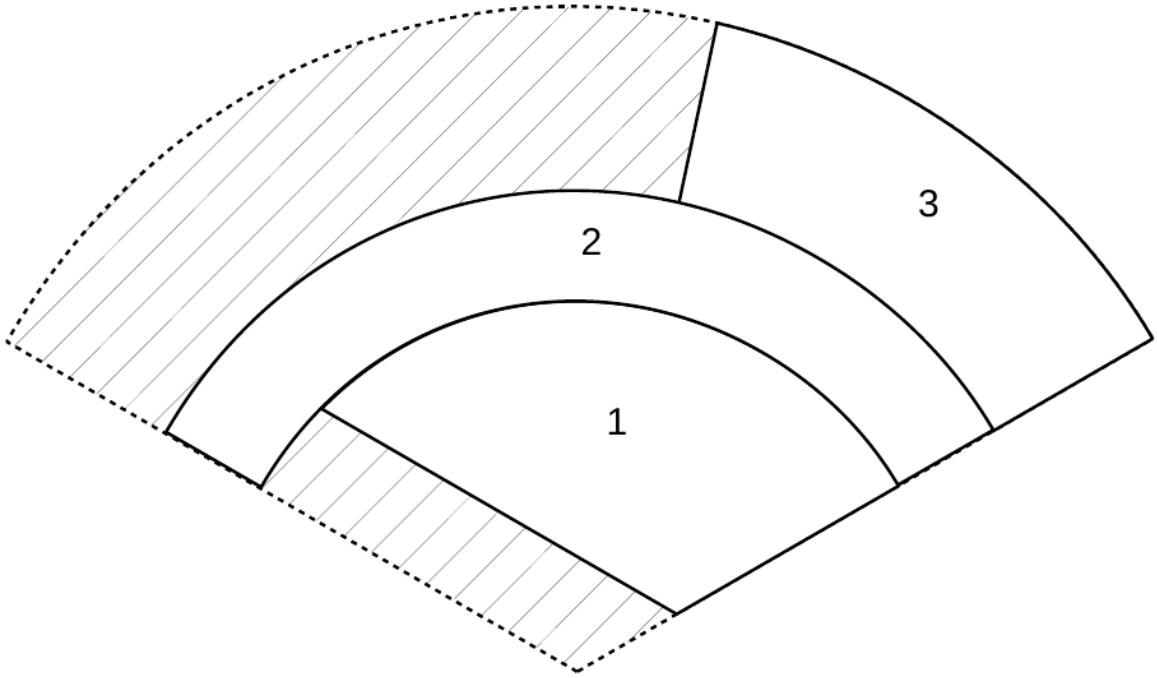

Figure 4.1: Showing the regions from a frontal view of the galaxy. Region 1 goes roughly from 3 to 10 kpc, Region 2 from 10 to 13 kpc and Region 3 from 13 to 18 kpc. The hatched parts are not included in Johnson et al. (2016).

With these we obtain (LK17):

$$\xi_{\mathrm{iecl}}(M_{\mathrm{ecl}}) = \int_{3\,\mathrm{kpc}}^{R'(M_{\mathrm{ecl}})} \int_{0}^{\phi'(r)} K(r) M_{\mathrm{ecl}}^{-\beta}\, r\, \mathrm{d}\phi \mathrm{d}r\,, \tag{4.1}$$

with

$$K(r) = \frac{(2-\beta)\,\mathrm{SFR}\,\delta t}{2\pi r_d^2 \left[\left(M_{\mathrm{U}} e^{-\frac{r}{r_d}}\right)^{2-\beta} - M_{\mathrm{ecl,min}}^{2-\beta}\right]} e^{-r/r_d}\,, \tag{4.2}$$

being the normalization constant of the LECMF, $\beta = 2.3 \pm 0.1$ being the power law index of the LECMF, $\phi'(r)$ being the observed angle in the galaxy (2π for the whole galaxy and $\frac{2}{3}\pi$ for a third of the galaxy). In this case (as shown in Fig. 4.1) the observed angle $\phi'(r)$ is dependent on the galactocentric radius. $R'(M_{\mathrm{ecl}})$ being the maximum galactocentric distance at which a cluster of mass M_{ecl} can be formed. δt is the time over which a population of embedded clusters forms, which we assume to be roughly 10 Myr, as deduced by Egusa, Sofue and Nakanishi (2004). M_{U} is the upper mass limit of the galaxy for embedded clusters and according to LK17 a SFR of 0.35 $M_\odot$/yr results in $M_{\mathrm{U}} = 2 \cdot 10^5\ M_\odot$. $M_{\mathrm{ecl,min}}$ is the lower mass limit and is assumed to be 5 $M_\odot$, corresponding to the smallest groups of embedded stars observed (Kroupa and Bouvier 2003, Kirk and Myers 2012).

We also compare our model with the data obtained from the single regions, including the “star

forming ring" (region 2 in Johnson et al. 2016). For this the lower limit of the radial integration in Eq. (4.1) changes to 10 kpc (for region 2) and 13 kpc (region 3). Also $R'(M_{\rm ecl})$ can't be larger than the galactocentric distance of the outer borders of the regions.

It is noteworthy that

$$\Sigma_{\rm SFR}(r) = \frac{\rm SFR}{2\pi r_d^2} e^{-r/r_d}\,, \tag{4.3}$$

is just the star formation surface density and

$$M_{\rm U,loc}(r) = M_{\rm U} e^{-\frac{r}{r_d}}\,, \tag{4.4}$$

is the upper limit for the mass of star clusters at a specific galactocentric radius. With that Eq. (4.2) can be rewritten as

$$K(r) = \frac{(2-\beta)\,\Sigma_{\rm SFR}(r)\,\delta t}{\left[\left(M_{\rm U,loc}(r)\right)^{2-\beta} - M_{\rm ecl,min}^{2-\beta}\right]}\,. \tag{4.5}$$

This will become important in Sec. 4.3.4.

4.3.1 Region 1

As the star cluster data from Johnson et al. (2016) contains star clusters in the age range of 10 to 300 Myr, our model, explained above, is calculated for 29 generations assuming δt = 10 Myr. In this section we only consider region 1 (see Fig. 4.1) and ignore the outer regions. The model expectations for region 1 is a later cut-off point of the mass function (due to the smaller galactocentric distance) compared to the other regions. The comparison between the binned star cluster data and the model expectations are shown in Fig. 4.2. The model overestimates the number of star clusters in the center region and also overestimates the cut-off mass. This means that the model is apparently in this form not compatible with the central region of M31. The reason being that M31 has not a exponential structure for the star formation rate density but rather a "star-forming ring" (region 2) with a higher star formation rate density than the rest of the galaxy.

This is also supported by gas surface densities measured by Johnson et al. (2016): region has a gas surface density of 4.47 $M_\odot/{\rm pc}^2$, while the gas surface densities for region 2 is 10.54 $M_\odot/{\rm pc}^2$ and for region 3 5.34 $M_\odot/{\rm pc}^2$. Both region 2 and 3 have a higher gas surface density than region 1, which is not compatible with an exponential gas disk.

4.3.2 Region 2

For region 2 we proceed similar to Section 4.3.1 to analyse the "star-forming ring". The results can be seen in Fig. 4.3. Region 3 seems to be in reasonable agreement to the model expectations.

4.3.3 Region 3

For region 3 we proceed similar to Sections 4.3.1 and 4.3.2 to analyse the outer parts of M31. Region 3 has a much smaller angular extension than the other regions, as large parts of the the outer area of the galaxy were not included in the catalogue (see Fig. 4.1 and Johnson et al. 2016). The model expectation for region 3 is a lower number of star clusters (due to the smaller area and greater galactocentric

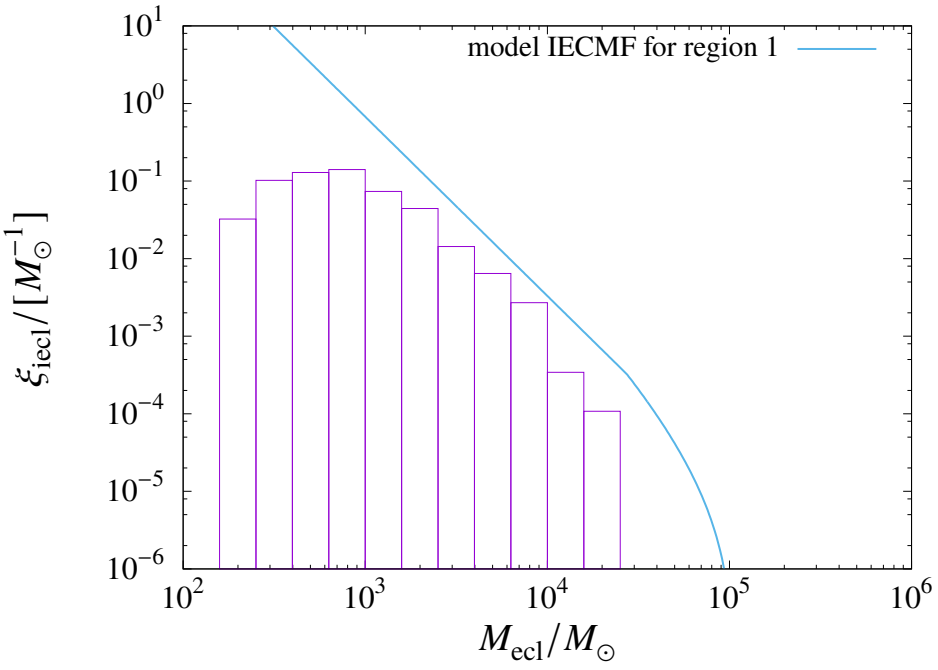

Figure 4.2: Binned young cluster mass function for region 1 (see Fig. 4.1) of M31 (data taken from Johnson et al. 2016). Also shown are the model expectations for region 1 of M31 according to the exponential model . See text for further details.

distance) and an earlier cut-off point of the mass function (due to the greater galactocentric distance) compared to the other regions. The results can be seen in Fig. 4.4. Region 3 seems to be in reasonable agreement to the model expectations.

4.3.4 All regions

Next is the comparison of the entire catalogue of star clusters younger than 300 Myr with model expectations. The results can be seen in Fig. 4.5. Given that region 1 does not fit the model expectations (see section 4.3.1) all regions combined reasonably well. Only in the high mass range does the model diverge from the observational data. This difference is there because according to model expectations region 1 is the only region with embedded star clusters in the high mass range and the exponential model does not fit the observational data for region 1 well. For lower mass ranges region 1 becomes less important and thus the model fits again with the data. All in all one can say that the exponential model is good approximation to the observed M31 in the galaxy-wide case and also in the local case for regions with a galactocentric distance larger than 10 kpc.

4.3.5 Modification to the exponential model

As region 1 does not fit to the exponential model but region 2 and 3 do, another assumption can be made: in region 2 is the peak for the star formation surface density ($\Sigma_{\rm SFR}(r)$) and it decreases exponentially both inward and outward. Also one has to ensure that the total SFR remains unchanged

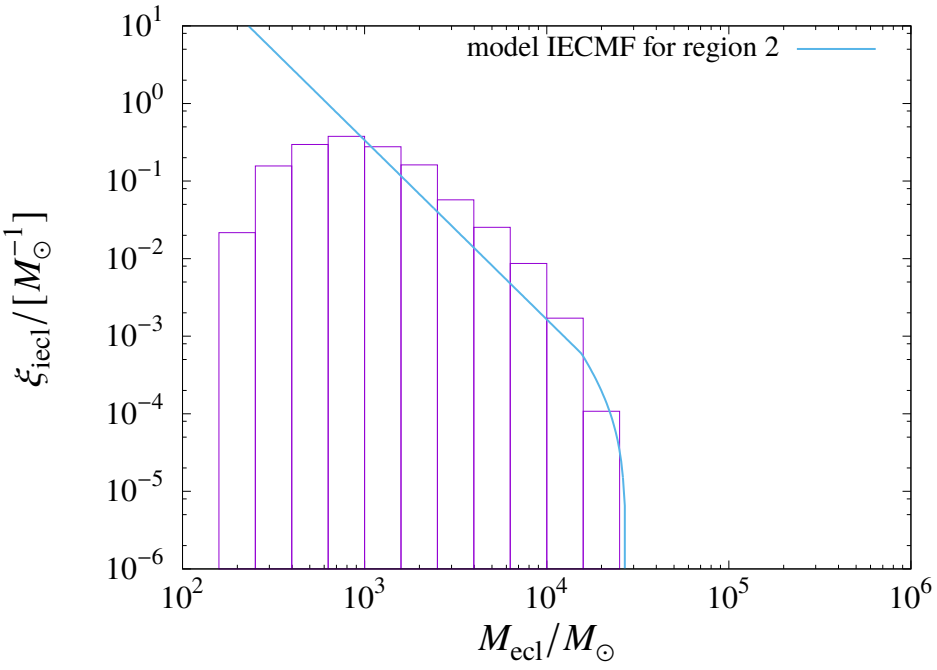

Figure 4.3: Binned young cluster mass function for the "star forming ring" (region 2) of M31 (data taken from Johnson et al. 2016). Also shown are the model expectations for region 2 of M31 according to the exponential model . See text for further details.

by this modification. Therefore Eq. (4.3) changes for region 1 to

$$\Sigma_{\rm SFR}(r) = \frac{\rm SFR}{2\pi r_d \left(2R_{12}e^{R_{12}/r_d} + r_d\right)} e^{r/r_d}\,, \tag{4.6}$$

and for region 2 and 3

$$\Sigma_{\rm SFR}(r) = \frac{\rm SFR}{2\pi r_d \left(2R_{12}e^{R_{12}/r_d} + r_d\right)} e^{(-r+2R_{12})/r_d}\,, \tag{4.7}$$

with R_{12} being the galactocentric distance of the border between region 1 and 2, so $R_{12} = 10$ kpc. The distribution of this modified $\Sigma_{\rm SFR}(r)$ can be seen in Fig. 4.6. The corresponding upper limit for the mass of star clusters (Eq. 4.4) changes for region 1 to

$$M_{\rm U,loc}(r) = M_{\rm U} e^{\frac{r-2R_{12}}{r_d}}\,, \tag{4.8}$$

while $M_{\rm U,loc}(r)$ does not change for region 2 and 3. This change ensures that $\Sigma_{\rm SFR}(r)$ and the corresponding $M_{\rm U,loc}(r)$ decrease exponentially inwards and outwards from region 2. Thus ensuring that the peak is in region 2 and that there is no break in the radial distribution of $\Sigma_{\rm SFR}(r)$ and $M_{\rm U,loc}(r)$, while also ensuring that the galaxy-wide SFR remains unchanged. The effects on region 2 and 3 are

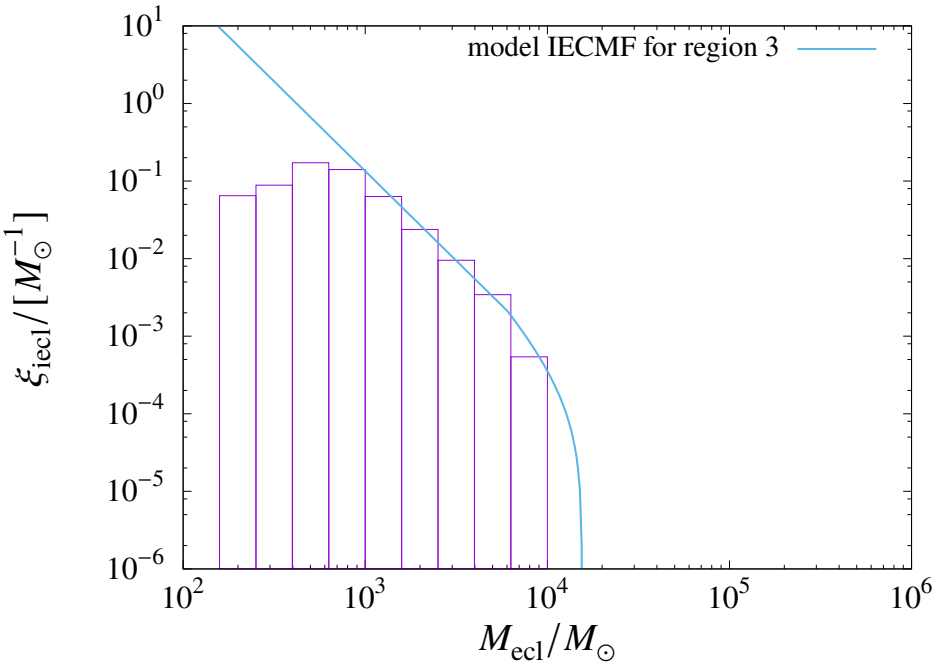

Figure 4.4: Binned young cluster mass function for the "star forming ring" (region 2) of M31 (data taken from Johnson et al. 2016). Also shown are the model expectations for region 2 of M31 according to the exponential model . See text for further details.

very small by this change. All results for all regions for this assumption can be seen in Fig. 4.7. The model seems to fit quite well. Although more tests are needed to determine if the assumption reflects reality sufficiently well, it seems to work in this context.

4.4 Conclusion

The model expectations assumed an exponential gas disc, where the number of star clusters and their maximum masses decrease outwards. As M31 does not have a strictly exponential disk (because of the "star-forming ring") it was a good test to see if the exponential model still provided a good fit or needed to be adapted.

There is no significant discrepancy between the galaxy-wide star cluster masses from Johnson et al. (2016) and the integrated embedded cluster mass function theory. Even the local cases are in reasonable agreement with the data, except the area between the galactic centre and the "star-forming ring". This means that, as far as current data are concerned, the IECMF is applicable to the Andromeda galaxy as a whole and to the single, outer parts of it. The discrepancies for the inner region can be explained as the gas disk of the Andromeda galaxy does not follow a perfect exponential form (as assumed by the exponential model). But the assumption of an exponential disk seems to work for the "star-forming ring" and the outer regions. The results of this chapter also suggest that the exponential model works for all regions if one moves the peak of the exponential disc into the "star forming ring". The modification requires a galactocentric radial dependency of the star-formation rate surface density

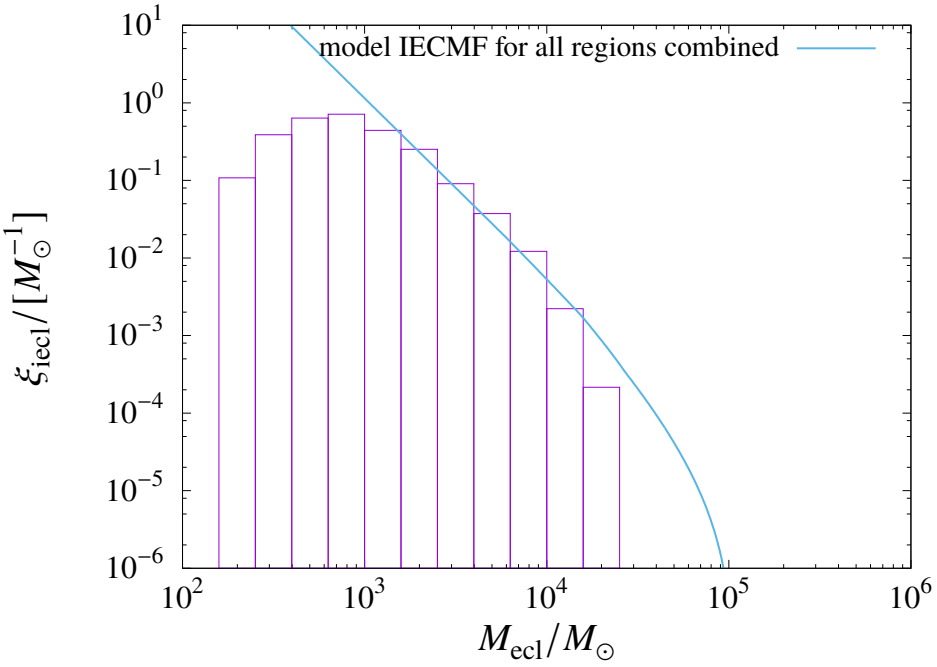

Figure 4.5: Binned young cluster mass function for the observed regions of M31 from Johnson et al. 2016. Also shown are the model expectations for them according to the exponential model . See text for further details.

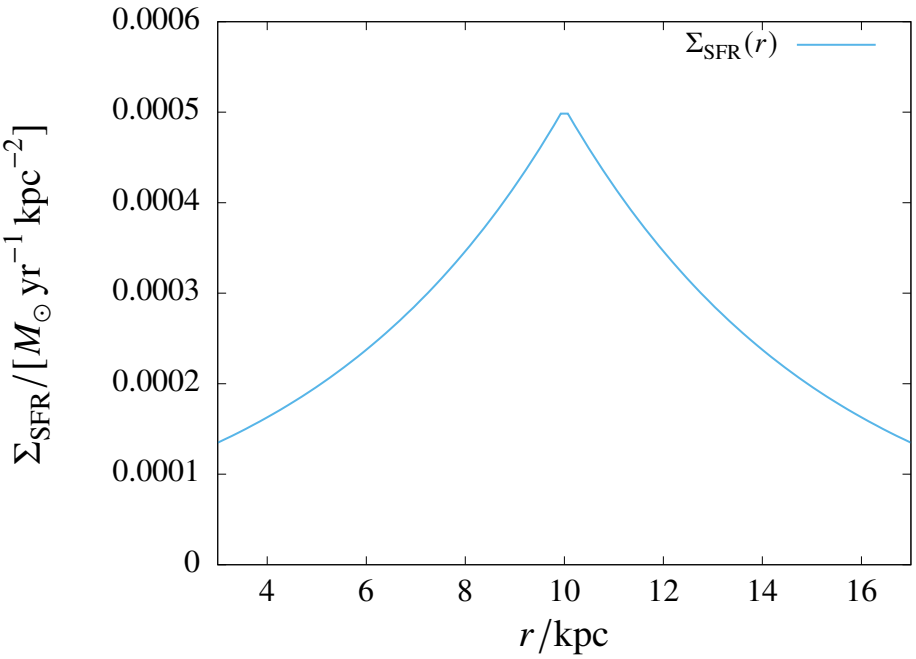

Figure 4.6: Modified radial distribution of $\Sigma_{\rm SFR}(r)$ according to the modified model discussed in Section 4.3.5. The peak of $\Sigma_{\rm SFR}(r)$ is at 10 kpc, in the "star-forming ring" (region 2).

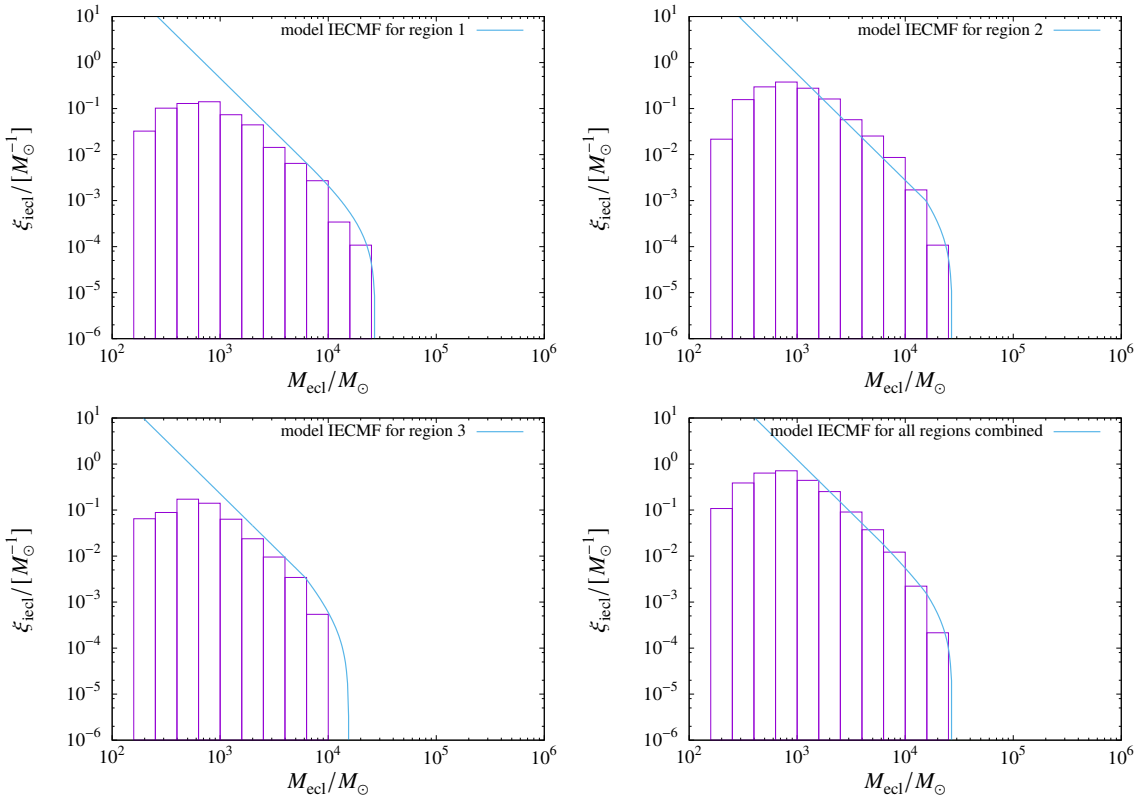

Figure 4.7: Binned young cluster mass function for the observed regions of M31 from Johnson et al. 2016. Also shown are the model expectations for a exponential model with a peak star formation surface density in the "star forming ring" (region 2). On the top left are the results for region 1, on the top right for region 2, on the bottom left for region 3 and on the bottom right for all regions. See text for further details.

as shown in Fig 4.6. We note that the Andromeda galaxy has a deficit of star formation in its inner 10 kpc region according to this model. This results in an decreasing amount of star clusters and their maximum masses both outwards and inwards from the "star forming ring", reflecting quite well the observations.

CHAPTER 5

Galactic shear: explanation for mass limits of star clusters?

This chapter is based on a planned future publication. The work on this was also the motivation for working on the research presented in chapter 3, as the need for a more theoretically developed Kennicutt-Schmidt law arose.

Abstract In the galaxy M33 it has been shown that the mass of the heaviest observed young star cluster at a given galactocentric distance decreases exponentially with increasing distance from the galactic center. It is shown that the shear effect, assuming an exponential (or stepwise exponential) galactic disk, gives an upper limit to the possible mass of gas clouds. Therefore the upper limit of the mass of star clusters is also limited by the shear effect. The shear effect can be calculated knowing the gas density and the rotation curve of a given galaxy. The radial size at which the self-gravity of a gas cloud equals the disruptive shear effect is determined assuming spherical gas clouds. This radius is assumed to be the maximal radius a gas cloud can have and is used to calculate the upper limit for the mass of the gas cloud. As the shear effect varies with galactocentric distance, so does the upper mass limit of gas clouds, resulting in a dependence on the galactocentric distance. Using a constant conversion from cloud mass to corresponding star cluster mass, one can obtain a relation between the upper mass limit of a star cluster and the galactocentric distance. Example calculations are made for the galaxies M33 and M83. For both tested galaxies the upper limit of the mass of gas clouds is found to decrease approximately exponentially with galactocentric distance, except for the central region of the galaxy. The resulting mass limit of star clusters is very well described by the shear-effect. The star cluster masses calculated with the here derived mass limit are in close agreement with observations. It is important to note that all the assumptions and calculations here were made using the classical, empirical and Newtonian Kennicutt-Schmidt law and not the theoretically discussed Kennicutt-Schmidt law from chapter 3.

5.1 Introduction

The embedded cluster mass function (ECMF), the probability density function having an embedded star cluster of a given mass in a local part of a disk galaxy, has been found to be a power-law (C. J. Lada and E. A. Lada, 2003a; Megeath et al., 2016b; Meingast et al., 2016a).

The integrated embedded cluster mass function (IECMF), the probability density function of having an embedded star cluster of a given mass in the whole disk galaxy, has the form of a Schechter-like power law (Gieles et al., 2006b). This has been explained by assuming that the ECMF is a power-law with an upper mass limit of embedded clusters depending on the environmental conditions surrounding the cluster and therefore on the position of the cluster within the galaxy. Integrating the ECMF over a galaxy would thus lead to a Schechter-like function (Lieberz and Kroupa, 2017b).

Observations of the galaxy M33 showing that the maximum star cluster mass decreases exponentially with galactocentric distance R (Pflamm-Altenburg, González-Lópezlira and Kroupa, 2013a) support this theory.

Here we study one possible explanation for this radial dependency, namely the galactic shear effect. Because the rotation curve of a galaxy is approximately constant rather than increasing linearly with R, the angular velocity of orbiting gas decreases with increasing R. The gradient of angular velocity gives rise to a disruptive force, the shear effect. If an object in the galaxy (e.g. a molecular cloud) grows so large that the shear effect becomes stronger than the self-gravity of the object, then the shear effect would destroy or reduce the size of the object. Therefore the combination of shear and self-gravity would impose a size limit, resulting, for a given density, in a mass limit, on gas clouds able to collapse under self gravity in the galaxy. As the shear effect depends on the form of the rotation curve, which varies with galactocentric distance, also the mass limit would depend on the galactocentric distance.

5.2 Method

5.2.1 Shear effect

As stated above, the competition between the self-gravity of the accumulated mass of the interstellar medium and the locale galactic shear is assumed to restrict the extension and growth of gas overdensities. This effect was quantified and calculated by Hunter, Elmegreen and Baker (1998), A. Leroy et al. (2005) and Dib et al. (2012) and named shear-effect.

In short the shear-effect can be described as follows. The surface density of the gas (Σ) should be sufficiently high for self-gravity to overcome the destructive action of locale shear. The minimal needed surface density ($\Sigma_{\rm sh}$) depends hence on the locale shear rate (described by the Oort's constant A) (see A. Leroy et al., 2005, chap. 2.2.2). Bellow this threshold the shear will disrupt the density perturbations and self gravitating clouds cannot exist. For the resulting cloud to be stable, every part of the cloud needs to have a surface density higher than $\Sigma_{\rm sh}$ and for every position within the cloud,

$$\Sigma_{\rm sh} = \frac{\alpha_A A \sigma}{\pi G}\,, \tag{5.1}$$

where A is Oort's constant and depends on the distance R to the galactic center of the token position within the cloud and on the rotational velocity V which is a function of R:

$$A = -0.5R\frac{d\Omega}{dR} = 0.5\left(\frac{V}{R} - \frac{dV}{dR}\right)\,. \tag{5.2}$$

In Eq. (5.1) α_A is a normalization constant for A assumed to be 2.5 (Hunter, Elmegreen and Baker, 1998). The velocity dispersion σ is the statistical dispersion around the mean rotational velocity of the cloud. A high gradient of rotational velocity within the cloud will increase the shear effect.

In this context we assume virial equilibrium (i.e. an unperturbed disk galaxy) and that σ is due to self gravity and thus depends only on the cloud mass and the radius of the cloud:

$$\sigma = \sqrt{\frac{G M_{\mathrm{gas}}}{r}} \,. \tag{5.3}$$

M_{gas} is the mass of the gas cloud and r its radial size. For simplicity we assume the cloud to have a spherical shape so that

$$M_{\mathrm{gas}} = \int_0^r \int_0^{2\pi} \Sigma(\Sigma_0, R', r', r_{\mathrm{d}}, \phi)\, r'\, d\phi\, dr' \,. \tag{5.4}$$

Σ is the density at a specific position within the cloud, R' is the galactocentric distance of the center of the cloud and r the radius of the cloud. Note that R' is constant within a cloud, while R varies. Σ_0 is the gas-surface-density at the center of the galaxy and r_{d} the scale length of the exponential gas-disc.

The surface density of the gas ($\Sigma(R)$) has to be higher than Σ_{sh} and depends on the assumed form of the gas disk.

This is known as the shear-criterion for gas perturbations S_g (Dib et al., 2012):

$$S_g = \frac{\Sigma_{\mathrm{sh}}}{\Sigma} = \frac{\alpha_A A \sigma}{\pi G \Sigma} \,. \tag{5.5}$$

If the condition $S_g < 1$ is fulfilled for the position R then this position within the cloud is stable against shear. The whole cloud is stable if every position within the cloud is stable against shear.

We are looking for the maximal cloud radius r for which $S_g < 1$ for every R fulfilling the following condition

$$\left\{ R \in \mathbb{R} \,|\, R' - r \leq R \leq R' + r \right\} \,, \tag{5.6}$$

in other words we are looking for the most extended cloud, which still fulfills at every position, within the cloud, the shear criterion.

This process leads to a relation between the galactocentric distance and the maximum size and mass of a gas cloud (see Eq. 5.4). So in order to quantify the shear effect at position R only two parameters are needed: the rotational velocity $V(R)$ and the gas surface density $\Sigma(R)$.

5.2.2 Evaluating the results

For simplicity we assume that a maximum of 5% of a gas clouds gets converted to embedded star clusters. Without there being further constraints we set M_{U} to be equal to the total mass converted into star clusters. Therefore we estimate M_{U} to be 5% of the mass limit for gas clouds. Even if this value is off by a few percent it will not change the results drastically, given the uncertainties. Therefore we can use the mass limit of gas clouds to determine the mass limit of star clusters ($M_{\mathrm{U}}(R')$). Having performed the steps from Section 5.2.1 it is thus possible to calculate the upper mass limit of clusters ($M_{\mathrm{U}}(R')$) for every galactocentric distance R', under the assumption that the shear-effect is the only or primary limiting factor.

In order to estimate the significance of the results we use the upper mass limit of star clusters ($M_{\mathrm{U}}(R')$) to predict the number and masses of the star clusters in the galaxy and compare them to empirical data.

We assume that locally the embedded star clusters are distributed according to the embedded star cluster mass function (ECMF or $\xi_{\rm ecl}$)), which has the form of a power law (C. J. Lada and E. A. Lada, 2003a):

$$\xi_{\rm ecl} \propto M_{\rm ecl}^{-\beta}\,, \tag{5.7}$$

where M_{ecl} is the stellar mass of the embedded star cluster, and β is the power-law parameter found to be between 1.5 and 2.5 (C. J. Lada and E. A. Lada, 2003a; Kroupa and Weidner, 2003; Weidner, Kroupa and Larsen, 2004b). In the following we will use $\beta = 2$ unless otherwise noted. Eq. (5.7) is valid between the lower mass limit $M_{\rm min}$ and the upper mass limit $M_{\rm U}(R)$ calculated above. Note that $dN_{\rm ecl} = \xi_{\rm ecl}(M_{\rm ecl})dM_{\rm ecl}$ is the number density of embedded clusters with stellar mass in the range $M_{\rm ecl}$ to $M_{\rm ecl} + dM_{\rm ecl}$.

So in order to determine whether the $M_{\rm U}(R)$ calculated with the shear-effect is in good agreement with observed reality, we use the following two tests:

Observational data give us the number and masses of star clusters more massive than a certain mass (the completeness limit) within a certain region of the galaxy. A first test is whether it is possible to predict this number of clusters. An integral of Eq. (5.7) over the observed area (taken here to be an annulus of width $R_{\rm max} - R_{\rm min}$) and observable mass range (completeness limit $M_{\rm comp}$ to $M_{\rm U}(R)$) results in the number of clusters $N_{\rm ecl}$:

$$N_{\rm ecl} = \int_{R_{\rm min}}^{R_{\rm max}} \int_{0}^{2\pi} \int_{M_{\rm comp}}^{M_{\rm U}(R)} K(R) M_{\rm ecl}^{-\beta} r \, dM_{\rm ecl} \, d\phi \, dr\,, \tag{5.8}$$

which is valid while $M_{\rm comp} < M_{\rm U}(R)$. $K(R)$ is the proportionality constant from Eq. (5.7). A description how one calculates $K(R)$ for every galactocentric distance is shown in Appendix C.1.

The second tests is whether it is possible to predict the masses of the star clusters with the previously determined $M_{\rm U}(R)$. In order to ensure that the result of the first test does not influence the second test the number of clusters will be taken from empirical data, instead of using the number determined in the first test.

The following steps are used to predict the cluster masses:

First we assume that the Kennicutt-Schmidt law is valid, which states that the star formation rate surface density $\Sigma_{\rm SFR}(R')$ is connected to the gas surface density $\Sigma(R')$ by (Schmidt, 1959)

$$\Sigma_{\rm SFR}(R') \propto \Sigma^{n}(R')\,, \tag{5.9}$$

with n being the Kennicutt-Schmidt parameter usually assumed to be 1.4 (Kennicutt, 1989). Following this one can derive the number surface density distribution function of clusters in the galaxy. For further information on the derivation see Appendix C.1. Now we randomly draw a galactocentric distance from the radial extend of the sample (between $R_{\rm min}$ and $R_{\rm max}$, which are the radial limits of the data to be compared), according to the surface density distribution function. Appendix C.2 gives information on random drawing. For each randomly selected galactocentric distance we randomly draw a cluster mass between $M_{\rm comp}$ and the corresponding $M_{\rm U}$ according to the ECMF at that galactocentric distance. See also Appendix C.2 for a more detailed description.

As the observable clusters already underwent the process of gas expulsion, meaning not being embedded clusters anymore, which alters the mass of the clusters, we simulate the clusters undergoing gas expulsion using the relation shown in figure 1 from Brinkmann et al. (2017), which related the birth mass ($M_{\rm ecl}$) to the post-gas-expulsion revirialized mass $M_{\rm cl} < M_{\rm ecl}$. Here, $M_{\rm cl}$ would be the

theoretical mass of a cluster, when it becomes observable after it underwent residual gas expulsion (e.g. the Pleiades). Brinkmann et al. (2017) relates the effect of gas expulsion to the half-mass radius $r_{\rm h}$ of the star cluster. We determine the half-mass radius of the clusters by using the Marks-Kroupa relation (Marks and Kroupa, 2012). The Marks-Kroupa-relation is a relation between the mass of a star cluster and its half-mass radius (Marks and Kroupa, 2012):

$$\frac{r_{\rm h}}{\rm pc} = 0.10^{+0.07}_{-0.04} \times \left(\frac{M_{\rm ecl}}{M_\odot}\right)^{0.13\pm0.04} , \tag{5.10}$$

thus allowing to determine the effect of gas expulsion and to calculate the mass of the cluster $M_{\rm cl}$ after gas expulsion.

The random drawing process gets repeated until N (the number of clusters from the observational data) clusters have been drawn to obtain a simulated sample of clusters. These clusters then get ranked from most to least massive.

Repeating all of the above process steps sufficiently often enough, allows to estimate the mean and median for every M_i (the mass of the i-th heaviest cluster) and the corresponding standard deviation and interquartile range. A comparison with the observational data can then be used to determine the goodness of the model.

5.3 Results

We quantify and check the influence of the shear-effect for the galaxies M33 and M83, as for these galaxies data exist on the galactocentric distances and masses of their star clusters (Pflamm-Altenburg, González-Lópezlira and Kroupa, 2013a; Sun et al., 2016) and detailed rotation curves are available (Corbelli et al., 2014; Lundgren et al., 2004). Sun et al. (2016) contains also star cluster data for M51, which we omit as there have been problems with modelling the rotation curve (Oikawa and Sofue, 2014), which may be related to this galaxy interacting with another one meaning that M51 cannot be described by an axis-symmetric virialized model.

5.3.1 Calculating the upper mass limit determined by the shear effect

For M83 we obtain the rotation curve $V(R)$ from Lundgren et al. (2004).In the case of M33 we get both the rotation curve and the radial gas surface density distribution from Corbelli et al. (2014). The baryonic disc is approximated with three overlapping exponential discs. For illustration a comparison of the resulting rotation curve with the data from Corbelli et al. (2014) can be seen in Fig. 5.1.

For simplicity we assume that both galaxies have axis-symmetric exponential gas discs. Therefore we can express the gas surface density as

$$\Sigma = \Sigma_0 e^{-R'/r_{\rm d}} , \tag{5.11}$$

resulting in Eq. (5.4) to become

$$M_{\rm gas} = \int_0^r \int_0^{2\pi} \Sigma_0 e^{-\sqrt{R'^2+r'^2+2R'r'\sin(\phi)}/r_{\rm d}} r'\, d\phi\, dr' . \tag{5.12}$$

From the literature we get $r_{\rm d}$ and the total gas mass $M_{\rm tot,gas}$ for both M33 and M83. As the total gas

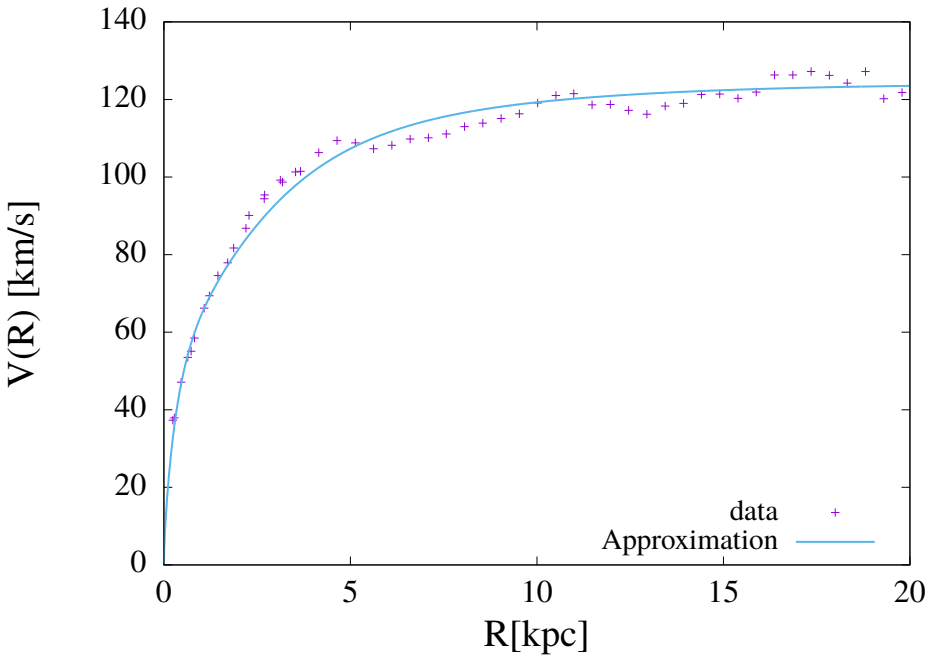

Figure 5.1: Comparison between the rotation curve by Corbelli et al. (2014) and the approximated rotation curve for M33. For details see text.

mass is the integral over the gas surface density we can use Eq. (5.11) to determine Σ_0:

$$M_{\mathrm{tot,gas}} = \int_0^{\infty} \int_0^{2\pi} \Sigma_0 e^{-R'/r_\mathrm{d}} d\phi \, R' dR' \, . \tag{5.13}$$

For M83 we use a radial scale length $r_\mathrm{d} = 2.8$ kpc and a total gas mass $M_{\mathrm{tot,gas}} = 7.8 \times 10^9 \, M_\odot$ given by Lundgren et al. (2004) resulting in $\Sigma_0 = 158 \, M_\odot \, \mathrm{pc}^{-2}$, while M33 has $r_\mathrm{d} = 2.2$ kpc and $M_{\mathrm{tot,gas}} = 1.83 \times 10^9 \, M_\odot$ (Corbelli et al., 2014) resulting in $\Sigma_0 = 60 \, M_\odot \, \mathrm{pc}^{-2}$.

With this information one can use the shear-effect to calculate the resulting upper mass limit $M_\mathrm{U}(R)$ for star clusters (see Section 5.2.1). This (including the empirical cluster masses for the galaxies) can be seen in Fig. 5.2.

5.3.2 Evaluating the results

We perform two statistical tests to determine whether these results are statistically significant.

For the first test we calculate the number of expected star clusters for both M33 and M83 according to the method described in Section 5.2.2 and compare them to the observed number of clusters, according to Pflamm-Altenburg, González-Lópezlira and Kroupa (2013a) (for M33) and Sun et al. (2016) (for M83).

In the second test we determine the masses of these clusters (as described in Section 5.2.2), rank them according to their mass and compare them to the empirical cluster masses.

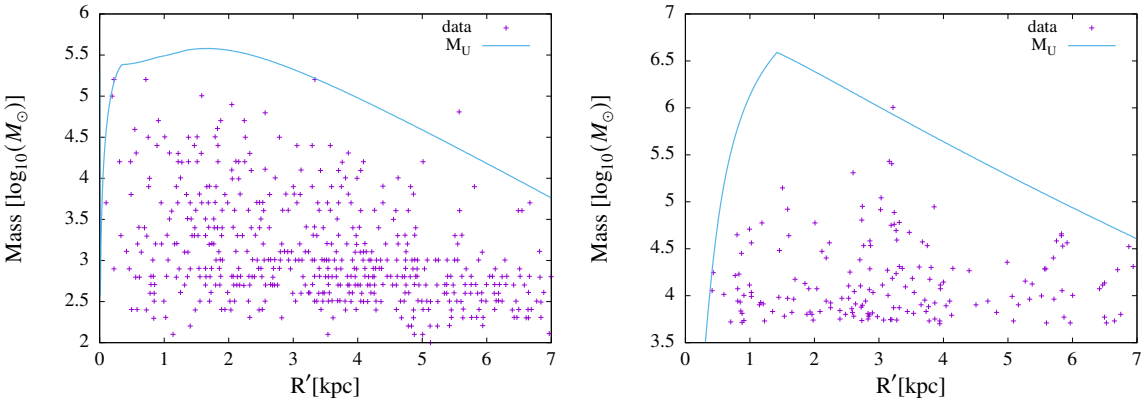

Figure 5.2: The points are the cluster data taken from Pflamm-Altenburg, González-Lópezlira and Kroupa (2013a) and Sun et al. (2016). The line is the determined upper mass limit M_U according to the shear-effect. On the left is the result for the galaxy M33 and on the right for M83.

With these tests the number of clusters and the masses of the clusters (M_i) with their corresponding interquartile ranges (IQR) can be determined. We compare these with the data from Pflamm-Altenburg, González-Lópezlira and Kroupa (2013a) (for M33) and Sun et al. (2016) (for M83) and determine the amount of clusters within the IQR. The model expectation would be that 50% of clusters fall within the IQR. As no uncertainties for the cluster masses are given we assume an uncertainty of 10%.

In order to perform the first test one needs the star formation rates (SFR) of the two galaxies and the time Δt over which all star clusters within the sample formed, as shown in Appendix C.1. Δt can be determined by subtracting the age of the youngest cluster in the sample from the age of the oldest cluster in the sample. As in our case the age of the youngest cluster is much smaller than the age of the oldest cluster, the age of the oldest cluster is already a good approximation for Δt. So we assume for M33 a star formation rate (SFR) of 0.55 $M_\odot$/yr (Sharma et al., 2011) and a Δt of $10^{7.4}$ yr, as the oldest observed clusters in the inner region of M33 have this age according to fig. 7 from Sharma et al. (2011). For M83 we assume a SFR of 3.8 $M_\odot$/yr (Eya et al. 2013, Foyle et al. 2012) and a Δt of 10^8 yr (Sun et al., 2016).

The results of the first test can be seen in Table 5.1 (for a comparison of the expected number of clusters and the observed one) and the second test in Table 5.2 (for a comparison of the ranked expected masses of the clusters). We further compare the following alternative models:

- what would be the result assuming no gas-expulsion?
- what if $\beta = 2.2$ instead of $\beta = 2$?
- what if the Kennicutt-Schmidt parameter is $n = 1$, as determined by Pflamm-Altenburg and Kroupa (2008a), instead of $n = 1.4$?
- what would change if the upper mass limit were infinite ($M_U = \infty$) and would not depend on the environment or galactocentric distance?
- what if a constant half-mass radius of $r_h = 0.3$ pc is a better approximation of r_h then using the Marks-Kroupa mass-radius relation? As according to Brinkmann et al. (2017) gas expulsion

	M33	M83
Observation	$N = 336$	$N = 179$
standard	$N = 337$	$N = 2321$
no gas-expulsion	$N = 1985$	$N = 5428$
$\beta = 2.2$	$N = 182$	$N = 1086$
$n = 1$	$N = 300$	$N = 1950$
$M_{\rm U} = \infty$	$N = 141$	$N = 1110$
Marks-Kroupa	$N = 338$	$N = 2281$

Table 5.1: Predicted number of clusters of the models. Also shown is the observed number of clusters according to Pflamm-Altenburg, González-Lópezlira and Kroupa (2013a) (for M33) and Sun et al. (2016) (for M83)

	M33	M83
	IQR	IQR
standard	0.57	0.69
no gas-expulsion	0.32	0.81
$\beta = 2.2$	0.47	0.99
$n = 1$	0.59	0.79
$M_{\rm U} = \infty$	0.24	0.34
Marks-Kroupa	0.57	0.84

Table 5.2: Statistical test comparing the masses of the i-th cluster to determine the reliability of the models. IQR gives the relative number of clusters from the empirical data which lie in the interquartile range of the model. For a perfect stochastic sample we expect that 50 % of clusters would be in the interquartile range.

depends on the half-mass radius, a constant half-mass radius would change the impact of gas-expulsion.

The results of these alternative models are also shown in Table 5.1 and 5.2

A visualization of the comparison of the ranked clusters with the empirical data for each model can be seen in Figs. 5.3 and 5.4.

We also compare whether the model results in a good description of the the radial distribution of the clusters. For that we divide each galaxy into radial bins of 1 kpc. For each bin we compare the five heaviest clusters from the model (with their corresponding interquartile ranges) with the five heaviest clusters from the observations. The results of the comparison can be seen in Fig. 5.5.

5.4 Discussion

It is possible to calculate an upper mass limit $M_{\rm U}$ for clusters using the galactic shear-effect. This upper mass limit varies with galactocentric distance (see Fig 5.2). For both galaxies it was found that $M_{\rm U}$ decreases roughly exponentially for a galactocentric distance larger than 3 (M33) or 2 (M83) kpc. Therefore the assumption that the upper mass limit can be approximated as an exponential function holds true, except for the very center of the galaxy. The fits of the exponential functions are shown in Fig. 5.6.

Table 5.1 shows the predicted number of clusters according to the various models and the observed number of clusters. In the case of M33 the standard model (a shear-induced upper mass limit, $\beta = 2$, $n = 1.4$, gas-expulsion) is the closest to observed reality, with only one more expected cluster than observed. In the case of M83 though no model was in good agreement to the number of observed clusters. Possible explanations could be that the completeness limit was set too low. The problem there is that a higher completeness limit would further reduce the number of observable clusters and would make further statistical comparisons harder.

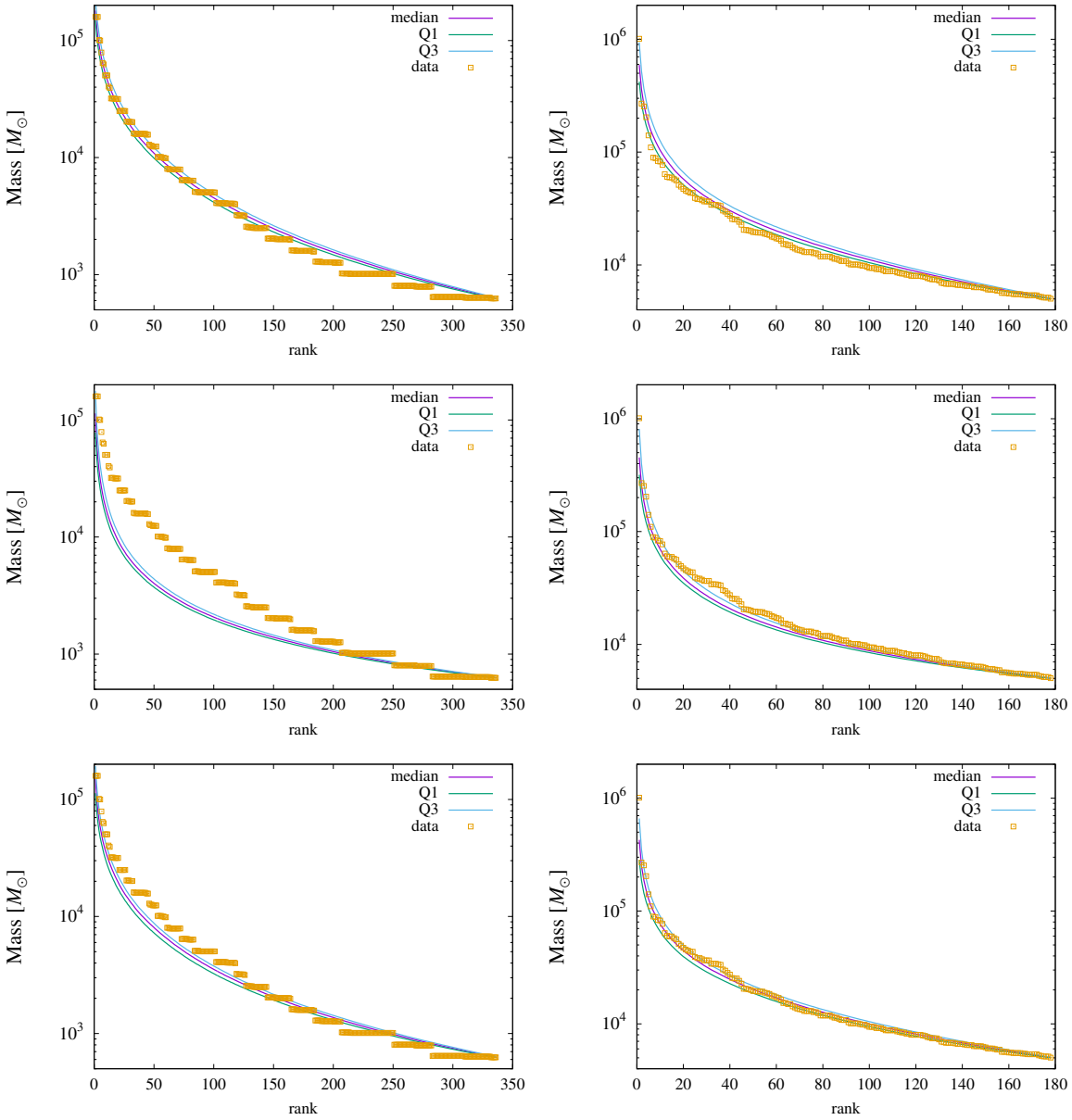

Figure 5.3: A comparison with the calculated median and interquartile range (between Q1 and Q3) and the data from Pflamm-Altenburg, González-Lópezlira and Kroupa (2013a) and Sun et al. (2016). The left panels are for the data concerning M33 and the right panels for M83. The top panels show the model including the the standard shear-effect (with gas-expulsion, $\beta = 2$ and $n = 1.4$). The central panels show the same but assuming that no gas-expulsion has happened. And the bottom panels show the distribution for $\beta = 2.2$. Plotted is the rank i of the cluster against the mass of the cluster M_i.

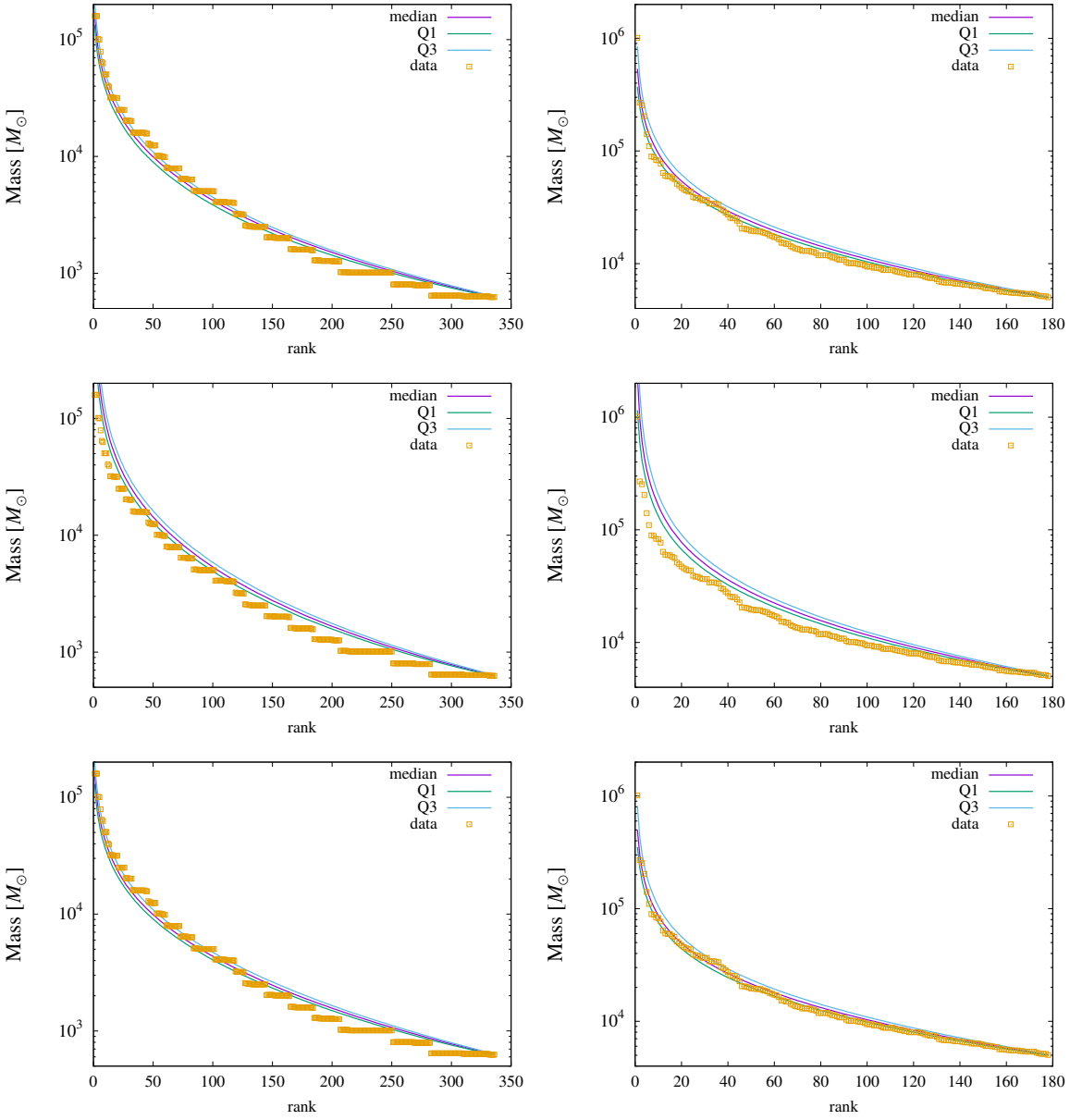

Figure 5.4: A comparison with the calculated median and interquartile range (between Q1 and Q3) and the data from Pflamm-Altenburg, González-Lópezlira and Kroupa (2013a) and Sun et al. (2016). The left panels are for the data concerning M33 and the right panels for M83. The top panels show the model including the the shear-effect assuming $n = 1$. The central panels show the stochastic distribution, assuming that the environment has no influence on cluster formation and that the upper mass limit $M_{\rm U}$ is infinite. And the bottom panels show the distribution if instead of a constant half-mass radius the Marks-Kroupa-relation is assumed. Plotted is the rank i of the cluster against the mass of the cluster M_i.

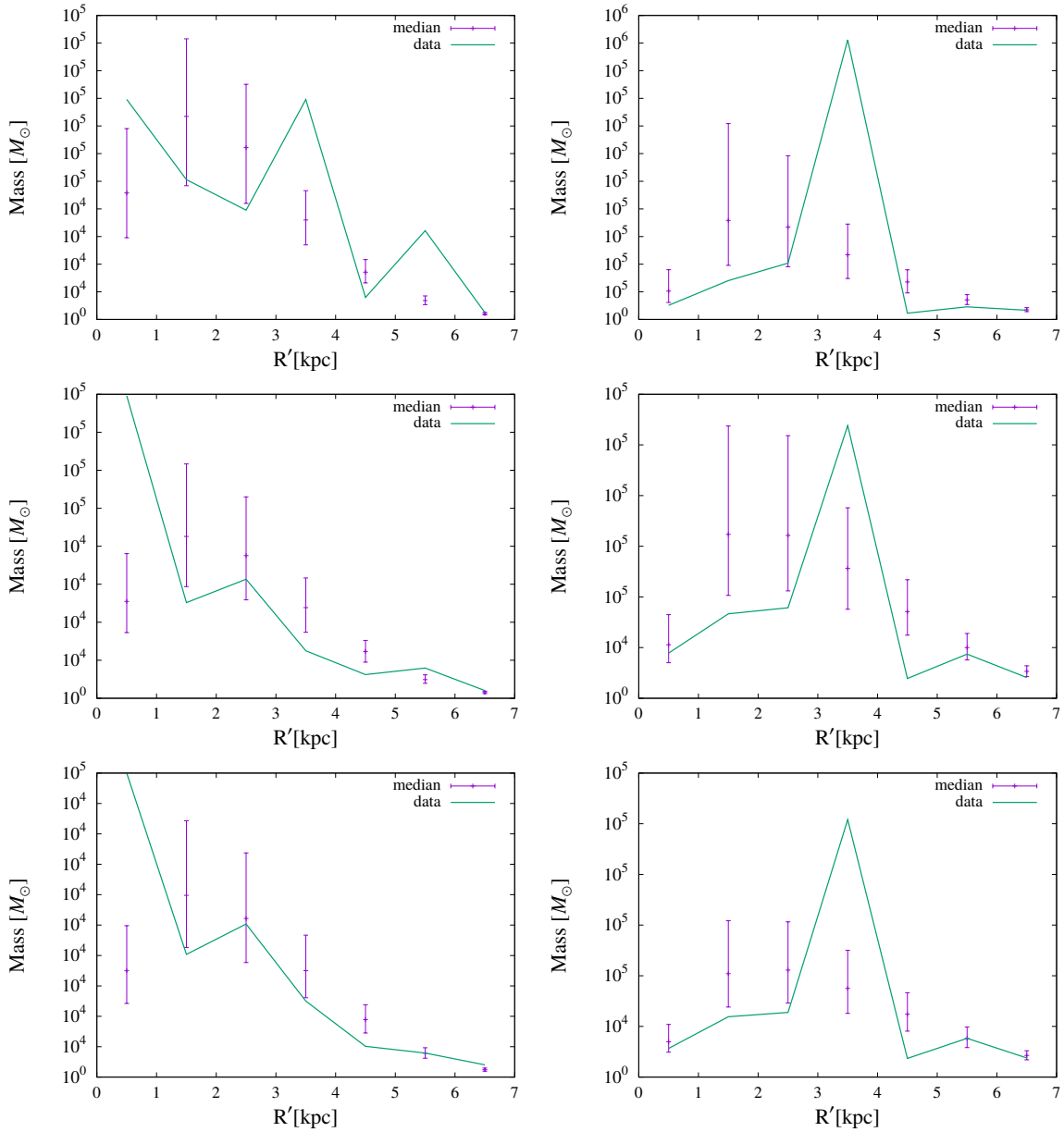

Figure 5.5: A comparison of the calculated heaviest clusters for each radial bin and the data from Pflamm-Altenburg, González-Lópezlira and Kroupa (2013a) and Sun et al. (2016). The left panels are for the data concerning M33 and the right panels for M83. From top to bottom the most massive, 2nd most massive and 3rd most massive cluster per radial bin. The green line presents the observational data, while the points show the calculated median mass and its corresponding IQR.

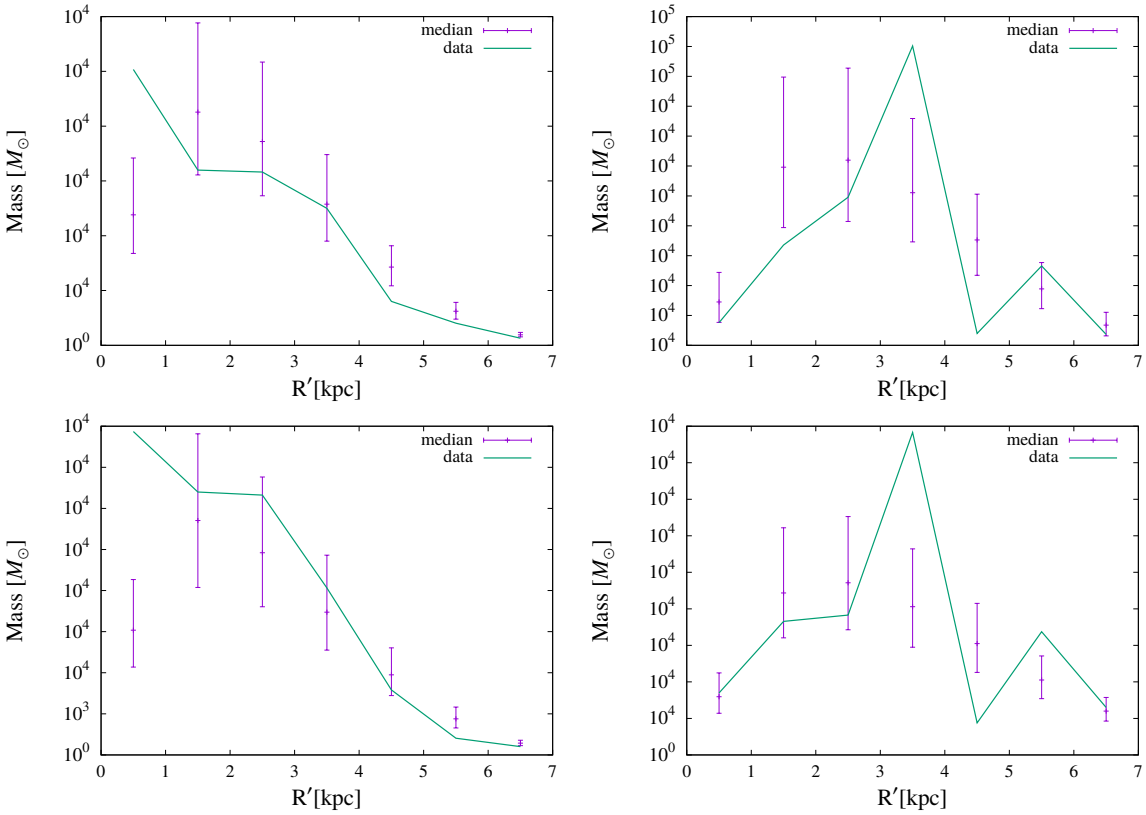

Figure 5.5: Continuation of Fig. 5.5.
A comparison of the calculated heaviest clusters for each radial bin and the data from Pflamm-Altenburg, González-Lópezlira and Kroupa (2013a) and Sun et al. (2016). The left panels are for the data concerning M33 and the right panels for M83. From top to bottom the 4th most massive and 5th most massive cluster per radial bin. The green line presents the observational data, while the points show the calculated median mass and its corresponding IQR.

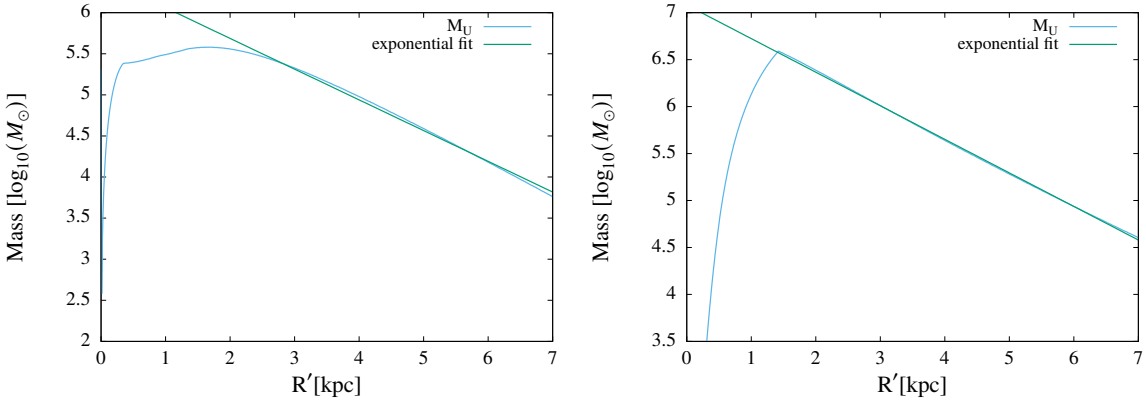

Figure 5.6: Shown here is the calculated upper mass limit (the same as in Fig 5.2) and an exponential fit to the upper mass limit. On the left is the result for the galaxy M33 and on the right M83.

Table 5.2 compares the ranked masses of the clusters and how good they are in agreement with the empirical data, by looking at the interquartile-range (IQR) of the models. For M33 we can exclude the model of no gas-expulsion happening and that the upper mass limit of embedded star clusters M_{U} is infinite. All the models which assume both a shear-induced upper mass limit and gas expulsion are in the realm of the possible with only slight changes to the amount of observed clusters within the IQR. In the case of M83 we can also exclude the model assuming M_{U} to be infinite. Every other model has more than 50% of clusters within the IQR. The model assuming $\beta = 2.2$ and the one using the Marks-Kroupa relation haven even nearly 100% of clusters within the IQR.

In conclusion the model assuming $\beta = 2$, $n = 1.4$ and a half-mass radius following the Marks-Kroupa relation is the best model fitting both galaxies satisfactory.

Looking at Figs. 5.3 and 5.4 allows to draw more conclusions. The observational data of M33 has a better mass-resolution for clusters with higher mass, allowing the conclusion that the higher mass range is more secure. This supports the standard model, the model assuming $n = 1$ and the one assuming the Marks-Kroupa relation. All these models fit better to the high-mass range than to the low mass range. The model assuming $\beta = 2.2$ on the other hand fits worse to the high-mass range and better to the low-mass clusters, making it a bit more unlikely. For M83 a comparison by eye reveals that the model model assuming $\beta = 2.2$ and the one using the Marks-Kroupa relation follow the closest the empirical data, supporting the result from Table 5.2.

Fig. 5.5 shows that overall the predicted radial distribution of the clusters fits observed reality. The heaviest cluster is for both galaxies the one with the most deviations from the model, while the 2nd-5th heaviest cluster are more in agreement with the model. This resembles the results from Pflamm-Altenburg, González-Lópezlira and Kroupa (2013a) who also found the heaviest cluster to be the one with most deviation from expected models. While both models fit the overall trend, both also have a region where the model fits the observations poorly. For M33 this is the central region within the first kpc, where the model underestimates the masses of the heaviest clusters. For M83 this region is between 3 and 4 kpc, again underestimating the masses of the clusters. Possible explanations for this effect could be that the heaviest clusters from the neighboring regions (which have slightly less massive clusters than expected) moved into the region. This could be the case for M83, which has clusters with ages up to 10^8 yr in its sample. M33 on the other hand only has clusters up to $10^{7.4}$ yr in its sample, making this explanation less likely in the case of M33. But we always assumed virial equilibrium which probably is not the case in the very center of galaxy, leading to deviating results.

As a summary we can conclude that the upper mass-limit obtained by calculating the shear-effect is in agreement with empirical data. Also gas-expulsion is necessary to obtain distributions in agreement with observations. Overall the model assuming $\beta = 2$, $n = 1.4$ and a half-mass radius following the Marks-Kroupa relation is the best model fitting both galaxies satisfactory and therefore the one which should be used for future predictions.

5.5 Conclusion

In this chapter it was shown that

- The upper mass limit for star clusters calculated using the shear-effect decreases exponentially with galactocentric distance, except close to the center of the galaxy.
- Calculating the masses of the star clusters with an embedded cluster mass function using the

upper mass limit yields more accurate results than a purely stochastic approach.

- Overall the radial distribution of clusters follows the one from observations.
- The Kennicutt-Schmidt parameter was not found to influence the results much. Both tested parameters of $n = 1.4$ and $n = 1$ resulted in similar distributions.
- A model assuming $\beta = 2$, $n = 1.4$ and a half-mass radius following the Marks-Kroupa relation is in acceptable agreement for both galaxies and is to be expected to work for other galaxies as well.
- Again using the Kennicutt-Schmidt law from chapter 3 might modify the results and would reduce the number of free parameters.

Bibliography

Abbott, T. M. C. et al. (2019), *First Cosmology Results using Type Ia Supernovae from the Dark Energy Survey: Constraints on Cosmological Parameters*, ApJ **872**, L30 L30, arXiv: 1811.02374 [astro-ph.CO] (cit. on p. 4).

Babcock, H. W. (1939), *The rotation of the Andromeda Nebula*, Lick Observatory Bulletin **498** 41 (cit. on p. 3).

Banik, I., M. Milgrom and H. Zhao (2018), *Toomre stability of disk galaxies in quasi-linear MOND*, arXiv e-prints, arXiv:1808.10545 arXiv:1808.10545, arXiv: 1808.10545 [astro-ph.GA] (cit. on pp. 35, 36).

Banik, I. and H. Zhao (2018a), *A plane of high-velocity galaxies across the Local Group*, MNRAS **473** 4033, arXiv: 1701.06559 [astro-ph.GA] (cit. on p. 35).

– (2018b), *Testing gravity with wide binary stars like α Centauri*, MNRAS **480** 2660, arXiv: 1805.12273 [astro-ph.GA] (cit. on pp. 8, 31, 34).

Baumgardt, H. and J. Makino (2003), *Dynamical evolution of star clusters in tidal fields*, MNRAS **340** 227, arXiv: astro-ph/0211471 [astro-ph] (cit. on p. 16).

Begeman, K. G., A. H. Broeils and R. H. Sanders (1991), *Extended rotation curves of spiral galaxies : dark haloes and modified dynamics.*, MNRAS **249** 523 (cit. on p. 6).

Bekenstein, J. and M. Milgrom (1984), *Does the missing mass problem signal the breakdown of Newtonian gravity?*, ApJ **286** 7 (cit. on pp. 8, 30).

Bennett, C. L. et al. (1996), *Four-Year COBE DMR Cosmic Microwave Background Observations: Maps and Basic Results*, ApJ **464** L1, arXiv: astro-ph/9601067 [astro-ph] (cit. on p. 3).

Bertone, G., D. Hooper and J. Silk (2005), *Particle dark matter: evidence, candidates and constraints*, Physics Reports **405** 279, arXiv: hep-ph/0404175 [hep-ph] (cit. on p. 3).

Beuther, H. et al. (2014), *Protostars and Planets VI*, Protostars and Planets VI (cit. on pp. 33, 41).

Bigiel, F. et al. (2008), *The Star Formation Law in Nearby Galaxies on Sub-Kpc Scales*, AJ **136** 2846, arXiv: 0810.2541 [astro-ph] (cit. on pp. 41, 44).

Binney, J. and S. Tremaine (2008), *Galactic Dynamics: Second Edition*, Princeton University Press (cit. on pp. 6, 33).

Blumenthal, G. R., S. M. Faber et al. (1984), *Formation of galaxies and large-scale structure with cold dark matter.*, Nature **311** 517 (cit. on p. 3).

Blumenthal, G. R., H. Pagels and J. R. Primack (1982), *Galaxy formation by dissipationless particles heavier than neutrinos*, Nature **299** 37 (cit. on p. 3).

Boissier, S. et al. (2007), *Radial Variation of Attenuation and Star Formation in the Largest Late-Type Disks Observed with GALEX*, ApJS **173** 524, eprint: astro-ph/0609071 (cit. on pp. 14, 30, 39, 43).

Bond, J. R., A. S. Szalay and M. S. Turner (1982), *Formation of Galaxies in a Gravitino-Dominated Universe*, Physical Review Letters **48** 1636 (cit. on p. 3).

Brada, R. and M. Milgrom (1995), *Exact solutions and approximations of MOND fields of disc galaxies*, MNRAS **276** 453 (cit. on p. 35).

Brinkmann, N. et al. (2017), *The bound fraction of young star clusters*, A&A **600**, A49 A49, arXiv: 1611.05871 (cit. on pp. 60, 61, 63).

Burkert, A. (1995), *The Structure of Dark Matter Halos in Dwarf Galaxies*, ApJ **447** L25, arXiv: astro-ph/9504041 [astro-ph] (cit. on p. 7).

Burkert, A. and G. H. Smith (2000), *A Proposed Functional Form for the Upper Mass Spectrum of Old Globular Cluster Systems*, ApJL **542** L95 (cit. on p. 16).

Chabrier, G. (2003), *Galactic Stellar and Substellar Initial Mass Function*, PASP **115** 763, arXiv: astro-ph/0304382 [astro-ph] (cit. on p. 11).

Corbelli, E. et al. (2014), *Dynamical signatures of a ΛCDM-halo and the distribution of the baryons in M 33*, A&A **572**, A23 A23, arXiv: 1409.2665 (cit. on pp. 7, 61, 62).

Courteau, S. et al. (2011), *The Luminosity Profile and Structural Parameters of the Andromeda Galaxy*, ApJ **739**, 20 20, arXiv: 1106.3564 [astro-ph.CO] (cit. on p. 48).

Curtis, H. D. (1917), *Novae in the Spiral Nebulae and the Island Universe Theory*, PASP **29** 206 (cit. on p. 2).

de Vaucouleurs, G. (1953), *On the distribution of mass and luminosity in elliptical galaxies*, MNRAS **113** 134 (cit. on p. 6).

– (1958), *Photoelectric photometry of the Andromeda Nebula in the UBV system.*, ApJ **128** 465 (cit. on p. 6).

Dib, S. et al. (2012), *The Lesser Role of Shear in Galactic Star Formation: Insight from the Galactic Ring Survey*, ApJ **758**, 125 125, arXiv: 1202.4699 (cit. on pp. 14, 58, 59).

Dopita, M. A. et al. (2010), *Supernova Remnants and the Interstellar Medium of M83: Imaging and Photometry with the Wide Field Camera 3 on the Hubble Space Telescope*, ApJ **710** 964 (cit. on p. 24).

Egusa, F., Y. Sofue and H. Nakanishi (2004), *Offsets between Hα and CO Arms of a Spiral Galaxy, NGC 4254: A New Method for Determining the Pattern Speed of Spiral Galaxies*, PASJ **56** L45, arXiv: astro-ph/0410469 [astro-ph] (cit. on pp. 17, 49).

Escala, A. and R. B. Larson (2008), *Stability of Galactic Gas Disks and the Formation of Massive Clusters*, ApJL **685** L31, arXiv: 0806.0853 (cit. on p. 33).

Eya, I. et al. (2013), *Measuring the Star Formation Rate of Nearby Galaxy – M83*, ARPN Journal of Science and Technology **VOL. 3** 1110 (cit. on p. 63).

Finnocchiaro, M. A. (1989), *The Galileo Affair*, University of California Press (cit. on p. 2).

Foyle, K. et al. (2012), *The dust and gas properties of M83*, MNRAS **421** 2917, arXiv: 1201.2178 (cit. on p. 63).

Freeman, K. C. (1970), *On the Disks of Spiral and S0 Galaxies*, ApJ **160** 811 (cit. on p. 6).

Fukui, Y. et al. (1999), *First Results of a CO Survey of the Large Magellanic Cloud with NANTEN; Giant Molecular Clouds as Formation Sites of Populous Clusters*, PASJ **51** 745 (cit. on p. 17).

Gieles, M. et al. (2006a), *The luminosity function of young star clusters: implications for the maximum mass and luminosity of clusters*, A&A **450** 129, arXiv: astro-ph/0512297 [astro-ph] (cit. on pp. 12, 16, 21).

– (2006b), *The luminosity function of young star clusters: implications for the maximum mass and luminosity of clusters*, A&A **450** 129, eprint: astro-ph/0512297 (cit. on p. 58).

Heesen, V. et al. (2014), *The Radio Continuum-Star Formation Rate Relation in WSRT SINGS Galaxies*, AJ **147**, 103 103, arXiv: 1402.1711 [astro-ph.GA] (cit. on p. 24).

Heyer, M. H. et al. (2004), *The Molecular Gas Distribution and Schmidt Law in M33*, ApJ **602** 723, eprint: astro-ph/0311226 (cit. on pp. 14, 30).
Hong, S. et al. (2013), *Constraining Stellar Feedback: Shock-ionized Gas in Nearby Starburst Galaxies*, ApJ **777**, 63 63, arXiv: 1309.0520 [astro-ph.CO] (cit. on p. 24).
Hubble, E. P. (1926), *A spiral nebula as a stellar system: Messier 33.*, ApJ **63** 236 (cit. on p. 2).
Hunter, D. A., B. G. Elmegreen and A. L. Baker (1998), *The Relationship between Gas, Stars, and Star Formation in Irregular Galaxies: A Test of Simple Models*, ApJ **493** 595, eprint: astro-ph/9712353 (cit. on pp. 14, 58).
Johnson, L. C. et al. (2016), *Panchromatic Hubble Andromeda Treasury. XVI. Star Cluster Formation Efficiency and the Clustered Fraction of Young Stars*, ApJ **827**, 33 33, arXiv: 1606.05349 [astro-ph.GA] (cit. on pp. 47–55).
Jordán, A. et al. (2007), *The ACS Virgo Cluster Survey. XII. The Luminosity Function of Globular Clusters in Early-Type Galaxies*, ApJS **171** 101, arXiv: astro-ph/0702496 [astro-ph] (cit. on p. 16).
Kennicutt Jr., R. C. (1989), *The star formation law in galactic disks*, ApJ **344** 685 (cit. on pp. 14, 30, 60, 93).
Kennicutt Jr., R. C. et al. (2007), *Star Formation in NGC 5194 (M51a). II. The Spatially Resolved Star Formation Law*, ApJ **671** 333, arXiv: 0708.0922 (cit. on pp. 14, 30).
Kent, S. M. (1986), *Dark matter in spiral galaxies. I. Galaxies with optical rotation curves.*, Astrophys. J. **91** 1301 (cit. on p. 6).
Kepler, J. (1609), *Astronomia nova*, Heidelberg : G. Voegelinus (cit. on pp. 1, 2).
– (1619), *Harmonices Mundi*, Linz : G. Tambach (cit. on p. 2).
– (1621), *Epitome Astronomiae Copernicanae*, Schönwetterus (cit. on p. 2).
Kirk, H. and P. C. Myers (2011), *Young Stellar Groups and Their Most Massive Stars*, ApJ **727**, 64 64, arXiv: 1011.1416 [astro-ph.GA] (cit. on pp. 11, 13).
– (2012), *Variations in the Mass Functions of Clustered and Isolated Young Stellar Objects*, ApJ **745**, 131 131, arXiv: 1110.4032 [astro-ph.GA] (cit. on pp. 17, 49).
Koch-Westenholz, U. (1995), *Mesopotamian Astrology*, Museum Tusculanum Press (cit. on p. 1).
Kroupa, P. (2002), "The Initial Mass Function and Its Variation (Review)", *Modes of Star Formation and the Origin of Field Populations*, ed. by E. K. Grebel and W. Brandner, vol. 285, Astronomical Society of the Pacific Conference Series 86, eprint: astro-ph/0102155 (cit. on p. 94).
Kroupa, P. and C. Weidner (2003), *Galactic-Field Initial Mass Functions of Massive Stars*, ApJ **598** 1076, eprint: astro-ph/0308356 (cit. on pp. 14, 30, 60).
Kroupa, P., C. Weidner, J. Pflamm-Altenburg et al. (2013a), *The Stellar and Sub-Stellar Initial Mass Function of Simple and Composite Populations*, Springer, Dordrecht (cit. on pp. 14, 30).
Kroupa, P. (2001), *On the variation of the initial mass function*, MNRAS **322** 231, arXiv: astro-ph/0009005 [astro-ph] (cit. on p. 11).
Kroupa, P. and J. Bouvier (2003), *The dynamical evolution of Taurus-Auriga-type aggregates*, MNRAS **346** 343, arXiv: astro-ph/0304201 [astro-ph] (cit. on pp. 17, 49).
Kroupa, P., C. Weidner, J. Pflamm-Altenburg et al. (2013b), "The Stellar and Sub-Stellar Initial Mass Function of Simple and Composite Populations", *Planets, Stars and Stellar Systems. Volume 5: Galactic Structure and Stellar Populations*, ed. by T. D. Oswalt and G. Gilmore, vol. 5 115 (cit. on pp. 11–13, 17, 18).

Krumholz, M. R. and C. F. McKee (2005), *A General Theory of Turbulence-regulated Star Formation, from Spirals to Ultraluminous Infrared Galaxies*, ApJ **630** 250, eprint: astro-ph/0505177 (cit. on p. 30).

Lada, C. J. and E. A. Lada (2003a), *Embedded Clusters in Molecular Clouds*, ARA&A **41** 57, eprint: astro-ph/0301540 (cit. on pp. 57, 60).

Lada, C. J. and E. A. Lada (2003b), *Embedded Clusters in Molecular Clouds*, ARA&A **41** 57, arXiv: astro-ph/0301540 [astro-ph] (cit. on pp. 11, 15, 16, 47, 82).

Larsen, S. S. (1999), *Young massive star clusters in nearby galaxies. II. Software tools, data reductions and cluster sizes*, A&AS **139** 393, arXiv: astro-ph/9907163 [astro-ph] (cit. on pp. 24–26).

Lawson, R. M. (2004), *Science in the ancient world : an encyclopedia*, ABC-CLIO (cit. on p. 2).

Lelli, F., S. S. McGaugh and J. M. Schombert (2016), *SPARC: Mass Models for 175 Disk Galaxies with Spitzer Photometry and Accurate Rotation Curves*, AJ **152**, 157 157, arXiv: 1606.09251 (cit. on pp. 40–43, 90, 92).

Lelli, F., S. S. McGaugh, J. M. Schombert and M. S. Pawlowski (2017), *One Law to Rule Them All: The Radial Acceleration Relation of Galaxies*, ApJ **836**, 152 152, arXiv: 1610.08981 [astro-ph.GA] (cit. on pp. 40, 42, 43, 92).

Leroy, A. et al. (2005), *The Molecular Interstellar Medium of Dwarf Galaxies on Kiloparsec Scales: A New Survey for CO in Northern, IRAS-detected Dwarf Galaxies*, ApJ **625** 763, eprint: astro-ph/0502302 (cit. on pp. 14, 30, 58).

Leroy, A. K. et al. (2008), *The Star Formation Efficiency in Nearby Galaxies: Measuring Where Gas Forms Stars Effectively*, AJ **136** 2782, arXiv: 0810.2556 (cit. on p. 40).

Leverington, D. (2003), *Babylon to Voyager and Beyond*, Cambridge University Press (cit. on p. 1).

Lieberz, P. and P. Kroupa (2017a), *On the origin of the Schechter-like mass function of young star clusters in disc galaxies*, MNRAS **465** 3775 (cit. on pp. 15, 47).

– (2017b), *On the origin of the Schechter-like mass function of young star clusters in disc galaxies*, MNRAS **465** 3775 (cit. on p. 58).

Lundgren, A. A. et al. (2004), *Molecular gas in the galaxy M 83. II. Kinematics of the molecular gas*, A&A **422** 865, eprint: astro-ph/0404026 (cit. on pp. 61, 62).

Marks, M. and P. Kroupa (2012), *Inverse dynamical population synthesis. Constraining the initial conditions of young stellar clusters by studying their binary populations*, A&A **543**, A8 A8, arXiv: 1205.1508 (cit. on p. 61).

Megeath, S. T. et al. (2016a), *The Spitzer Space Telescope Survey of the Orion A and B Molecular Clouds. II. The Spatial Distribution and Demographics of Dusty Young Stellar Objects*, AJ **151**, 5 5, arXiv: 1511.01202 [astro-ph.GA] (cit. on pp. 15, 47).

– (2016b), *The Spitzer Space Telescope Survey of the Orion A and B Molecular Clouds. II. The Spatial Distribution and Demographics of Dusty Young Stellar Objects*, AJ **151**, 5 5, arXiv: 1511.01202 (cit. on p. 57).

Meingast, S. et al. (2016a), *VISION - Vienna survey in Orion. I. VISTA Orion A Survey*, A&A **587**, A153 A153, arXiv: 1601.01687 (cit. on p. 57).

Meingast, S. et al. (2016b), *VISION - Vienna survey in Orion. I. VISTA Orion A Survey*, A&A **587**, A153 A153, arXiv: 1601.01687 [astro-ph.GA] (cit. on p. 15).

Milgrom, M. (1983a), *A modification of the Newtonian dynamics - Implications for galaxies.*, ApJ **270** 371 (cit. on p. 3).

– (1983b), *A modification of the newtonian dynamics : implications for galaxy systems.*, ApJ **270** 384 (cit. on p. 3).

– (1983c), *A modification of the Newtonian dynamics as a possible alternative to the hidden mass hypothesis*, ApJ **270** 365 (cit. on pp. 7, 8, 30, 31).
– (1983d), *A modification of the Newtonian dynamics as a possible alternative to the hidden mass hypothesis.*, ApJ **270** 365 (cit. on p. 3).
Milgrom, M. (1999), *The modified dynamics as a vacuum effect*, Physics Letters A **253** 273, arXiv: astro-ph/9805346 [astro-ph] (cit. on pp. 7, 8, 30, 31).
NASA and WMAP Science Team (2013), *Content of the Universe - Pie Chart*, URL: https://map.gsfc.nasa.gov/media/080998/index.html (visited on 08/11/2020) (cit. on p. 5).
Navarro, J. F., C. S. Frenk and S. D. M. White (1996), *The Structure of Cold Dark Matter Halos*, ApJ **462** 563, arXiv: astro-ph/9508025 [astro-ph] (cit. on p. 7).
Newton, I. (1687), *Philosophiae naturalis principia mathematica*, J. Societatis Regiae (cit. on p. 2).
Oikawa, S. and Y. Sofue (2014), *Rotation Curve Anomaly and Galactic Warp in M 51*, PASJ **66**, 77 77, arXiv: 1406.7625 (cit. on p. 61).
Oort, J. H. (1940), *Some Problems Concerning the Structure and Dynamics of the Galactic System and the Elliptical Nebulae NGC 3115 and 4494.*, ApJ **91** 273 (cit. on p. 3).
Ossendrijver, M. (2016), *Ancient Babylonian astronomers calculated Jupiter's position from the area under a time-velocity graph*, Science **351** 482 (cit. on p. 1).
Parmentier, G. and G. Gilmore (2007), *The origin of the Gaussian initial mass function of old globular cluster systems*, MNRAS **377** 352, arXiv: astro-ph/0702258 [astro-ph] (cit. on p. 16).
Peebles, P. J. E. (1982), *Large-scale background temperature and mass fluctuations due to scale-invariant primeval perturbations*, ApJ **263** L1 (cit. on p. 3).
Pflamm-Altenburg, J., R. A. González-Lópezlira and P. Kroupa (2013a), *The galactocentric radius dependent upper mass limit of young star clusters: stochastic star formation ruled out*, MNRAS **435** 2604, arXiv: 1310.0012 (cit. on pp. 58, 61–69).
Pflamm-Altenburg, J. and P. Kroupa (2008a), *Clustered star formation as a natural explanation for the Hα cut-off in disk galaxies*, Nature **455** 641, arXiv: 0905.0898 [astro-ph.GA] (cit. on pp. 14, 30, 63, 93).
Pflamm-Altenburg, J., R. A. González-Lópezlira and P. Kroupa (2013b), *The galactocentric radius dependent upper mass limit of young star clusters: stochastic star formation ruled out*, MNRAS **435** 2604, arXiv: 1310.0012 [astro-ph.GA] (cit. on pp. 25, 27).
Pflamm-Altenburg, J. and P. Kroupa (2008b), *Clustered star formation as a natural explanation for the Hα cut-off in disk galaxies*, Nature **455** 641, arXiv: 0905.0898 [astro-ph.GA] (cit. on pp. 19, 20, 26, 85).
Pingree, D. (1992), *Hellenophilia versus the history of science.*, Isis. Journal of the History of Science Society **83** 554 (cit. on p. 1).
Planck Collaboration et al. (2020), *Planck 2018 results. VI. Cosmological parameters*, A&A **641**, A6 A6, arXiv: 1807.06209 [astro-ph.CO] (cit. on pp. 4, 5).
Prantzos, N. and O. Aubert (1995), *On the chemical evolution of the galactic disk.*, A&A **302** 69 (cit. on pp. 39, 43).
Rahmani, S., S. Lianou and P. Barmby (2016), *Star formation laws in the Andromeda galaxy: gas, stars, metals and the surface density of star formation*, MNRAS **456** 4128, arXiv: 1512.06675 [astro-ph.GA] (cit. on p. 48).
Randriamanakoto, Z. et al. (2013), *Near-infrared Adaptive Optics Imaging of Infrared Luminous Galaxies: The Brightest Cluster Magnitude-Star Formation Rate Relation*, ApJL **775**, L38 L38, arXiv: 1308.6293 [astro-ph.CO] (cit. on p. 22).

Recchi, S. and P. Kroupa (2015), *The chemical evolution of galaxies with a variable integrated galactic initial mass function*, MNRAS **446** 4168, arXiv: 1411.0318 [astro-ph.GA] (cit. on p. 27).

Riess, A. G. et al. (1998), *Observational Evidence from Supernovae for an Accelerating Universe and a Cosmological Constant*, AJ **116** 1009, arXiv: astro-ph/9805201 [astro-ph] (cit. on p. 3).

Rubin, V. C., J. Ford W. K. and N. Thonnard (1980), *Rotational properties of 21 SC galaxies with a large range of luminosities and radii, from NGC 4605 (R=4kpc) to UGC 2885 (R=122kpc).*, ApJ **238** 471 (cit. on p. 3).

Rubin, V. C. and J. Ford W. Kent (1970), *Rotation of the Andromeda Nebula from a Spectroscopic Survey of Emission Regions*, ApJ **159** 379 (cit. on pp. 3, 4).

Salpeter, E. E. (1955), *The Luminosity Function and Stellar Evolution.*, ApJ **121** 161 (cit. on p. 11).

Schaye, J. and C. Dalla Vecchia (2008), *On the relation between the Schmidt and Kennicutt-Schmidt star formation laws and its implications for numerical simulations*, MNRAS **383** 1210, arXiv: 0709.0292 (cit. on pp. 14, 30).

Schmidt, M. (1959), *The Rate of Star Formation.*, ApJ **129** 243 (cit. on pp. 29, 60, 93).

Schulz, C., J. Pflamm-Altenburg and P. Kroupa (2015), *Mass distributions of star clusters for different star formation histories in a galaxy cluster environment*, A&A **582**, A93 A93, arXiv: 1507.00860 [astro-ph.GA] (cit. on pp. 17, 81, 83).

Sharma, S. et al. (2011), *The population of young stellar clusters throughout the disk of M 33*, A&A **534**, A96 A96, arXiv: 1109.4760 (cit. on p. 63).

Skibba, R. A. et al. (2011), *The Emission by Dust and Stars of Nearby Galaxies in the Herschel KINGFISH Survey*, ApJ **738**, 89 89, arXiv: 1106.4022 [astro-ph.CO] (cit. on pp. 25, 27).

Smolin, L. (2017), *MOND as a regime of quantum gravity*, PhysRevD **96**, 083523 083523, arXiv: 1704.00780 [gr-qc] (cit. on pp. 7, 30).

Smoot, G. F. et al. (1992), *Structure in the COBE Differential Microwave Radiometer First-Year Maps*, ApJ **396** L1 (cit. on p. 3).

Sofue, Y. (2013), "Mass Distribution and Rotation Curve in the Galaxy", *Planets, Stars and Stellar Systems. Volume 5: Galactic Structure and Stellar Populations*, ed. by T. D. Oswalt and G. Gilmore, vol. 5 985 (cit. on pp. 5, 6).

Speagle, J. S. et al. (2014), *A Highly Consistent Framework for the Evolution of the Star-Forming "Main Sequence" from z ~ 0-6*, ApJS **214**, 15 15, arXiv: 1405.2041 (cit. on pp. 41, 43, 90, 92).

Sun, W. et al. (2016), *The Star Cluster Mass-Galactocentric Radius Relation: Implications for Cluster Formation*, ApJ **816**, 9 9, arXiv: 1511.04490 (cit. on pp. 61–68).

Tamburro, D. et al. (2008), *Geometrically Derived Timescales for Star Formation in Spiral Galaxies*, AJ **136** 2872, arXiv: 0810.2391 [astro-ph] (cit. on p. 17).

Toomre, A. (1964), *On the gravitational stability of a disk of stars*, ApJ **139** 1217 (cit. on p. 30).

Trimble, V. (1995), *The 1920 Shapley-Curtis Discussion: Background, Issues, and Aftermath*, PASP **107** 1133 (cit. on p. 2).

Tully, R. B. and J. R. Fisher (1977), *Reprint of 1977A&A....54..661T. A new method of determining distance to galaxies.*, A&A **500** 105 (cit. on p. 9).

Weidner, C. and P. Kroupa (2005), *The Variation of Integrated Star Initial Mass Functions among Galaxies*, ApJ **625** 754, arXiv: astro-ph/0502525 [astro-ph] (cit. on p. 12).

Weidner, C., P. Kroupa and I. A. D. Bonnell (2010), *The relation between the most-massive star and its parental star cluster mass*, MNRAS **401** 275, arXiv: 0909.1555 [astro-ph.SR] (cit. on pp. 11, 13).

Weidner, C., P. Kroupa and S. S. Larsen (2004a), *Implications for the formation of star clusters from extragalactic star formation rates*, MNRAS **350** 1503, arXiv: astro-ph/0402631 [astro-ph] (cit. on pp. 12, 16, 17, 20–22, 79, 80, 82, 84).
– (2004b), *Implications for the formation of star clusters from extragalactic star formation rates*, MNRAS **350** 1503, eprint: astro-ph/0402631 (cit. on p. 60).
Weidner, C., P. Kroupa, J. Pflamm-Altenburg et al. (2013), *The galaxy-wide initial mass function of dwarf late-type to massive early-type galaxies*, MNRAS **436** 3309, arXiv: 1309.6634 [astro-ph.CO] (cit. on p. 27).
Westman, R. S. (2011), *The Copernican Question*, University of California Press (cit. on p. 1).
Wu, X. and P. Kroupa (2015), *Galactic rotation curves, the baryon-to-dark-halo-mass relation and space-time scale invariance*, MNRAS **446** 330, arXiv: 1410.2256 [astro-ph.GA] (cit. on pp. 7, 30).
Yamaguchi, R. et al. (2001), "A CO Survey of the LMC with NANTEN: III. Formation of Stellar Clusters and Evolution of Molecular Clouds", vol. 53, 6 985 (cit. on p. 17).
Zuckerman, B. and N. J. Evans II (1974), *Models of massive molecular clouds*, ApJL **192** L149 (cit. on pp. 33, 41).
Zwicky, F. (1933), *Die Rotverschiebung von extragalaktischen Nebeln*, Helvetica Physica Acta **6** 110 (cit. on p. 3).
– (1937), *On the Masses of Nebulae and of Clusters of Nebulae*, ApJ **86** 217 (cit. on p. 3).

APPENDIX A

Appendix of Chapter 2

A.1 The LECMF with a Non-Infinitesimal Surface Area

In this section we discuss what differences there are to Sec. 2.2 if one uses an observable non-infinitesimal surface area ΔA instead of $\mathrm{d}A$. First Eq. (2.1) becomes

$$\xi_{\mathrm{lecl}}(M_{\mathrm{ecl}};r)\,\mathrm{d}M_{\mathrm{ecl}}\,\Delta A = \mathrm{d}N_{\mathrm{ecl}}\,. \tag{A.1}$$

For a given region ΔA, $\Sigma_{\mathrm{SFR}}(r)$ becomes the local star formation rate LSFR:

$$\mathrm{LSFR}(r) = \frac{\Delta\mathrm{SFR}}{\Delta A}\,, \tag{A.2}$$

with ΔSFR being the star formation rate in the galactic region ΔA.

The total mass formed in stars is then obtained by multiplying $\mathrm{LSFR}(r)$ with δt (Weidner, Kroupa and Larsen, 2004a):

$$\mathrm{LSFR}(r)\,\delta t = \int_{M_{\mathrm{ecl,min}}}^{M_{\mathrm{U,loc}}(r)} M'_{\mathrm{ecl}}\xi_{\mathrm{lecl}}(M'_{\mathrm{ecl}};r)\mathrm{d}M'_{\mathrm{ecl}}\,. \tag{A.3}$$

For $\beta \neq 2$ we obtain

$$K(r) = \frac{\mathrm{LSFR}(r)\,\delta t(2-\beta)}{M_{\mathrm{U,loc}}^{2-\beta}(r) - M_{\mathrm{ecl,min}}^{2-\beta}}\,. \tag{A.4}$$

For the special case of $\beta = 2$,

$$K(r) = \frac{\mathrm{LSFR}(r)\,\delta t}{\ln\left(M_{\mathrm{U,loc}}(r)/M_{\mathrm{ecl,min}}\right)}\,. \tag{A.5}$$

Using the LECMF it is now possible to calculate the mass of the most massive observable cluster in the region ΔA ($M_{\mathrm{ecl,max,loc}}(r)$). To determine $M_{\mathrm{ecl,max,loc}}(r)$ we use two conditions: first there is only one most massive cluster. Second the mass of the most massive cluster is $M_{\mathrm{ecl,max,loc}}(r)$.

To implement the first condition we choose a mass interval between the upper mass limit $M_{\mathrm{U,loc}}(r)$ and $M_{\mathrm{ecl,t,loc}}(r)$, with $M_{\mathrm{ecl,t,loc}}(r)$ chosen in such a way that there is only one cluster between these

limits:

$$1 \approx \int_{M_{\rm ecl,t}(r)}^{M_{\rm U,loc}(r)} \xi_{\rm lecl}(M'_{\rm ecl};r)\mathrm{d}M'_{\rm ecl}\,\Delta A\,, \tag{A.6}$$

and the second condition implies that the mass between these limits is $M_{\rm ecl,max,loc}(r)$:

$$M_{\rm ecl,max,loc}(r) \approx \int_{M_{\rm ecl,t}(r)}^{M_{\rm U,loc}(r)} M'_{\rm ecl}\xi_{\rm lecl}(M'_{\rm ecl};r)\mathrm{d}M'_{\rm ecl}\,\Delta A\,. \tag{A.7}$$

The reason for the equation being approximated is that $\xi_{\rm lecl}(M'_{\rm ecl};r)$ depends on r. One would have to perform an integration over ΔA to get the exact value (see also Sect. 2.3). But for small ΔA the above equation is a good approximation.

Using Eqs. (A.6) and (A.7) $M_{\rm ecl,max,loc}(r)$ becomes for $\beta \neq 2$:

$$M_{\rm ecl,t}(r) \approx \left(M^{1-\beta}_{\rm U,loc}(r) - \frac{1-\beta}{K(r)\Delta A}\right)^{\frac{1}{1-\beta}}\,, \tag{A.8}$$

$$M_{\rm ecl,max,loc}(r) \approx \frac{K(r)}{2-\beta}\left[M^{2-\beta}_{\rm U,loc}(r) - M^{2-\beta}_{\rm ecl,t}(r)\right]\Delta A\,. \tag{A.9}$$

And for $\beta = 2$:

$$M_{\rm ecl,max,loc}(r) \approx K(r)\left[\ln\left(1+\frac{M_{\rm U,loc}(r)}{K(r)\Delta A}\right)\right]\Delta A\,. \tag{A.10}$$

This is a simple method to determine $M_{\rm ecl,max,loc}(r)$ without having to perform an integration over the area, as long as ΔA is small enough.

A.2 Comparison to Weidner-Normalization

Weidner, Kroupa and Larsen (2004a) defined Eq. (2.4) slightly differently:

$$\Sigma_{\rm SFR}(r)\,\delta t = \int_{M_{\rm ecl,min}}^{M_{\rm ecl,max,loc}(r)} M'_{\rm ecl}\xi_{\rm lecl}(M'_{\rm ecl};r)\mathrm{d}M'_{\rm ecl}\,. \tag{A.11}$$

Instead of using a theoretical most massive cluster $M_{\rm U,loc}(r)$ as an upper mass limit, $M_{\rm ecl,max,loc}(r)$ was used. This $M_{\rm ecl,max,loc}(r)$ was defined by claiming that there was exactly one cluster in the mass intervall $\left[M_{\rm ecl,max,loc}(r),\ M_{\rm U,loc}(r)\right]$:

$$1 \approx \int_{M_{\rm ecl,max,loc}(r)}^{M_{\rm U,loc(r)}} \xi_{\rm lecl}(M'_{\rm ecl};r)\mathrm{d}M'_{\rm ecl}\,\Delta A\,. \tag{A.12}$$

A criticism of this LECMF formulation is the claim that Eq. (A.12) would result in one most massive cluster with mass $M_{\rm ecl,max,loc}(r)$. In fact it only ensures that there is a most massive cluster without guaranteeing that this most massive cluster has the mass $M_{\rm ecl,max,loc}(r)$. For this another equation is needed:

$$M_{\rm ecl,max,loc}(r) \approx \int_{M_{\rm ecl,max,loc}(r)}^{M_{\rm U}} M'_{\rm ecl}\xi_{\rm lecl}(M'_{\rm ecl};r){\rm d}M'_{\rm ecl}\,\Delta A\,. \tag{A.13}$$

Now it is ensured that there is a mass $M_{\rm ecl,max,loc}(r)$ between $M_{\rm ecl,max,loc}(r)$ and $M_{\rm U}$. But in general an equation system

$$\begin{aligned} 1 &= \int_a^b f(x)\,{\rm d}x\,,\\ a &= \int_a^b x f(x)\,{\rm d}x\,, \end{aligned} \tag{A.14}$$

does not have a real, non-imaginary, solution for power laws. If $f(x)$ is a distribution function this set of equations requests that the mean of x over the interval $[a,\,b]$ has the same value as the minimal value of x. This can only be possible if $a = b$.

A.3 Other models

Alternatives to the exponential model described in Sec. 2.3.1:

A.3.1 Phantom Cluster Model

In the past Eq. (A.12) had been used to calculate the LECMF. It had been assumed that $M_{\rm U}$ is a very large mass, often approximated as infinity. In order to get similar results to the previous method we use a slightly modified form of that equation (introduced in Schulz, Pflamm-Altenburg and Kroupa 2015):

$$1 \approx \int_{M_{\rm U,loc}(r)}^{M_\infty} \xi_{\rm lecl}(M'_{\rm ecl};r){\rm d}M'_{\rm ecl}\,\Delta A\,, \tag{A.15}$$

with M_∞ going towards infinity.

This resulting model, the phantom cluster model, makes the claim that if there would not be an upper mass limit, then there would be one more cluster in the mass range between the upper mass limit and an infinite mass. A phantom cluster, so to speak.

We have to mention that there is no physical reason for claiming that there is exactly one cluster between the upper mass limit and infinity (Schulz, Pflamm-Altenburg and Kroupa, 2015).

The resulting relation between $K(r)$ and $M_{\rm U,loc}$ is:

$$K(r) \approx (\beta-1)\,M_{\rm U,loc}^{\beta-1}(r)/\Delta A\,. \tag{A.16}$$

If one inserts Eq. (A.16) into Eq. (2.13) , so inserting $K(r)$ as a function of $M_{\rm U,loc}(r)$, a direct relation between $M_{\rm U,loc}(r)$ and r is obtained:

$$\int_{M_{\rm ecl,min}}^{M_{\rm U,loc}(r)} (\beta-1)\,\frac{M_{\rm ecl}^{1-\beta}}{M_{\rm U,loc}^{1-\beta}(r)\Delta A}{\rm d}M_{\rm ecl} \approx \frac{M_{\rm tot}}{2\pi r_d^2}e^{-r/r_d}\,. \tag{A.17}$$

This equation is not analytically solvable for $M_{\rm U,loc}$. But numerically it is possible to calculate for every r a corresponding $M_{\rm U,loc}(r)$ and $K(r)$. The only remaining free parameters are β and ΔA.

We can use these two last equations to calculate a $R'(M_{\rm ecl})$ for every $M_{\rm ecl}$, as in the exponential model.

ΔA has to be sufficiently small, so that Eq. (A.15) is still a good approximation, but has to be large enough to ensure that a complete LECMF can be found in the area. In the following we make the assumption of ΔA being constant, for simplicity reasons.

The free parameters (β and ΔA) can be fixed by comparing the model to the empirical SFR-$M_{\rm ecl,max}$ by Weidner, Kroupa and Larsen (2004a) (see Eq. (2.23))

Similar to the local case (see Eqs. (A.6) and (A.7)) the mass of the heaviest cluster in the entire galaxy ($M_{\rm ecl,max}$) is determined by

$$1 = \int_{M_{\rm ecl,t}}^{M_{\rm U}} \xi_{\rm iecl}(M'_{\rm ecl}) {\rm d}M'_{\rm ecl} \tag{A.18}$$

and

$$M_{\rm ecl,max} = \int_{M_{\rm ecl,t}}^{M_{\rm U}} M'_{\rm ecl} \xi_{\rm iecl}(M'_{\rm ecl}) {\rm d}M'_{\rm ecl} \,. \tag{A.19}$$

Using the above Eqs. (A.18) and (A.19) it is possible to calculate for any β a corresponding SFR-$M_{\rm ecl,max}$-relation. These relations can be compared with the empirical found relation from Eq. (2.23) to constraint β. For $\beta = 1.73 \pm 0.01$ and $\Delta A = (2.9 \pm 0.1)\,{\rm kpc}^2$ the SFR-$M_{\rm ecl,max}$-curve aligns best to the fit from Weidner, Kroupa and Larsen (2004a). $M_{\rm U}$ should be larger than any observed cluster. Given the error bars from the observation this requirement is reasonably fulfilled by the chosen parameters, as can be seen in Fig. A.1.

Another concern is whether the chosen ΔA is still small enough that Eq. A.15 is still a good approximation for an integration over the area ΔA. Numerical tests show that using $\Delta A = 2.9\,{\rm kpc}^2$ results in a deviation of up to 3%, compared to an integration over ΔA, which is still quite accurate. Also observations of the LECMF often use a bigger observation area, e.g. C. J. Lada and E. A. Lada (2003b) use an area of roughly $12.6\,{\rm kpc}^2$.

A.3.2 Constant K Model

The following is an ansatz that tries to be as simple as possible while being consistent with the observational data. If we assume that K does not depend on the galactocentric distance r, then Eq. (2.13) should also be valid for $r = 0$. Hence K has for $\beta \neq 2$ the form (with $M_{\rm U,loc}(0) = M_{\rm U}$):

$$K = \frac{(2-\beta) M_{\rm tot}}{2\pi r_d^2 \left(M_{\rm U}^{2-\beta} - M_{\rm ecl,min}^{2-\beta} \right)} \tag{A.20}$$

and for $\beta = 2$:

$$K = \frac{M_{\rm tot}}{2\pi r_d^2 \ln\left(\frac{M_{\rm U}}{M_{\rm ecl,min}}\right)} \,. \tag{A.21}$$

The corresponding $M_{\rm U,loc}$ as obtained from Eq. (2.13), using the above form for K, is for $\beta \neq 2$:

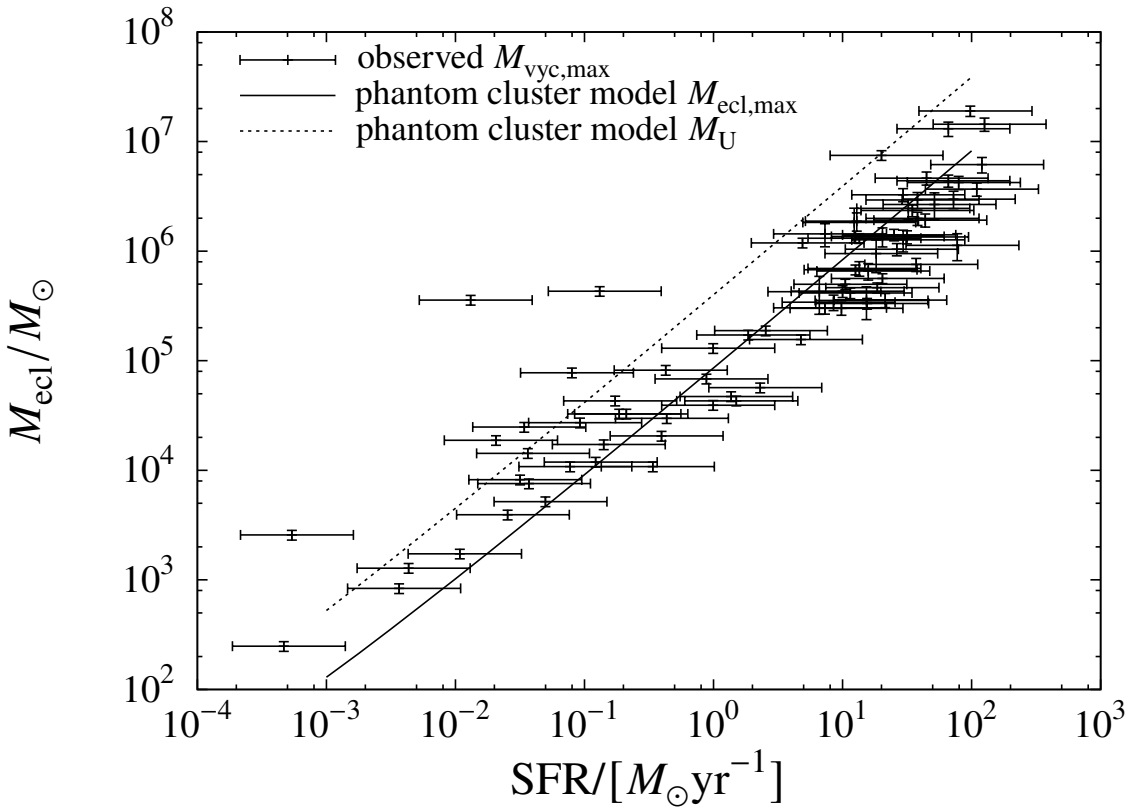

Figure A.1: The observational data are as in Fig. 2.2. Plotted here is $M_{\rm ecl,max}$ and $M_{\rm U}$ against the SFR as calculated using the phantom cluster model for $\beta = 1.73$ and $\Delta A = 2.9\,{\rm kpc}^2$. All observed clusters should be below the $M_{\rm U}$-line within their error-bars, which is not the case here but the data might be consistent with this requirement given the uncertainties. See also Schulz, Pflamm-Altenburg and Kroupa (2015) for a discussion of the outlying data points.

$$M_{\rm U,loc}(r) = \left[e^{-\frac{r}{r_d}} \left(M_{\rm U}^{2-\beta} - M_{\rm ecl,min}^{2-\beta} \right) + M_{\rm ecl,min}^{2-\beta} \right]^{\frac{1}{2-\beta}} , \tag{A.22}$$

and for $\beta = 2$:

$$M_{\rm U,loc}(r) = M_{\rm ecl,min} \left(\frac{M_{\rm U}}{M_{\rm ecl,min}} \right)^{e^{-\frac{r}{r_d}}} . \tag{A.23}$$

We can use these two last equations to calculate $R'(M_{\rm ecl})$, as in the exponential model. For $\beta \neq 2$:

$$R'(M_{\rm ecl}) = -r_d \ln \left[\frac{M_{\rm ecl}^{2-\beta} - M_{\rm ecl,min}^{2-\beta}}{M_{\rm U}^{2-\beta} - M_{\rm ecl,min}^{2-\beta}} \right] \tag{A.24}$$

and for $\beta = 2$:

$$R'(M_{\rm ecl}) = -r_d \ln \left[\frac{\ln\left(\frac{M_{\rm ecl}}{M_{\rm ecl,min}}\right)}{\ln\left(\frac{M_{\rm U}}{M_{\rm ecl,min}}\right)} \right] . \tag{A.25}$$

Consequently $\xi_{\rm iecl}(M_{\rm ecl})$ takes the form

$$\xi_{\rm iecl}(M_{\rm ecl}) = K \int_0^{2\pi} \int_0^{R'(M_{\rm ecl})} M_{\rm ecl}^{-\beta}\, r\, {\rm d}r{\rm d}\phi \,. \tag{A.26}$$

It is now possible to solve this integral analytically to get an IECMF, which depends only on $M_{\rm ecl}$:

$$\xi_{\rm iecl}(M_{\rm ecl}) \quad = K\pi R'^2(M_{\rm ecl}) M_{\rm ecl}^{-\beta} \,. \tag{A.27}$$

This model has two remaining free parameters (β and $M_{\rm U}$). As in the other models we want to calculate $M_{\rm ecl,max}$ in order to compare it to the empirical SFR-$M_{\rm ecl,max}$ by Weidner, Kroupa and Larsen (2004a) (see Eq. (2.23)) and constrain these parameters. Similar to the local case (see Eqs. (A.6) and (A.7)) the mass of the heaviest cluster in the entire galaxy ($M_{\rm ecl,max}$) is determined by

$$1 = \int_{M_{\rm ecl,t}}^{M_{\rm U}} \xi_{\rm iecl}(M'_{\rm ecl}) {\rm d}M'_{\rm ecl} \tag{A.28}$$

and

$$M_{\rm ecl,max} = \int_{M_{\rm ecl,t}}^{M_{\rm U}} M'_{\rm ecl} \xi_{\rm iecl}(M'_{\rm ecl}) {\rm d}M'_{\rm ecl} \,. \tag{A.29}$$

Therefore we can find for every β a SFR-$M_{\rm ecl,max}$-curve that aligns with Eq. (2.23). Doing so we can find for every β a corresponding $M_{\rm U}$:

$$M_{\rm U} = \frac{74138}{2-\beta} {\rm SFR}^{0.91-0.15\beta} \,. \tag{A.30}$$

In order to be realistic this $M_{\rm U}$ has to be heavier than any relevant observed cluster for this specific SFR, but also not so much larger than the mass of the heaviest observed cluster that there would be an unrealistic gap between them. As can be seen in Fig. A.2, $\beta = 1.83 \pm 0.1$ fulfils these observational constraints well.

A.3.3 Comparison of the three models

All the models can be written as

$$\xi_{\rm iecl}(M_{\rm ecl}) = f(M_{\rm ecl}, \beta) M_{\rm ecl}^{-\beta} \,, \tag{A.31}$$

with $f(M_{\rm ecl}, \beta)$ varying from model to model. All three models use a different $f(M_{\rm ecl}, \beta)$ and also different values for β in order to be in agreement to the empirical fit by Weidner, Kroupa and Larsen (2004a) (Eq. 2.23). Eq. (A.31) shows that $\xi_{\rm iecl}$ is not a pure power-law, so β is not the logarithmic slope of $\xi_{\rm iecl}$. For a comparison of ECMFs resulting from the best fits of the models, see Fig. A.3.

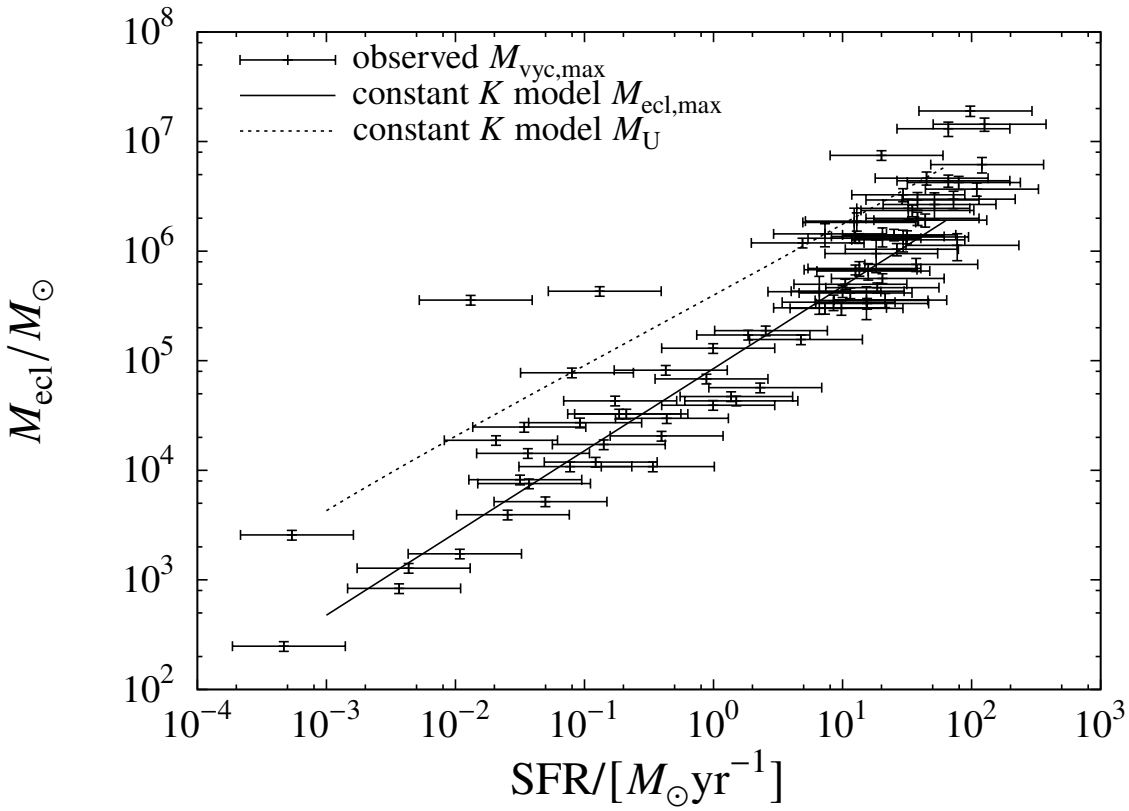

Figure A.2: The observational data are as in Fig. 2.2. Plotted here is $M_{\rm ecl,max}$ and $M_{\rm U}$, as calculated using the constant K model for $\beta = 1.83$ against the SFR. All observed clusters within their uncertainties should be below the $M_{\rm U}$-line, which is fulfilled here well.

One can see that the exponential (Sec. 2.3.1) and the constant K (Sec. A.3.2) model look very similar, although they have different values for β. This is because in these models β is no longer the logarithmic slope. In contrast to the exponential and the constant K model, the phantom cluster model looks different: its logarithmic slope is less steep.

The models also result in different dependencies on the distance to the the galactic center in the case of the LECMF. This is illustrated in Fig. A.4 with parameters chosen in such a way that the models result in the same LECMF for $r = 0$ kpc.

An important difference between the phantom cluster model (Sec. A.3.1) and the other models is that the phantom cluster model has the free parameters β and ΔA, in comparison to the other two which have instead of ΔA a direct dependence on the parameter $M_{\rm U}$. Therefore the exponential and the constant K model allow for a $M_{\rm U}$ which is larger than the masses of the observed clusters (see Figs. 2.2 and A.2).

Another difference is that the constant K model can be solved analytically, whereas the other models need to be solved numerically.

Summarizing, overall the exponential model, which is physically motivated (Pflamm-Altenburg and Kroupa, 2008b), works best, as the phantom cluster model depends on a rather arbitrary ΔA and the

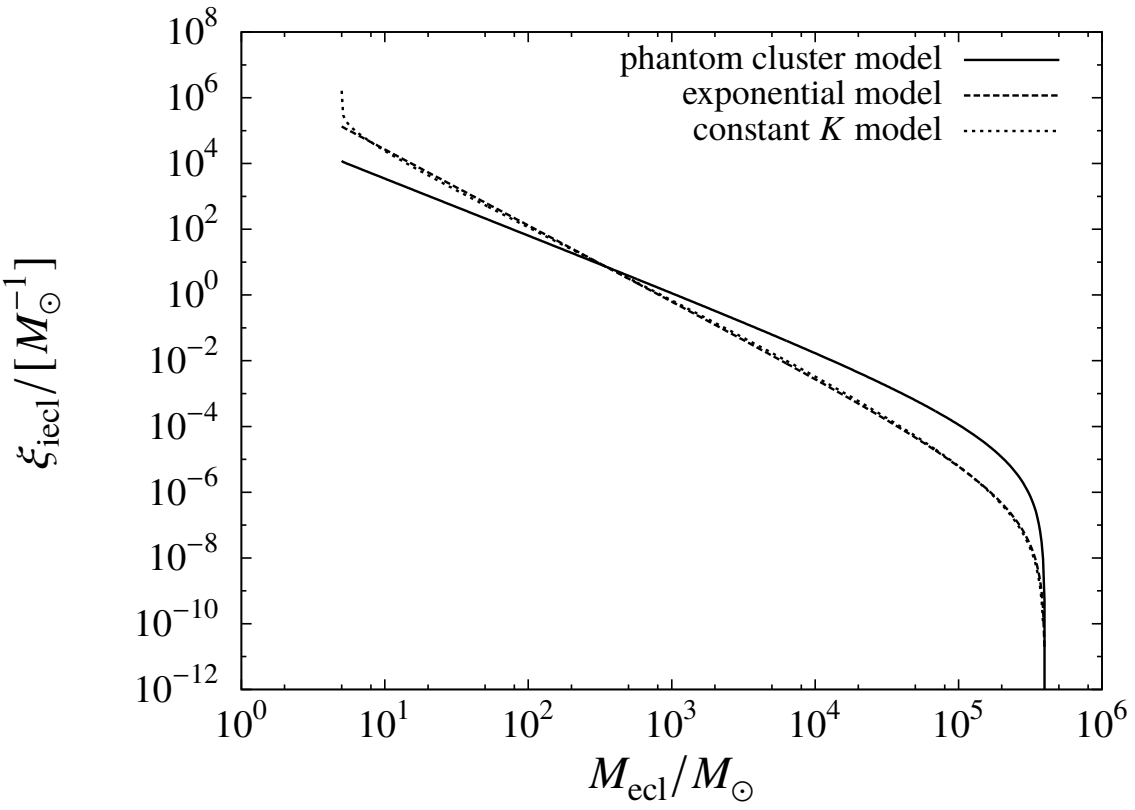

Figure A.3: Comparison of the three models for a galaxy-wide SFR of 1 $M_\odot$/yr and for δt = 10 Myr. For the phantom cluster model β = 1.73 was used, for the exponential model β = 2.31 and for the constant K model β = 1.83. These values have been chosen so that the models fit the observational data shown in Figs. 2.2, A.1 and A.2.

constant K model does not reproduce well local data. But one may still apply these models, e.g. if one needs an IECMF without numerical modelling, one can use the constant K model.

A.4 Summary of Variables

Table A.1: List of variables that were introduced.

Variable	Definition	Reason for Introduction
$N_{\rm ecl}$	number of embedded star clusters	see definition of $\xi_{\rm lecl}$
$M_{\rm ecl}$	mass of an embedded star cluster	see definition of $\xi_{\rm lecl}$
A	surface area	see definition of $\xi_{\rm lecl}$
r	galactocentric distance	see definition of $\xi_{\rm lecl}$
$\xi_{\rm lecl}$	local embedded cluster mass function: $\frac{{\rm d}N}{{\rm d}M_{\rm ecl}{\rm d}A}$ at r	parameter studied in chapter 2
K	normalization constant	the normalization constant for $\xi_{\rm lecl}$
β	power law index	power law index and logarithmic slope of $\xi_{\rm lecl}$
$M_{\rm ecl,min}$	minimal embedded cluster mass	the smallest cluster mass
$M_{\rm ecl,max}$	the largest cluster mass in a given galaxy	used to compare theory with observations
$M_{\rm ecl,max,loc}$	local $M_{\rm ecl,max}$	used to compare theory with observations
δt	star formation time-scale	proportional to K
SFR	star formation rate	used to calculate the normalization constant K
LSFR	local star formation rate	proportional to K in the local case
$\Sigma_{\rm SFR}$	start formation rate surface density	proportional to K in the local, infinitesimal case
$M_{\rm U}$	theoretical most massive cluster physically possible	upper limit for $M_{\rm ecl}$ in a galaxy
$M_{\rm U,loc}$	local $M_{\rm U}$	upper limit for $M_{\rm ecl}$ at r
$M_{\rm ecl,t}$	auxiliary variable	needed together with $M_{\rm U,loc}$ to calculate $M_{\rm ecl,max,loc}$: there is exactly one cluster of mass $M_{\rm ecl,max,loc}$ between $M_{\rm ecl,t}$ and $M_{\rm U,loc}$
$\xi_{\rm iecl}$	integrated embedded cluster mass function : $\frac{{\rm d}N}{{\rm d}M_{\rm ecl}}$	parameter studied in chapter 2
R	radius of the star forming area	upper limit for r
R'	maximal theoretical galactocentric distance for a cluster	necessary to change the r-dependence into a mass dependence
$M_{\rm vyc,max}$	observationally derived maximal very young cluster mass	a good approximation for $M_{\rm ecl,max}$

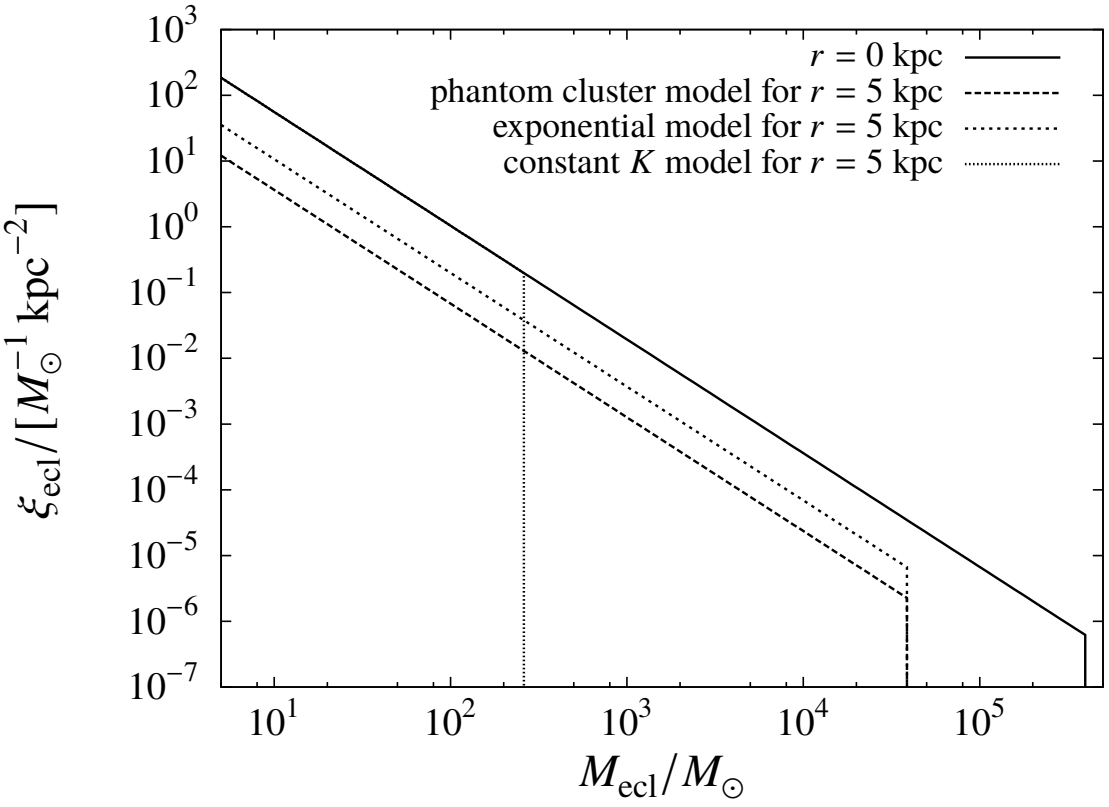

Figure A.4: Comparison of the dependence on the galactocentric distance of the three models. All models are shown with $\beta = 1.73$, $M_{\rm U} = 400000\ M_\odot$, SFR = $1\ M_\odot$/yr, $\delta t = 10$ Myr and $r_d = 2.15$ kpc. These values are not the previous fit values but were chosen so that all models produce the same LECMF for a galactocentric distance of 0 kpc. Note that the constant K model leads to a significantly smaller $M_{\rm U,loc}(r)$, for $r = 5$ kpc, than the other models.

APPENDIX B

Appendix of Chapter 3

B.1 The free-fall time in MOND

In Newtonian dynamics, there are two ways to calculate the free-fall time. The first is to start from the equation of motion in free fall

$$\frac{d^2r}{dt^2} = -\frac{GM}{r(t)^2}\,, \tag{B.1}$$

and solve the differential equation in time t. Another possibility without referring to differential equations would be Kepler's Third Law. Assuming that one has two objects orbiting each other with a semi-minor axis of 0 and a semi-major axis of $R/2$ with R being the initial distance of the two masses, we would get the same result since the free-fall time would be half the orbital period.

In MOND, there are two things to keep in mind: the first approach, using the equation of motion, can only be done for the extreme cases, as the differential equation is not algebraically solvable in the general case:

$$\frac{d^2r}{dt^2} = -\frac{GM}{r(t)^2}\nu\left(\frac{g_{\mathrm{N}}(t)}{a_0}\right)\left(1+\tanh\left(0.825\frac{g_{\mathrm{ext,N}}r(t)^2}{GM}\right)^{3.7}\frac{K(t)}{3}\right), \tag{B.2}$$

here with added emphasis on the parts of the equation of motion which depend on t. Secondly, the approach using Kepler's third law leads to a different result compared to the first approach. In the case of the isolated deep-MOND limit, the numerical difference of the two approaches reaches its maximum of $\frac{2}{\sqrt{\pi}}$. The reason for this is that MOND is not axi-symmetric and therefore the approach using Kepler's Third Law yields an offset to the correct value. Note that this offset disappears in the external-field dominated or Newtonian case.

The important point is that the approach using Kepler's Third Law can be used for any intermediate case, whereas the approach using a differential equation can only be used for the extreme cases. Using Kepler's Third Law gives the correct dependencies and is only off by a numerical factor of order unity.

Therefore, one can use this approach to write the free-fall time in MOND as:

$$t_{\rm ff} = \frac{\pi}{2} \frac{R^{3/2}}{\sqrt{2GM\nu\left(g_{\rm N}/a_0\right)\left(1+\tanh\left(0.825\frac{g_{\rm ext,N}}{g_{\rm int,N}}\right)^{3.7}\frac{K}{3}\right)}} N\,, \tag{B.3}$$

with N being a numerical factor between 1 and $\frac{2}{\sqrt{\pi}}$. N is therefore an interpolating function with the following characteristics: $N = 1$ in the Newtonian and external field-dominated cases and $N = \frac{2}{\sqrt{\pi}}$ in the deep-MOND limit. As a compromise between accuracy and simplicity, we found the following function:

$$N = 1 + \frac{\left(1-\frac{1}{\nu\left(g_{\rm N}/a_0\right)}\right)\left(\frac{2}{\sqrt{\pi}}-1\right)}{\frac{g_{\rm ext,N}}{g_{\rm int,N}}+1}\,, \tag{B.4}$$

which gives a maximum error of 3%. It is possible to find even more accurate interpolating functions, albeit more complicated ones. For example,

$$N = 1 + \frac{\left(1-\frac{1}{\nu\left(g_{\rm N}/a_0\right)}\right)\left(\frac{2}{\sqrt{\pi}}-1\right)}{\left(\frac{g_{\rm ext,N}}{g_{\rm int,N}}\right)^{0.6}\ln\left(\frac{g_{\rm ext,N}}{g_{\rm int,N}}+1\right)+1} \tag{B.5}$$

would reduce the maximum error to only 1.2%.

B.2 Comparison with the main sequence including scatter

In this section we discuss whether and how the scatter of the SPARC scaling relations (Lelli, McGaugh and Schombert, 2016) influences the results. In order to quantify this, we assume a maximum possible scatter of 3σ. Firstly we determine how the deviation of the results assuming Newtonian or Milgromian depends on the scatter. As is illustrated in Fig. B.1, more extended or less dense galaxies deviate stronger from the Newtonian models than more concentrated galaxies.

Secondly we consider the effect of the observational scatter on the calculated main sequence of galaxies using the model presented in chapter 3. For this we are using Eq. (3.46), the dependence of the HI-gas-mass on the stellar mass, and Eq. (3.47), the dependence of the scale length on the HI-gas-mass. Using the SPARC data we first determine a correlation between the scatter of two equations:

$$\sigma_{R_d} = -0.34\sigma_{M_{\rm HI}} + 0.14 \pm 0.214\,, \tag{B.6}$$

with σ_{r_d} being the scatter of the scale length R_d from Eq. (3.47) and $\sigma_{M_{\rm HI}}$ being the scatter of the HI-mass from Eq. (3.46). For $\sigma_{M_{\rm HI}}$ we use the value from Lelli, McGaugh and Schombert (2016) of a 1σ-scatter of 0.35.

Assuming that the scatter normal distributed we can now determine the corresponding scatter of the SFR-M_S-relation of the here presented theory. The result is a a 1σ-scatter of about 0.35, mostly due to the uncertainty in the $M_{\rm HI}$-M_S-relation. A comparison with main sequence of galaxies from Speagle et al. (2014), which has a 1σ-scatter of about 0.2, can be seen Fig B.2. Overall the derived main sequence in chapter 3 is in in agreement with the main sequence by Speagle et al. (2014). Note

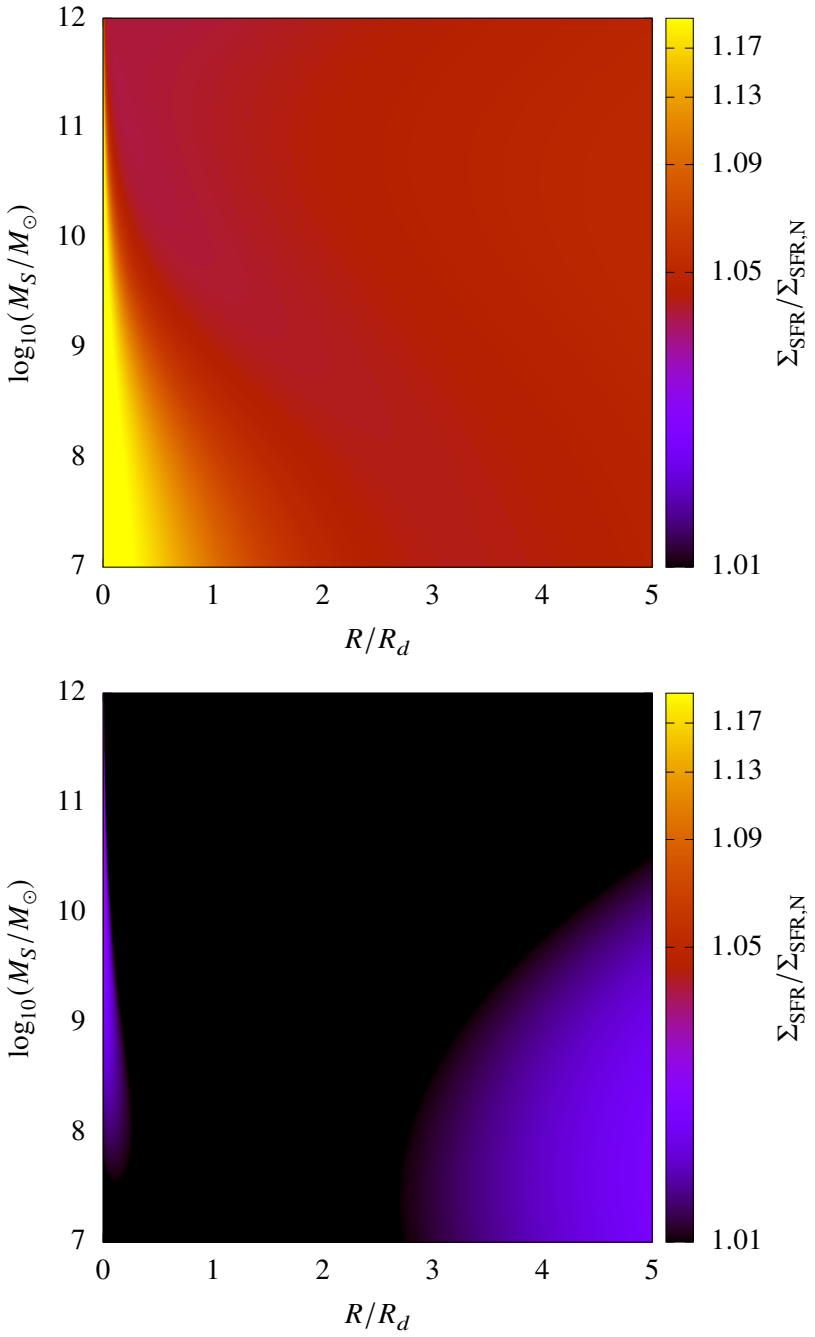

Figure B.1: The same as Fig. 3.4 just with assuming a 3σ-scatter for the scale length. The upper plot shows the relative divergence to a pure Newtonian model for very extended or low-surface brightness galaxies. The lower plot is the same for very dense galaxies. As can be seen the low-surface brightness galaxies always diverge from the Newtonian model and go directly from the deep-MOND limit to the Quasi-Newtonian limit. On th other hand the very dense galaxy is very well approximated using the Newtonian model over its whole range.

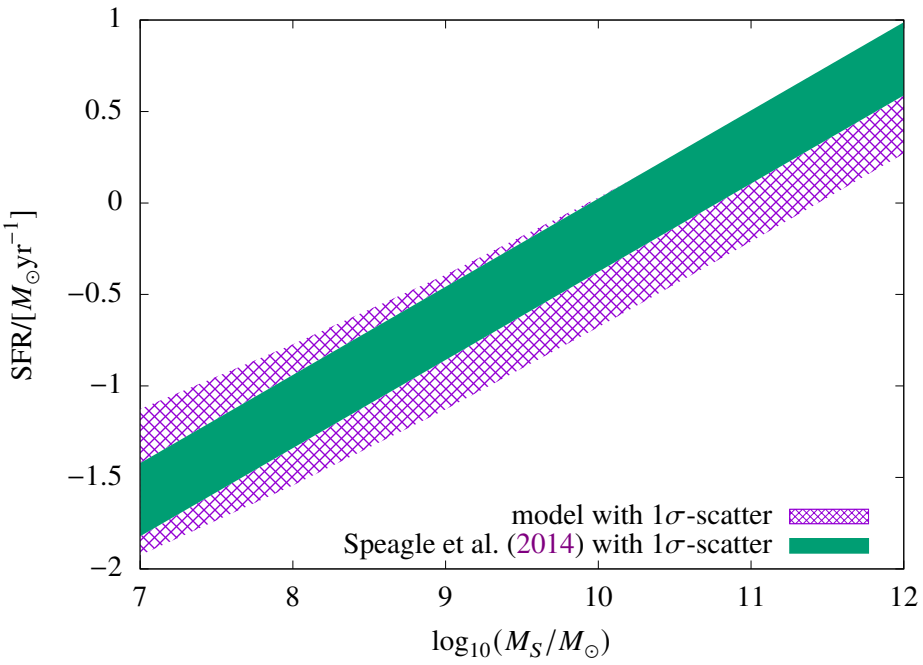

Figure B.2: The star formation rate (SFR) in comparison to the stellar mass of a galaxy. The green area is a fit to observations by Speagle et al. (2014) using an age of the universe of 13.77 Gyr and a scatter of 0.2. The purple area is a numerical integration over the whole galaxy of Eq. 3.18 using the SPARC scaling relations (Lelli, McGaugh and Schombert, 2016) including the RAR (Lelli, McGaugh, Schombert and Pawlowski, 2017) and assuming a star formation efficiency ($\varepsilon_{\mathrm{SFE}}$) of 1.33%. For details of the used scatter scatter see the text. As can be seen, the two areas overlap each other over the whole considered mass range.

that here we assumed that the entire scatter is due to natural scatter and not due to uncertainties in observations. Section 3.4.1 can be interpreted as the other extreme, where all of the scatter is due to observational uncertainties and none of it due to a natural scatter.

APPENDIX C

Appendix of Chapter 5

C.1 Determining $K(R')$ and dN/dA

First we assume the Kennicutt-Schmidt-relation (Eq. 5.9) is valid, according to which the star formation rate surface density $\Sigma_{\rm SFR}(R')$ follows the gas surface density $\Sigma(R')$ (Schmidt, 1959):

$$\Sigma_{\rm SFR}(R') \propto \Sigma^n(R')\,, \tag{C.1}$$

with n being the Kennicutt-Schmidt parameter usually assumed to be 1.4 (Kennicutt, 1989). As we assume the gas disk to be an axis-symmetric exponential disk, we can thus write the star formation rate surface density $\Sigma_{\rm SFR}(R')$ as

$$\Sigma_{\rm SFR}(R') = Ae^{-\frac{nR'}{r_{\rm d}}}\,, \tag{C.2}$$

with A being a constant and $r_{\rm d}$ being the scale length. We know that an integral over the entire disk should give the star formation rate (SFR):

$$\mathrm{SFR} = \int_0^\infty \int_0^{2\pi} Ae^{-\frac{nR'}{r_{\rm d}}}\, r\, d\phi\, dr\,. \tag{C.3}$$

Solving this for A allows to rewrite Eq. (C.2) as (Pflamm-Altenburg and Kroupa, 2008a)

$$\Sigma_{\rm SFR}(R') = \frac{\mathrm{SFR}\, n^2}{2\pi r_{\rm d}^2} e^{-\frac{nR'}{r_{\rm d}}}\,. \tag{C.4}$$

Multiplying $\Sigma_{\rm SFR}(R')$ with the time Δt should result in the mass surface density for stellar mass formed during the time Δt. Multiplying the ECMF (Eq. 5.7) with embedded cluster mass $M_{\rm ecl}$ and solving the mass integral also results in the expected value of the mass surface density. Therefore we can write

$$\delta t \frac{\mathrm{SFR}\, \delta t\, n^2}{2\pi r_{\rm d}^2} e^{-\frac{nR'}{r_{\rm d}}} = \int_{M_{\rm min}}^{M_{\rm U}(R')} K(R') M_{\rm ecl}^{1-\beta}\, dM_{\rm ecl}\,. \tag{C.5}$$

This allows us to determine $K(R')$. For $\beta = 2$

$$K(R') = \frac{\mathrm{SFR}\, n^2}{\ln\left(M_\mathrm{U}(R')/M_\mathrm{min}\right) 2\pi r_\mathrm{d}^2} e^{-\frac{nR'}{r_\mathrm{d}}}\,, \tag{C.6}$$

and for $\beta \neq 2$

$$K(R') = \frac{\mathrm{SFR}\, \delta t\, n^2\, (2-\beta)}{\left(M_\mathrm{U}^{2-\beta}(R') - M_\mathrm{min}^{2-\beta}\right) 2\pi r_\mathrm{d}^2} e^{-\frac{nR'}{r_\mathrm{d}}}\,. \tag{C.7}$$

From Eq. (5.7) follows directly

$$\frac{dN_\mathrm{obs}}{dA} = \int_{M_\mathrm{comp}}^{M_\mathrm{U}(R')} K(R') M_\mathrm{ecl}^{-\beta}\, dM_\mathrm{ecl}\,, \tag{C.8}$$

where N_obs is the number of observed clusters (therefore dN_obs/dA is the surface density of observed clusters) and M_comp is the minimum mass for which all clusters can be detected. Inserting the previously calculated $K(R')$ and solving the integral determines dN/dA. For $\beta = 2$

$$\frac{dN_\mathrm{obs}}{dA} = \frac{\left(M_\mathrm{comp}^{-1} - M_\mathrm{U}^{-1}(R')\right) \mathrm{SFR}\, \delta t\, n^2}{\ln\left(M_\mathrm{U}(R')/M_\mathrm{min}\right) 2\pi r_\mathrm{d}^2} e^{-\frac{nR'}{r_\mathrm{d}}}\,, \tag{C.9}$$

and for $\beta \neq 2$ and $\beta \neq 1$

$$\frac{dN_\mathrm{obs}}{dA} = \frac{\left(M_\mathrm{U}^{1-\beta}(R') - M_\mathrm{comp}^{1-\beta}\right) \mathrm{SFR}\, \delta t\, n^2\, (2-\beta)}{\left(M_\mathrm{U}^{2-\beta}(R') - M_\mathrm{min}^{2-\beta}\right) 2\pi r_\mathrm{d}^2\, (1-\beta)} e^{-\frac{nR'}{r_\mathrm{d}}}\,, \tag{C.10}$$

thus giving the number surface density of clusters formed during the time δt at galactocentric distance R'.

C.2 Drawing random numbers

The method used is inspired by Kroupa (2002), used there as the generating function for the initial mass function.

Lets assume one has the probability density function $C\, p(x)$, where C is a constant. The indefinite integral of $p(x)$ is

$$\int p(x)dx = P(x)\,. \tag{C.11}$$

Further let x_0 be the lower limit of $p(x)$ and x_1 the upper limit. Then one obtains the normalization of $C\, p(x)$:

$$\int_{x_0}^{x_1} C\, p(x)dx = C(P(x_1) - P(x_0)) = 1\,, \tag{C.12}$$

which leads to

$$C = \frac{1}{P(x_1) - P(x_0)}\,. \tag{C.13}$$

Now let y be a uniformly distributed random variable on [0,1]:

$$\int_{x_0}^{x} C\, p(x')dx' = C(P(x) - P(x_0)) = \frac{P(x) - P(x_0)}{P(x_1) - P(x_0)} = y\,. \tag{C.14}$$

And therefore solving Eq. (C.14) for x gives you random variable between x_0 and x_1 distributed according to $p(x)$.

C.2.1 Drawing a random galactocentric distance

In the case of drawing a random galactocentric distance our $C\, p(x)$ is for $\beta = 2$ (see Eq. C.9)

$$dN/dA = 2\pi R' dN/dR' = C\, p(R') = C \frac{\left(M_{\rm comp}^{-1} - M_{\rm U}^{-1}(R')\right)}{\ln\left(M_{\rm U}(R')/M_{\rm min}\right)} e^{-\frac{nR'}{r_{\rm d}}} R'\,, \tag{C.15}$$

and for $\beta \neq 2$

$$C\, p(R') = C \frac{\left(M_{\rm U}^{1-\beta}(R') - M_{\rm comp}^{1-\beta}\right)}{\left(M_{\rm U}^{2-\beta}(R') - M_{\rm min}^{2-\beta}\right)} e^{-\frac{nR'}{r_{\rm d}}} R'\,. \tag{C.16}$$

Although this is not analytically solvable anymore, the process described in Section C.2 can still be done:

$$P(R') = \int p(R')dR'\,. \tag{C.17}$$

Solving the integral numerically for $x_0 = R_0$ and $x_1 = R_1$ we get

$$C = \frac{1}{P(R_1) - P(R_0)}\,. \tag{C.18}$$

With that Eq. (C.14) becomes

$$\frac{P(x) - P(R_0)}{P(R_1) - P(R_0)} = y\,. \tag{C.19}$$

Solving this equation numerically for x gives the relation to draw the correctly distributed random number.

C.2.2 Drawing a random mass

If we want to draw a random mass our $C\, p(x)$ is the ECMF

$$\xi(M) = C\, p(M) = CM^{-\beta}\,, \tag{C.20}$$

and therefore

$$P(M) = \int p(M)dM = \frac{M^{1-\beta}}{1-\beta}\,. \tag{C.21}$$

With $x_0 = M_{\mathrm{comp}}$ and $x_1 = M_{\mathrm{U}}$ we get

$$C = \frac{1-\beta}{M_{\mathrm{U}}^{1-\beta} - M_{\mathrm{comp}}^{1-\beta}}\,, \tag{C.22}$$

in the extreme case of $M_{\mathrm{U}} = \infty$ this simplifies to $C = \frac{\beta-1}{M_{\mathrm{comp}}^{1-\beta}}$. So Eq. (C.14) becomes

$$\frac{x^{1-\beta} - M_{\mathrm{comp}}^{1-\beta}}{M_{\mathrm{U}}^{1-\beta} - M_{\mathrm{comp}}^{1-\beta}} = y\,, \tag{C.23}$$

and solving for x gives

$$x = \left[\left(M_{\mathrm{U}}^{1-\beta} - M_{\mathrm{comp}}^{1-\beta}\right) y + M_{\mathrm{comp}}^{1-\beta}\right]^{\frac{1}{1-\beta}}\,. \tag{C.24}$$

List of Figures

List of Tables

Acknowledgements

First of all, I would like to thank my PhD supervisor Pavel kroupa, who guided and supported me through my time working on this thesis. I much appreciate the chances and insights he has given me during the past years. Further I would like to extend my gratitude to others who supported me and helped me to continue during this project. I especially would like to thank Mathias Kruckow, Patrick Neunteufel ans Armin Rasekh, who were always open to the discussion of new ideas. Also I would like to thank Moritz Haslbauer who shared an office with me and helped with insightful comments and a relaxing atmosphere. Not to forget Ingo Thies, who was always ready to help, when one asked him. Indranil Banik has my gratitude for his support regarding the MONDian calculations in chapter 3.

Going back to my student days I would also like to thank Thomas Reiprich for the work with him during my Bachelor and Master-thesis.

On a more private note I thank Christopher Helmes and Philipp Bielefeldt, who were patient enough to live for seven years with me in a shared flat. Finally I want to thank my parents for giving me the opportunities and help necessary so that I could even be writing these lines (I also thank my sisters but do not tell them that).